UNIVERSITY OF BELGRADE
SCHOOL OF ELECTRICAL ENGINEERING

Nikola Jovalekic

IMPROVING THE PERFORMANCE OF LoRa BASED WIRELESS TRANSCEIVERS

Doctoral Dissertation

Belgrade, 2018

UNIVERZITET U BEOGRADU
ELEKTROTEHNIČKI FAKULTET

Nikola Jovalekić

POBOLJŠANJE PERFORMANSI BEŽIČNIH PRIMOPREDAJNIKA ZASNOVANIH NA LoRa MODULACIJI

Doktorska disertacija

Beograd, 2018

Supervisor:

Dr Vujo Drndarevic, Full Professor

University of Belgrade, School of Electrical Engineering

Committee:

Dr Aleksandar Neskovic, Full Professor

University of Belgrade, School of Electrical Engineering

Dr Nenad Jevtic, Assistant Professor

University of Belgrade, Faculty of Transport and Traffic Engineering

Dr Ivan Popovic, Assistant Professor

University of Belgrade, School of Electrical Engineering

Dr Dragan Olcan, Associate Professor

University of Belgrade, School of Electrical Engineering

"The coming of the wireless era will make war impossible, because it will make war ridiculous."

— Guglielmo Marconi

To my family and the star brightening my way.

In memory of my mother Slavica and her unwavering support and belief in me, and in memory of my grandmother Djordjina

Acknowledgments

I would like to express my sincere gratitude to my advisor Prof. Dr. Vujo Drndarevic for the continuous support of my PhD study and related research. His guidance helped me in all the stages of my research and in writing of this thesis.

I would like to thank Prof. Ermanno Pietrosemoli and my father Branislav Jovalekic for their help with the design of field experiments, data collection, and insightful discussions.

My sincere thanks also go to Dr. Marco Zennaro and Dr. Iain Darby who provided me an opportunity to join their team, and who gave me access to the laboratory and research facilities.

Last but not the least, I would like to thank my sister Zorana Dubljevic for supporting me unconditionally throughout this process and in my life in general.

Dissertation Title: Improving the Performance of LoRa Based Wireless Transceivers

Abstract: The use of wireless technologies dominates the everyday life of a modern society. Internet of Things, the new paradigm of interaction between humans and their environment, unlocks advanced scenarios of collecting information from the real world using various sensors. One of the recently developed technologies, that is a potential candidate to become a prevalent technology exploited in the Internet of Things arena, is LoRa. The technology has been extensively explored in numerous theoretical and experimental studies, and a significant insight has been gained.

However, to provide a deeper insight into LoRa technology capabilities, the novel LoRa transceiver with improved characteristics in terms of sensitivity and immunity to external interferences has been developed. This work presents the development methodology, as well as the laboratory experiments that verified the transceiver's superior characteristics. In addition, it provides performance comparison with two widely adopted commercial solutions. The results have shown that the novel LoRa transceiver has an improved sensitivity of 15–25 dB, while the field experiments revealed higher immunity to external interferences.

The second part of the thesis explores LoRa capabilities and limitations by deploying the novel transceiver along with the two commercial transceivers in various experimental scenarios. Namely, the transceivers were deployed in very long and ultra-long distance links providing two propagation conditions: line-of-sight over land and line-of-sight over seawater. In addition, obstructed line-of-sight scenario over sea water has been investigated. The results indicate that 112 km long links over land are fully feasible using low-cost, rubber-duck, omnidirectional antennas and standard output powers in two ISM frequency bands, 868 MHz and 434 MHz, provided that line-of-sight is guaranteed. Furthermore, it has been shown that such links can be established for virtually any combination of LoRa parameters, since the experiments were carried out deploying three different, characteristic, set of LoRa parameters, namely: for spreading factors of SF $\in \{7, 10, 12\}$, within a fixed bandwidth of BW = 125 kHz, and deploying fixed coding rate of CR = 4/6. The short and long-term temporal analysis of the links revealed that the main cause of packet reception rate deterioration are multipath propagation effects, while the

radio-interference has negligible effects on packet reception rate. Furthermore, it has been demonstrated that ultra-long distance links of 316 km are also possible, in both ISM bands of interest, but using only novel LoRa transceiver. The significance of the results is amplified by the fact that omnidirectional antennas were used in the experiments with standard output powers.

Finally, the experiments over seawater revealed that links up to 22 km in line-of-sight mode are fully feasible using low-cost, rubber-duck, omnidirectional antennas and standard output powers with link margin yielding more than 15 dB in both ISM frequency bands. Moreover, the links in obstructed line-of-sight mode over 28 km are also possible in ISM 434 MHz band; however, there are certain limitations when it comes to their practical implementations since costly and bulky antennas are needed on both sides and transmission reliability is not guaranteed.

Keywords: IoT, LPWAN, LoRaWAN, LoRa, transceiver, long range, sensitivity, interference, immunity

Scientific area: Technical Sciences, Electrical Engineering

Specific scientific area: Electronics

UDK number: 621.3

Naslov teze: Poboljšanje performansi bežičnih primopredajnika zasnovanih na LoRa modulaciji

Rezime: Savremene bezične tehnologije značajno utiču na svakodnevni život modernog društva. *Internet stvari*, nova paradigma interakcije čoveka sa njegovom okolinom, omogućava brzo prikupljanje i selektovanje informacija iz realnog sveta koristeći različite vrste senzora. Jedna od novih tehnologija, koja je potencijalni kandidat da postane najmasovnije upotrebljavana tehnologija u takvim sistemima jeste upravo LoRa. Ova tehnologija je, do sada, ispitivana kroz brojne teoretske i eskperimentalne studije.

Da bi se obezbedio dublji uvid u mogućnosti tehnologije, razvijen je novi LoRa primopredajnik sa poboljšanim karakteristikama u smislu osetljivosti i imunosti na smetnje. U tezi je prikazana metodologija razvoja novog primopredajnika i dati su rezultati laboratorijskih ispitivanja koji verifikuju poboljšane performanse. Takodje su uradjena uporedna ispitivanja novorazvijenog primopredajnika sa dva veoma rasprostranjena komercijalna primopredajnika. Rezultati ispitivanja su pokazali, da novi LoRa primopredajnik ima poboljšanu osetljivost u opsegu 15–25 dB, dok su rezultati ispitivanja u realnim uslovima dodatno utvrdili i veću imunost na spoljnje smetnje.

U drugom delu teze su dati rezultati eksperimenta izvršenih u realnim uslovima. Novi LoRa primopredjanik je ispitivan na vrlo dugačkim i izuzetno dugačkim trasama u dva karakteristična propagaciona scenarija: kada je zadovoljen uslov optičke vidljivosti i kada je optička vidljivost blokirana izmedju prijemnika i predajnika. U ovim eksperimentima linkovi su formirani iznad kopna i iznad mora.

Rezultati eksperimenata su pokazali da, ukoliko je obezbedjena optička vidljivost izmedju prijemnika i predajnika, linkovi u dužini od 112 km iznad kopna u potpunosti su izvodljivi, koristeći omnidirekcione antene i standardnu izlaznu snagu u oba ISM opsega, 868 MHz i 434 MHz. Takodje, pokazano je da takvi linkovi mogu biti uspostavljeni za bilo koju kombinaciju LoRa parametara, uključujući i komercijalne primopredajnike, s obzirom na to da su eksperimenti izvršeni za tri karakteristična seta LoRa parametara, naime: koristeći faktore širenja SF $\in \{7, 10, 12\}$ unutar fiksnog LoRa opsega od BW = 125 kHz i upotrebom zaštitnog kodovanja

CR = 4/6. Analiza parametara linka u vremenskom domenu je pokazala da je glavni uzrok gubitka paketa *mulitpath* propagacija signala, dok je radio-interferencija imala zanemariv doprinos gubitku paketa. Dalje je pokazano da su izuzetno dugački linkovi, dužine 316 km, izvodljivi koristeći novorazvijeni primopredajnik u oba ISM opsega od interesa, upotrebljavajući omnidirekcione antene i standardne izlazne snage. Konačno, eksperimenti iznad morske površine su pokazali da, ukoliko postoji optička vidljivost izmedju prijemnika i predajnika, linkovi u dužini od 22 km su mogući i to u oba ISM opsega od interesa, koristeći omnidirekcione antene i standardne izlazne snage; margina linka od 15 dB u oba frekvencijska opsega implicira da su moguća i veća rastojanja. Eksperimentalno je utvrdjeno i da, ukoliko je optička vidljivost preko morske površine izmedju prijemnika i predajnika blokirana, moguće je uspostaviti link u dužini od 28 km na frekvenciji od 434 MHz, upotrebom antena sa većim pojačanjem, ali kvalitet prenosa u ovom slučaju ne može biti garantovan.

Ključne reči: IoT, LPWAN, LoRaWAN, LoRa, primopredajnik, dugački linkovi, osetljivost, interferencija, imunost

Naučna oblast: tehničke nauke, elektrotehnika

Uža naučna oblast: elektronika

UDK broj: 621.3

Contents

List of Figures

List of Tables

Chapter 1

Introduction

In recent years several new technologies have emerged in IoT arena. These technologies unlocked the new use cases and accelerated the development of different paradigms applied in wireless sensors networks [1–3]. One such technology is LoRa (Long Range), developed by Semtech.

LoRa is one of the several technologies that have been developed lately to address the problem of high power consumption in existing wireless sensor networks and to extend the range [4]. As a consequence, a new paradigm has been developed, and traditional mesh wireless sensor network topologies shifted to star topologies, eliminating complex routing protocols, consequently lowering the power consumption while increasing the transmission reliability.

Such technologies trade data rate for sensitivity [5]; some of them utilize spread spectrum types of modulation, while others exploit narrow band technology. They mostly operate in unlicensed part of the spectrum, enabling free of charge data transfer. Due to extended ranges and low power consumption, they are mostly utilized in Low Power Wide Area Networks (LPWANs) [6, 7].

The advent of LoRa technology is followed by the increased efforts of the scientific community to assess the potentials of the technology and gain deeper insights into its capabilities and limitations. Numerous experiments have been carried out in both laboratory and field; the focus was mostly on range exploration in different propagation scenarios, packet loss, and technology suitability for different industrial applications.

However, the conclusions drawn from those experiments are limited by several

factors. The use of commercial general-purpose LoRa development kits masks the real capabilities of LoRa transceivers since trade-offs in the kit design often lead to suboptimal performance. The antenna radiation pattern, gain and RF front-end impedance matching are often not specified, thus limiting the correct interpretation of experimental results. A small number of packets sent prevents statistical processing of the experimental data. The reporting of grossly aggregate performance metrics, typically limited to long-term average values of Received Signal Strength (RSS) and packet loss, does not give information about short-term fluctuations and temporal variability of link behavior. In addition, no information is given as to whether and how RSS calibration is performed, which somewhat limits the informativeness of experimental results reported in such previous works. Finally, test scenarios explored are usually urban areas where nodes are placed at relatively short distances, which restricts obtaining the deeper insight into technology capabilities in terms of range.

To bridge the identified gaps and provide a deeper insight into LoRa technology and its limitations, we first designed the novel LoRa transceiver with improved characteristics in terms of sensitivity and immunity to external interferences. Next, we carried out laboratory experiments to verify its characteristics and confirm improved sensitivity. Further, we performed the field tests which aimed to explore transceiver's characteristics in real operating conditions - primarily immunity to external interferences - and to investigate the feasibility and analyze long and ultra-long LoRa links. For that purpose, we deployed various commercial transceivers, as well as the own-developed transceiver in different experimental scenarios. Namely, we investigated two typical propagation conditions: Line-of-Sight (LOS) and obstructed LOS. The LOS experimental scenario encompassed three different testbeds: 1) LOS over seawater (22 km), 2) LOS over land (112 km); and 3) LOS over land (316 km). On the other hand, obstructed LOS scenario included testbed over seawater (28 km). All the experiments were performed deploying transceivers to operate simultaneously in two different Industrial, Scientific, and Medical (ISM) bands: 868 MHz, and 434 MHz.

To further address the identified gaps, we calibrated the RSS indicators of each

transceiver used in the experiments and investigated the linearity of their Signal-to-Noise (SNR) measurement chains, determining the RSS threshold for which the SNR measurement chains go into saturation. In addition, we deployed antennas of known radiation pattern and gain, providing correct impedance matching. Finally, we increased the traffic between experimental nodes significantly in comparison to the others experiments thus enabling statistical processing of the measurement results and more robust conclusions.

The presented approach led to the following contributions:

- The development of the highly-sensitive LoRa transceiver yielding 5 dB of sensitivity improvement in comparison to the value specified in the LoRa modem specifications used to develop the novel transceiver; moreover, the better sensitivity of 15–25 dB in comparison to two widely adopted commercial transceivers.

- Demonstration of very long and ultra-long LoRa links using low-cost commercial-off-the-shelf (COTS) omnidirectional antennas with standard-compliant output power in two ISM bands: 868 MHz and 434 MHz.

- Temporal analysis of the link variability for different spreading factors (7, 10, 12) within a fixed LoRa bandwidth of 125 kHz in four experimental cases: 1) LOS over seawater (22 km), 2) obstructed LOS over seawater (28 km), 3) LOS over land (112 km); and 4) LOS over land (316 km).

The thesis is organized into six chapters, summarized as follows:

Chapter 2 firstly introduces fundamentals of LoRa technology by providing available technical details. Next, it gives an overview of the LoRa transceivers developed by the scientific community and analyzes them in terms of hardware design. Additionally, commercial transceivers used in the scientific experiments are presented. Finally, a detailed overview of experiments carried out is reported, as well as the conclusions drawn.

Chapter 3 presents the design and implementation methodology of the LoRa transceiver with improved characteristics. A theoretical background is given, as well as a detailed development methodology. A Printed Circuit Board (PCB) model

is provided and simulations performed to verify the PCB layout of the transceiver. In addition, the firmware implementation methodology is presented.

Chapter 4 gives an overview of the laboratory experimental setup and methods used to verify the characteristics of the transceiver. The results of sensitivity tests, RF output power measurements, and power consumption measurements are given. The RSS indicator correction factors are determined and SNR measurement chain linearity is investigated.

Chapter 5 explores LoRa capabilities in the field experiments deploying different transceivers in various experiments. Two experimental scenarios are investigated: LOS over land and seawater, and blocked LOS over seawater in two ISM frequency bands, namely 868 MHz and 434 MHz. The measurements are performed for three different values of spreading factor, SF $\in \{7, 10, 12\}$, within fixed LoRa bandwidth of 125 kHz and a coding rate of CR $= 4/6$. The temporal analysis of the links is provided and corresponding conclusions delivered.

Chapter 6 presents concluding remarks and perspectives for future work.

Chapter 2

State of the Art

In this section, we provide a theoretical background for LoRa modulation and present LoRa technology fundamentals. In addition, we report on the work of other research groups that developed LoRa transceivers to be deployed in scientific experiments and deliver brief descriptions of widely adopted commercial transceivers by the scientific community. Further, we present the LoRa experimental results obtained in different experimental scenarios, as well as the conclusions drawn from these experiments. Finally, we identify the gaps that exist in the current state of the art which must be addressed to provide a deeper insight into LoRa technology.

2.1 LoRa Fundamentals

LoRa is a proprietary low-power wireless technology developed by Semtech. It leverages chirp spread spectrum modulation to increase receiver sensitivity within a fixed channel bandwidth, at the cost of limited throughput [4]. Spread spectrum refers to a general technique in which the transmission bandwidth is increased significantly above the minimum required to convey a certain amount of information. It is currently used in many systems, including WiFi, Bluetooth, and 4G which have proved the effectiveness of the technique. The amount of spreading is defined by the Spreading Factor (SF), which is the ratio between the transmission RF bandwidth and the baseband bandwidth. All the spread spectrum systems devised so far confer a degree of resistance to noise and interference that is proportional to the SF, as can be deducted from Shannon's channel capacity formula:

$$C = B \log_2(1 + \frac{S}{N}) \tag{2.1}$$

where C is capacity or throughput in bits per second, B is bandwidth in hertz, S is the signal power in watt, and N is the noise power in watt.

The same channel capacity can be obtained with a wide bandwidth and low SNR or vice versa. Of course, because of the logarithmic dependence, increasing the bandwidth has a stronger effect than increasing the SNR. Nevertheless, it must be kept in mind that the thermal noise, which controls the ultimate lower limit of the noise power N, is proportional to both the absolute temperature and the bandwidth.

There are many ways to spread the spectrum of a given signal. For example, Bluetooth uses a technique called frequency hopping, in which the carrier frequency of the modulated signal changes in subsequent intervals according to a specific pseudo noise pattern known by both the transmitter and the receiver. WiFi, on the other hand, uses a completely different strategy - the data sequence that contains the information is multiplied by a pseudo-noise sequence at a much higher data rate. The resulting signal has the same bandwidth of the pseudo-noise sequence, thus effecting the "spreading of the spectrum". To recover the information contained in the spread sequence one needs to multiply it by the original pseudo-noise signal that was used at the modulator. This has also the effect of reducing the spectrum occupancy to that of the original baseband signal.

At the receiver, after demodulation, the recovered baseband signal is multiplied by the same pseudo-noise sequence that was used in transmission to yield the original signal. This requires the receiver to be synchronized with the transmitter and to possess a local copy of the pseudo noise sequence used in transmission. Multiplying by a different sequence, or by the same signal offset in time will result in a very low signal because in effect we are performing the cross-correlation between the recovered baseband signal and the pseudo noise sequence. The cross-correlation will show a high value when the local pseudo-noise sequence matches the one used in transmission and very low value for all other sequences if the sequence is offset in time. As might be expected, the pseudo-noise sequence must be of a particular kind that has a strong autocorrelation at zero time offset and very low elsewhere.

LoRa [4, 8] is proprietary modulation based on spread spectrum techniques developed by Semtech. In this type of modulation, the bandwidth spreading is done using "chirps", i.e. pulses of linearly increasing (or decreasing) frequency, spanning the whole bandwidth allocated for transmission. An example of such chirps is shown in Fig. 2.1.

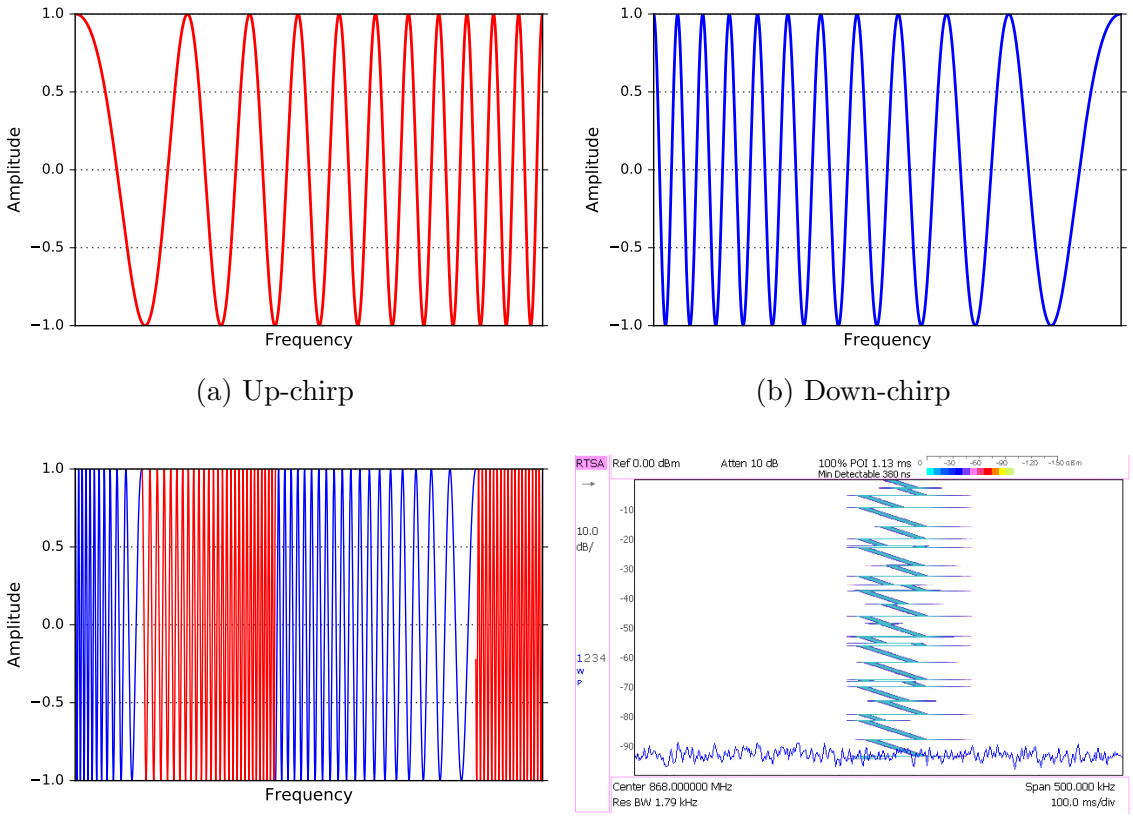

(a) Up-chirp

(b) Down-chirp

(c) Transmitted signal

(d) LoRa packet spectrogram

Figure 2.1: LoRa physical layer. Signals used to convey information: **(a)** up-chirp and **(b)** down-chirp; **(c)** transmitted signal composed of two up-chirps and two down-chirps; **(d)** LoRa packet spectrogram captured by real-time spectrum analyzer.

Data to be transmitted is encoded in abrupt changes from up-chirp to down-chirp or vice versa, maintaining a constant envelope of the modulated signal [5], which simplifies the design of the amplifiers since there is no need for the complex and expensive ones required by other types of modulation [9]. At the receiver side, the same F_c tone is used to down-convert the signal to baseband, where essentially the reverse of the operations performed in transmitting is undertaken to recover the original data affected by the inevitable noise.

Demodulation is accomplished in two steps: 1) multiplying the received signal by the conjugate of each of the two chirps used in transmission, which turns each modulated symbol into regions of constant frequency; and 2) performing a Fast Fourier Transform (FFT) in each region. The peak of the FFT represents the value of the received symbol, easily distinguishable even in the presence of considerable noise or interference [10].

There are three LoRa parameters that enable the designer of the LoRa link to balance between bit rate and robustness of the transmission: Bandwidth (BW), Spreading Factor (SF), and Coding Rate (CR). The bandwidths used in LoRa links can take BW $\in \{125, 250, 500\}$ kHz, while spreading factors can be SF $\in [6, 12]$. Coding rate offers the possibility to add up to four redundant bits for error handling after every 4-bit chunk of payload transmitted, making the transmission more resistant to interference bursts.

We can opt for higher sensitivity by choosing a higher spreading factor, or for a higher bit rate by selecting lower spreading factor. Higher spreading factors result in longer symbol periods and longer packet air times, whereas a lower spreading factor yields shorter transmission times. These trade-offs are illustrated in Fig. 2.2.

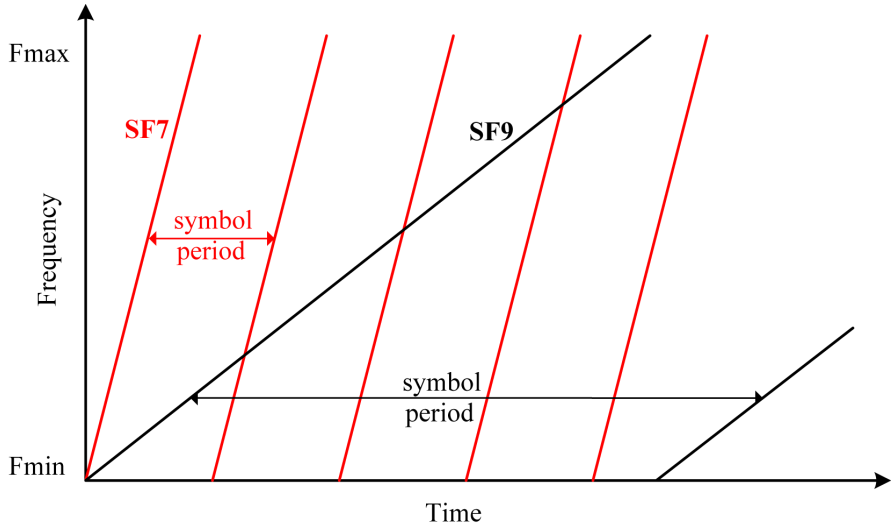

Figure 2.2: Trade-off between symbol period and spreading factor.

Finally, LoRa technology offers two advantages over other technologies used in LPWANs. Since the modulated signal is continuously changing in frequency it is

more tolerant to clock inaccuracies and also to Doppler shifts caused by movements between the transmitter and the receiver [11]. Additionally, the main modulation mechanism i.e. abrupt change of the frequency, facilitates reception of very weak LoRa signals, even below the noise floor of the transceiver.

2.2 LoRa Transceivers Developed by Scientific Community

Most of the experiments carried out by the scientific community so far were performed using commercial transceivers. As already explained, this approach has several downsides. On the other hand, it enables fast planning and execution of the experiments since research groups do not need to develop their own transceivers and experimental setups. However, there are several research groups which developed their own transceivers, optimizing them for different experimental purposes.

For example, in [12] a general-purpose transceiver is presented. The transceiver is optimized in terms of power consumption, size, and cost. It encompasses three sub-blocks: digital sub-block, RF sub-block, and the interface for connecting different sensors.

The operation of the transceiver is managed by the microcontroller from ST, STM32L051, which is based on ARM Cortex M0+ core. This microcontroller is selected since it is optimized for low-power operation.

The RF part is implemented using LoRa module from Dorji, DRF1272F, which is capable of modulating signals in 868 MHz band, exploiting spreading factors $\mathrm{SF} \in [6, 12]$, within the bandwidth of 125 kHz. Here it is worth noting that this approach of implementing the RF sub-block, i.e. using already developed LoRa module, is one of the two widely used. Namely, the second approach implies the usage of the LoRa modem Integrated Circuit (IC), and design of RF front-end on the same PCB where the digital sub-block is realized. Both approaches have advantages and downsides. For example, usage of already developed module simplifies and shortens the time needed to develop the transceiver; on the other hand, the attenuation of the transmitted/received signal is increased since there are multiple

impedance discontinuities on the signal path from the LoRa modem IC pin to the antenna connector. This has a direct impact on the sensitivity and output power of the transceiver, by decreasing both. On the contrary, designing and implementing the customized RF sub-block enables the achievement of higher sensitivity, as well as the output power, but this approach is more complex and requires additional development time.

The sensor interface provides connectivity to different sensors, but the authors do not specify which interfaces they implemented. Further, the authors claim that they ported LoRaWAN MAC to the microcontroller and modified it to fit their experimental scenario, implementing an algorithm which manages the use of different spreading factors fulfilling the low-power requirements.

The low-power characteristics of the transceiver are demonstrated by comparing its power consumption with power consumption of Microchip RN2483 LoRa module. The measurement results showed the difference in three operation modes, namely sleep, receive, and transmit, yielding $\Delta I_{\text{sleep}} = 9.55\,\mu\text{A}$, $\Delta I_{\text{transmit}} = 12\,\text{mA}$, $\Delta I_{\text{receive}} = 3.7\,\text{mA}$, respectively.

In [13], a compact low-power LoRa IoT sensor node with extended dynamic range for channel measurements is presented. This transceiver is primarily meant to be deployed in the experiments where a wide dynamic range of RSS should be measured, without saturating the SNR measurement chain.

The node consists of the digital part, RF part, and peripherals. The digital part encompasses microcontroller and NAND flash; the authors opted for 8-bit microcontroller based on 8051 architecture from Silicon Labs, C8051F342, and 32 MB of NAND flash storage. On the other hand, the RF part consists of LoRa module from Microchip, RN2438, and two digitally controlled attenuators since this LoRa module is capable of operating in two different frequency bands: 915 MHz, and 434 MHz.

The node is equipped with 3 sensors: 3D accelerometer, 3D gyroscope, and 3D magnetometer, which enables the transceiver to be used in applications such as indoor navigation and motion monitoring. Additionally, there is also a real-time clock with its own separate 32.768 kHz quartz crystal for timekeeping. Finally, the node also offers the possibility for different sensors to be connected via flat flexible

cable to the microcontroller using a full 8-lead microcontroller I/O port, or the SPI bus.

The hardware design of the node and variety of peripherals makes this transceiver suitable for a broad range of research applications, such as long-term channel measurements, indoor positioning, environmental monitoring, etc. The software allows the analysis of very strong input signals by setting the RF front-end attenuation and recalculation of SNR values to obtain values that are out of the saturation region of SNR measurement chain. This is useful in indoor applications and small distances, where the RSS levels can be higher than a threshold which saturates the SNR measurement chain.

Besides the general-purpose LoRa transceivers, there is also a group of transceivers developed for specific experiments and purposes. For example, in [14], a low-power IoT sensor node for waste management within smart cities is presented. The node is intended to be used for a real-time monitoring of the trash bin load; the authors claim that the node is optimized in terms of power consumption and adapted to be used in harsh environments.

The transceiver's central processing unit is 8-bit microcontroller ATmega328/P, which is responsible for reading the trash level sensor and managing the operation of the transceiver. The trash level detection is realized using the low-cost ultrasound proximity sensor, HC-SR04. On the other hand, the RF sub-block is implemented using an already developed LoRa module from Libelium. The node's firmware provides compliance with LoRaWAN standard, but the duty cycling of the node is regulated using an external timer by disabling the module's power supply. The power supply for the node is provided from AA 1.5 V lithium batteries, with a capacity of 3500 mAh. The device operates in ISM 868 MHz band.

A similar device based on LoRa is presented in [13]. The self-powered environmental monitoring system for smart cities is developed. This device is optimized in terms of power consumption and cost. It integrates various sensors: temperature, humidity, ambient light and different gas sensors, such as sensors for carbon monoxide, carbon dioxide, liquefied petroleum gas, methane, hydrogen, and ozone. The measurement nodes are powered using solar energy for battery charging and

continuous operation. As in the previous work, the ATMega328 microcontroller was used to manage the operation of the node, while RN2483 from Microchip is used as a LoRa module. Besides these sub-blocks, there is also a power management sub-block which controls the charging of the Lithium-Ion battery; this sub-block encompasses a battery with a capacity of 2600 mAh and a solar panel which provides an output voltage of 6 V and power of 3.5 W. Finally, there is also a real-time clock that is used to manage the duty cycling of the transceiver.

In [15] the node that monitors the water pressure and flow together with leak detection in water distribution network is presented. The node is assembled from already developed commercial modules. Namely, Moteino MEGA is used as the main board, which is equipped with the ATMega1284P microcontroller and a HopeRF RFM95 LoRa module. Besides that, there is a real-time clock, as well as a generic sensor interface. A Secure Digital (SD) card enables data logging, while the power management circuit regulates the voltage from the Lithium-Ion battery and provides its charging. Two sensors are connected to the microcontroller via a generic sensor interface: the Honeywell PX3AG1BH010BSAAX pressure sensor and a tiny hydro-generator. The tiny hydro-generator is used as both flow meter and power harvester for battery charging.

In [16] the environmental pollution monitoring device is presented. This device is also assembled from already developed commercial modules. As a carrier board, the LPC2148 development board is used, which is equipped with LM35 temperature sensor and humidity sensor (DHT11). In addition, there are three gas sensors: a carbon dioxide sensor (MQ-135), nitric oxide (MQ-2), and carbon monoxide (MQ-9). An LCD provides the user interface, while there is also GPS module connected to provide the position of the measurement node. The LoRa communication module exploited is based on the SX1278 LoRa modem from Semtech, but the authors do not specify the manufacturer and the part number of the module.

Finally, in [17] the LoRa module used in the cognitive controller for Heating, Ventilation, and Air Conditioning (HVAC) system deployed in the non-domestic building is presented. In this work, the authors upgraded the existing device that measures the concentration of carbon dioxide, temperature, and humidity with LoRa

communication module to provide extended transmission range for sensors' data. As a LoRa module, the RFM95 from HopeRF that operates in ISM 868 MHz band was used.

As can be noticed, all the transceivers presented in this section are developed using the same methodology, which is based on using already developed general-purpose commercial LoRa modules, which are integrated into the transceiver as separate small form factor boards, or directly on the PCB where other transceiver's sub-blocks are placed. However, such an approach can deteriorate the transceiver's overall performance since the commercial modules are impacted with many trade-offs to provide general purpose functionalities. This is particularly important for the sensitivity since such trade-offs usually increase the overall noise floor of the transceiver, consequently reducing its sensitivity. This further implies decreased range especially in urban areas; for example, locations such as building basements become unavailable for packet reception, which reduces the number of potential applications using this technology.

2.3 Commercial LoRa Transceivers Used in Scientific Experiments

In this section, the overview of commercial LoRa transceivers used in scientific experiments is presented. The focus is on the LoRa nodes, while LoRa gateways are not considered. The transceivers presented in the section are divided into two groups: 1) modules, which need host board for the operation; and 2) general-purpose standalone transceivers.

The modules are usually implemented using LoRa modem IC and an adequate RF front-end, providing the interface to a host/processor board. Some of the modules are equipped also with a microcontroller; in this case, the host processor usually communicates with the module using e.g. AT commands, while all the low-level functions that manage the operation of the LoRa modem are executed on the module's microcontroller. This simplifies the design of the firmware but limits the functionalities of the transceiver since, usually, offered AT commands are limited and do not

allow some advanced settings of the LoRa modem. On the other hand, the latter approach does not have limitations in that sense, but firmware development is more complex and time consuming.

General-purpose standalone transceivers are equipped with a microcontroller, power management sub-block, LoRa modem IC, and various peripherals on the same board. This enables the user to very quickly set up the experimental environment and start with measurements. However, due to the already presented reasons, this approach cannot provide reliable experimental data and somewhat limits the usefulness of the conclusions drawn from such experiments.

The most exploited modules in research applications are HopeRF RFM95, Microchip RN2903, RFSolutions RF-LORA, Semtech SX1272/1276 Mbed shield, Pycom LoRa shield, STMicroelectronics Nucleo LoRa shield, and Semtech SX1276 LoRa module.

The first three modules, HopeRF RFM95, Microchip RN2903, and RFSolutions RF-LORA, are low-cost solutions, meant to be used in the custom-made transceivers since they have to be soldered on the carrier board. Except RN2903, these modules do not have a microcontroller, so their operation has to be managed by the host processor. The Microchip's LoRa module is managed via UART using predefined sets of commands. The advantages of these modules are low price, small form factor, and simple integration in the host system. On the other hand, the main downside is that they are not optimized in terms of sensitivity. This is the consequence of small dimensions and high component and trace density which increases the coupling between them; furthermore, due to short traces, the manufacturers opt not to implement controlled impedance of RF traces which can cause reflections and noise problems. Moreover, they usually do not have antenna connectors, so the RF signal experiences additional losses when propagates from LoRa modem IC pin to the connector on the carrier board and vice versa due to an impedance discontinuity on the junction between the module and a host board. However, it is worth mentioning that the RFM95 module from HopeRF is probably the most exploited LoRa module in different implementations.

Besides "raw" LoRa modules, there are also modules which use raw LoRa mod-

ules to implement modules which are suitable for some widely adopted platform such as Raspberry Pi, Arduino, etc. Obviously, the characteristics of such modules are additionally deteriorated due to reasons already mentioned.

As far as general-purpose standalone LoRa transceivers are concerned, currently, there are two extensively used in the scientific experiments: LoRaMote from Semtech and LoRaMote from Microchip.

The LoRaMote from Semtech is based on the LoRa module WiMOD iM880A. It is capable of operating in one ISM band, namely 868 MHz. The transceiver has the following sensors on the board:

- 3-axis accelerometer sensor MMA8451Q,
- 3-axis magnetometer sensor MAG3110,
- altimeter, thermometer and pressure sensor MPL3115A2, and
- SAR proximity sensor SX9500.

Besides the sensors, there is also a GPS module, EEPROM, and I/O expander. The transceiver has a PCB antenna, realized in the form of Planar Inverted F Antenna (PIFA) which can be detached if necessary, and the SMA connector can be soldered to provide the connection of the external antenna. The microcontroller that manages the operation of the transceiver and peripherals is Cortex-M3 based from ST, STM32L151C8U6.

On the other hand, LoRaMote from Microchip is based on 8-bit PIC18LF45K50 microcontroller and utilizes RN2483 LoRa module. The transceiver is capable of operating in two ISM bands, 868 MHz and 434 MHz. However, it has to be noted that there is only one SMA connector which is reserved for 868 MHz band, while for 434 MHz there is 50 Ω trace that goes to the single pin; this may limit the use of lower frequency port since there is no option to mount any of the RF antenna connectors. On the other hand, there are only two sensors on the board: an ambient light sensor (ALS-PT19-315C), and temperature sensor (MCP9700). Besides that, there are I/O expanders, LEDs, and an LCD.

Both transceivers can be powered directly from batteries which simplifies the field deployment. However, there is a significant difference in the number of sensors - it seems that LoRaMote from Semtech is more suitable for measurements that require various sensors, while Microchip is more suitable to provide general LoRa connectivity, offering advantages when LoRa physical layer is concerned.

Examining carefully the architecture and design methodology of the modules and general-purpose development boards, and analyzing their usability in the research applications, several important observations can be made. Firstly, the RF front-end of the modules is not optimized in terms of the impedance matching and crosstalk. In addition, they are usually realized as a two-layer PCBs, without a solid ground plane. As a consequence, immunity to external interferences is decreased, while radiated emissions from the module are increased, which can potentially impact other sub-blocks on the carrier board or nearby devices. This is especially harmful if there is an analog front end on the carrier board where very weak analog signals are measured and have to be amplified.

Moreover, the various trade-offs in the design, which have to be done to build a general-purpose standalone transceiver, further decrease the performance in terms of sensitivity. That can be an issue if the experiments, where the transceiver is to be deployed, aim to investigate e.g. the maximum attainable range. It is obvious that, in this case, the results may be misleading, which further can increase the transmission protocol complexity by adding unnecessary overheads, thus increasing the node's power consumption.

2.4 LoRa Field Experiments

A number of experiments have been carried out in the field deploying different LoRa devices. As stated earlier, commercial development kits were used in different experimental scenarios, such as indoor, urban, and mixed experimental scenarios. The overview starts with indoor experiments and presentations of the main results and conclusions.

2.4.1 Indoor Test Scenarios

Several works addressed LoRa indoor tests scenarios. For example, in [18], the indoor signal propagation of LoRa signal was investigated. The authors deployed a pair of transmitter and receiver, where the transmitter was mobile while the receiver was fixed. In the first group of experiments, the receiver was positioned in the basement of the building, while in the second it was on the roof. The transmitter was sending packets from different locations, while on the receiver side RSS and SNR were logged together with the time stamp. The propagation was investigated for 868 MHz, deploying one set of LoRa parameters, namely BW = 125 kHz, SF = 12. The results showed that reception was possible only when the transmitter was on the same side of the building as the receiver.

In [19] a similar work was carried out, but the packet sending rate was set to be compliant with the LoRaWAN specification. Additionally, during the experiments, three different channels in ISM 868 MHz frequency band were exploited, within 125 kHz LoRa bandwidth. The current consumption of the mobile node was measured and logged. Different locations were investigated, up to 60 m far from the gateway. The gateway logged SNR and RSS of each received packet. The results showed that packet loss stays below 5 % when the gateway and node are on the same floor, whereas it was 27 % when the node was located in the basement.

An almost identical work is presented in [20], with the restriction that the measurements were carried out on the same floor of the building. The authors systematically investigated packet loss for all possible spreading factors within the bandwidth of 125 kHz, as well as coding rates. The results showed that for output power of 14 dBm, packet loss of approximately 25 % was observed. It is interesting to note that in this work the maximum packet loss was observed for SF = 10, which is unexpected since this is not the LoRa operation mode with the lowest sensitivity.

The results presented in [21] shows that packet reception is possible in an indoor scenario on each floor of the 12-story building, when the gateway is placed on the roof of the building. A significant number of the positions was investigated on each floor, generalizing obtained results. The measurements were performed in 868 MHz

band.

Finally, in [22] an indoor scenario in an industrial environment was studied. The area of 250 000 m^2 was investigated for two different spreading factors, SF $\in \{7, 12\}$ within BW = 125 kHz in 868 MHz band. The results showed that there was a negligible packet loss at each location tested for both spreading factors.

2.4.2 Urban Area Test Cases

This group of experiments addresses the requirements for deployment of wireless sensor networks in cities. Different research groups addressed various experimental scenarios, for example, in [23], the range and performance evaluation of LoRa links within the city is presented. The gateway was installed 30 m above the ground and packet delivery rate was tested at different points in a radius of several kilometers from the gateway. The results revealed that the packet delivery rate of 65.76 % can be achieved if the node is positioned outside of the building at a distance of approximately 4 km from the gateway in 868 MHz band, while packet delivery rate of 2.27 % is recorded if the node is positioned in the ground floor of the building at the approximately same distance. Interestingly, the same locations yielded a packet delivery rate of 27.03 % and 0 %, respectively in the 434 MHz band. In both frequency bands, omnidirectional antennas were deployed. The authors also provided the empirical path loss models for both experimental scenarios.

The packet reception rate in an urban scenario in 868 MHz was explored also in [24]. The study showed that the packet reception was possible at a distance of 2.2 km on 868 MHz. In addition, the packet reception rate was investigated when LoRaWAN protocol was deployed. Results showed that there was a small residual packet loss of 1 %.

In [25] range testing in an urban area was performed in 868 MHz band, using LoRa settings that enable maximum sensitivity and resilience to external interference bursts: SF = 12, BW = 125 kHz, and CR = 4/8. The antennas used in the experiments were omnidirectional. The experiments were carried out in two different cities with the same transceivers and antennas. In one scenario the maximum attainable range was 3.5 km, whereas, in the second 900 m; the difference reported

was explained with different terrain profiles of the city locations.

The study [26] analyzes packet loss versus two parameters, the distance and weather conditions, deploying LoRa gateway and nodes in the student campus. Both, indoor and outdoor scenarios were tested for the single LoRa setting: SF = 9, BW = 125 kHz, while the output power was set to 20 dBm. The experiments were carried out on 915 MHz using low-cost omnidirectional rubber duck antennas. The results showed that the maximum distance achieved was 1.15 km with packet loss of almost 85 %. In addition, the correlation between the rain and packet loss was derived. Namely, during the interval of light rain, the packet loss was increased by almost 20 %.

Finally, the work presented in [27] provided simulations of LoRa links in an urban area scenario. Firstly, the theoretical background on link performance and measurement model was given, and simulation modules developed for the ns-3 simulator were presented. The simulation results of throughput performance, the probability of successful reception of a packet, and gateway coverage assessment were given. They revealed that LoRaWAN scheme provides the higher throughput than ALOHA protocol. Furthermore, the results revealed that LoRaWAN architecture can scale well and that a single gateway serving approximately 15 000 devices can deliver packets to nodes with a success rate of 95 %.

2.4.3 Mixed Experimental Scenarios

This section presents the results from different field experimental scenarios. Mostly, these experiments were carried out to gain a deeper insight into the LoRa technology in terms of range, packet delivery rate, susceptibility to interference in two characteristic experimental scenarios: LOS and obstructed LOS.

In [28] an experimental evaluation of the reliability of LoRa communication was investigated in three different experimental scenarios: outdoor in LOS mode, underground covered by a metal manhole, and indoor. The variety of LoRa parameter sets was investigated, combining all three LoRa bandwidths, minimum and maximum coding rate, and following spreading factors: 7, 9, and 12. Also, the impact of the temperature on the received signal strength and packet reception rate was

explored in laboratory conditions. The work suggested that when the nodes are on the boundary of the link margin, the use of the fastest PHY setting and the highest RF output power is more efficient than selecting slower settings that maximize the sensitivity of the receiver. The study also revealed that the RSS linearly decreases when temperature increases, showing a trend of 1 dBm per every 10 °C.

The exploration of different antennas and environmental factors is provided in [29]. The packet delivery rate in LOS scenario on 800 m long propagation path was compared to 200 m long blocked LOS in the mountain area obstructed with vegetation. In addition, experimental work provided an insight into link reliability when different antennas are used; furthermore, the measurement results also confirmed the impact of temperature on the packet receive signal strength, presented in [28].

In [11, 30] range evaluation, channel models, Doppler robustness and scalability of LoRa technology were investigated. The experiments in [30] demonstrated that LoRa communication is possible over seawater at distances up to 15 km in 868 MHz band, but with a significant packet loss (30 %). The results also revealed that communication is possible up to 10 km over land in the same frequency band, with packet loss of 40 %. The path loss models for both scenarios are also provided. On the other hand, in [11] it was shown that when the SF = 12 was selected and relative speed of the mobile node exceeded 40 km/h, the communication performance significantly deteriorated.

The performance evaluation in LOS and blocked LOS environment on 915 MHz is given in [31]. The objective of the research work was to investigate the suitability of the LoRa technology for IoT applications. The link lengths were varied in steps of 100 meters, up to 700 m for the LOS propagation condition, and up to 400 m for obstructed LOS. During the experiments the RSS was recorded, experiencing variations from –50 dBm to –100 dBm for the shortest and longest propagation path confirming the suitability of the technology to be deployed in IoT applications.

The LoRa network performance comparison deployed in an open area and tree farm based on PHY factors is given in [32]. The experiments were conducted on the 200 m long links. The RSS and Packet Delivery Rate (PDR) were logged. The

results revealed that PDR is more sensitive to PHY factors in the tree farm; the open area yields better PDR, as well as higher levels of RSS.

The channel characterization in the Antarctic between mobile LoRa node and a base station in two frequency bands, 868 MHz and 434 MHz is presented in [33]. Two propagation conditions were investigated: LOS, and blocked LOS. The results showed that distances up to 30 km can be easily covered with standard output power, 14 dBm, using an omnidirectional antenna at the transmit side. In addition, blocked LOS links are also possible but their reliability is not guaranteed.

There are several general studies of LoRa technology which consider the theoretical background of LoRa modulation technique and provide some basic demonstration experiments. For example, in [34–37], theoretical analysis of LoRa parameters and their impact on sensitivity, bit rate, and packet airtime is presented. In addition, the overview of LoRaWAN protocol is given, and its suitability for LPWANs is studied. The LoRaWAN scalability is analyzed, as well as the probability of packet collisions in such networks. Furthermore, LoRa coverage experiments inside the city are carried out, confirming the results and conclusions already presented in other works.

Various research groups addressed the problem of interference and coexistence of different sensor networks that use distinct types of modulation. In [38, 39] interference measurement in ISM 868 MHz band with focus on LoRa and SigFox technology is presented, and LoRa protocol performance assessment in critical noise conditions is explored. The results revealed that there is a probability of approximately 23 % of interference in active city areas such as shopping malls, while in passive areas the probability significantly decreases down to 3 %. In addition, in [39] it is shown that LoRa technology provides very high link reliability even in the presence of high power Gaussian noise in the channel.

In [40, 41] LoRa scalability was investigated with a simulation model based on interference measurements, and mitigation of inter-network interference was studied. The results showed that when LoRa is deployed and LoRaWAN protocol applied, the successful packet delivery rate is six-times higher within LoRaWAN than using competitive technologies. On the other hand, in [41] it is shown that interference

can potentially drastically reduce the performance of LoRa network, and that deployment of multiple base stations gives an advantage in comparison to the use of directional antennas.

Several research studies, namely [42–44], provided the evaluation of LoRa receiver performance under co-technology interference, as well as node-to-gateway connectivity analysis. The studies reveal that LoRa can still provide high packet reception rate in the presence of time-synchronized packets transmitted by multiple transmitters with an identical spreading factor. On the other hand, in [43] it is shown that LoRa can be a potential interference threat to IEEE 802.15.4g networks, affecting one or more channels, depending on LoRa bandwidth deployed. Finally, the simulations provided in [44] revealed that LoRa network performance strongly depends on the deployment scheme of gateways and that careful network planning is needed to provide high connectivity and coverage.

Security vulnerabilities of LoRa are investigated in [45]; it has been shown that security is already a major challenge in such networks and that the long-range links are particularly vulnerable to multiple security attacks. Moreover, it has been demonstrated that attacks can be carried out using low-cost commercial hardware. In [46], a secure smart metering infrastructure is proposed, based on symmetric cryptography to protect end-to-end communication between the gateway and the end node. The proposed scheme was tested and verified in laboratory experiments.

In numerous research works, LoRa technology was applied in the design and implementation of systems that can be potentially used in commercial applications. In [8, 47–60] different systems to be deployed in smart cities for environmental monitoring, remote health monitoring and smart metering are presented. In addition, systems for remote measurements in coastal regions, early warning systems for disaster prevention, and different security monitoring systems are presented.

Due to inherent characteristics of spread spectrum types of the modulations, LoRa technology cannot be used for implementation of accurate tracking systems. However, in [61–64] LoRa was used as an underlying communication technology in tracking systems, enabling long-range transmission of position parameters to a base station. On the other hand, in [65–70] various application scenarios in agriculture are

presented, where LoRa is used to extend the range and lower the power consumption of different measurement systems used to automate some of the processes in plants growing, such as e.g. irrigation. Moreover, different use cases are presented where LoRa is deployed to lower the cost of the systems used in smart farming and simplify their deployment due to extended coverage capabilities.

Finally, [71–79] present various deployments of LoRaWAN networks, as well as networks using customized communication protocols; in addition, successful data acquisition and transmission have been demonstrated. These use case scenarios proved the suitability of such protocols and networks in systems which require high resilience to interference and co-existence with other technologies used in LPWANs.

2.4.4 Bridging the Identified Gaps

The current state of the art in the area reveals that all research studies carried out so far are limited to the investigation of short LoRa links, despite the fact that the LoRa technology was developed to enable very long links. Furthermore, the amount of traffic generated during the experiments was too low to provide deeper insight into link behavior since the maximum number of sent packets in each experiment did not exceed 3500. To assess link behavior and provide enough data for statistical processing, usual engineering practice recommends transmission of at least 10 000 packets. Next, experimental data are presented cumulatively, in the form of packet loss, therefore no insight into link behavior over time can be gained. Further, the restricted selection of LoRa parameters deployed in the experiments cannot provide general insights in the link behavior because parameters are either selected to enable maximum sensitivity of the transceivers, or to take into account trade-offs between power consumption, data rate, and transmission delay. Besides, only one frequency band is usually investigated, hence advantages of using one ISM frequency band over another cannot be quantified. Moreover, commonly one pair of commercial LoRa transceivers was used in the experiments, which can limit the insight in the technology capabilities, especially if we take into account the fact that commercial transceivers are usually not optimized in terms of sensitivity and immunity to external interferences [80]. As a further matter, most

works lack systematic measurements of RSS and SNR of received packets, which prevents parametric analysis of link behavior. Furthermore, in works where such measurements are performed, scaling factors for RSS indicators are not provided, and linearity and saturation region of SNR measurement chain was not determined; however, to provide an accurate interpretation of the measurement results and valid conclusions, these steps are mandatory. Finally, no study explores long and ultra-long LoRa links using comprehensive sets of LoRa parameters in two different ISM bands simultaneously, and there is no systematic study of LoRa transmission over seawater that would explore the feasibility and reliability of such links.

To bridge the identified gaps in the current state of the art, firstly novel LoRa transceiver must be developed which would have improved characteristics in terms of sensitivity and immunity to external interferences. This is necessary because the real capabilities of the LoRa technology can be masked by deploying commercial transceivers in the experiments since their implementations include various design trade-offs which degrade the overall performance of the transceiver. Next, calibration of RSS indicator has to be performed and SNR measurement chain investigated in terms of saturation region identification. Finally, such an experimental device has to be deployed in long and ultra-long links, investigating the feasibility and temporal behavior of such links. In this way, the identified gaps would be fully addressed.

Chapter 3

Design and Implementation Methodology of Novel LoRa Transceiver

In this chapter, we present the requirements that novel LoRa transceiver has to fulfill. In addition, we define the problem statement, introduce the general model of the transceiver, and explain the design methodology used to develop it. Furthermore, we present and discuss the simulations of the RF front-end. The final PCB layout of the proposed transceiver is provided, as well as the simulation results which confirm desired characteristics. The transceiver implementation is briefly discussed. Finally, firmware functionality requirements are given, and concrete implementation is presented.

3.1 Novel LoRa Transceiver Requirements

When discussing the requirements for wireless devices which are to be used in scientific experiments or deployed in some of the myriads of IoT applications in industry, there are several requirements that each of them has to fulfill, and they are divided into two groups, namely behavioral and functional. By behavioral requirements, we refer to all the use cases where the transceiver is supposed to be used. On the other hand, by functional requirements, we refer to all technical characteristics that transceiver has to meet.

As far as the behavioral requirements of the new LoRa transceiver are concerned, it is meant to be used primarily by the scientific community that explores LoRa

transmission systems, particularly the physical layer. In industry, however, it is meant to be used as a communication module with high sensitivity deployed within a complex system providing extended range capabilities.

The behavioral requirements dictate which functional requirements the transceiver must meet, consequently implying all the sub-blocks of the transceiver. Since the main purpose of the new transceiver is to measure link parameters, such as RSS and SNR, it is convenient to have a flash memory which would enable logging of the results, thus eliminating the need to connect the transceiver to some external device, avoiding bulky experimental setup. Additionally, this approach reduces the possibility for the noise generated in the external device to be coupled to the transceiver via cable (conductive emissions) or by radiated emissions. Next, the transceiver should be capable of operating in different frequency bands, which may additionally simplify the experimental setups where the transceiver is intended to be used, or lower the overall cost of the device if it is meant to be used in some industrial application as a communication module. Further, to extend the range of applications where it can be used, a simple connection to external sensors has to be also enabled using some of the standard buses, such as I2C, SPI, or UART. To enable convenient interaction with the user, some kind of signalization should be provided such as LEDs, as well as push buttons, etc.

Furthermore, since most of such devices are battery-operated, it is very important to enable a low-power operation of the transceiver. Also, the mechanical design should be compact, providing a simple connection to host boards in the applications where it is necessary. In addition, the transceiver must be also capable of operating as a standalone unit as well, offering the flexibility when it comes to its deployment.

Finally, the sensitivity, which is the most important characteristic of a wireless transceiver, must be increased as much as possible since it directly impacts the packet error rate and the maximum attainable range. This is needed to gain a deeper insight into LoRa technology capabilities because in this case the real capabilities will not be masked by the poor hardware design of the transceiver which has the major effect on the sensitivity of the transceiver. On the other hand, the cost of the commercial application, in this case, would decrease since extended ranges eliminate

the need for increased number of gateways, which are the most expensive elements of the network.

Comparing the technologies used in IoT and LPWANs, LoRa technology inherently provides the highest sensitivity. That implies that LoRa devices can detect very weak signals, even below the noise floor, thanks to the coding gain provided by the chirp spread spectrum modulation employed. However, to fully exploit the advantages that LoRa technology offers, a careful PCB design must be performed.

Achieving a low noise floor is a complex task and requires combining different design methodologies. To lower the noise floor, one has to know all the sources of the noise that can impair packet reception in the potential transceiver design, as well as their coupling and transfer mechanisms through the PCB. Combined with all other requirements presented earlier in this chapter, it is clear that such a task cannot be successfully accomplished using only theoretical knowledge and engineering practice. There must be deployed an iterative process that includes simulations which can provide a deeper insight into the frequency characteristics of the PCB, and therefore, offer the possibility to improve the overall performance.

The ultimate goal is to design the transceiver that would have a 3 dB better sensitivity than it is specified in the corresponding datasheet of LoRa modem IC used to develop the new transceiver. The goal is perhaps counterintuitive, but it is achievable provided that the PCB design of the new transceiver has a lower noise floor than the PCB developed by the manufacturer used to measure sensitivity. In addition, the aim is to compare the sensitivity and immunity to the external interferences of the new LoRa transceiver with two widely adopted commercial LoRa transceivers and show the new LoRa transceiver's superior performance.

3.2 Transceiver Design Methodology

The devices used in IoT systems have special requirements in terms of hardware design since they consist of digital, RF, and analog sub-blocks. This makes the design of such devices complex because RF and analog sub-blocks need to be isolated from noisy digital sub-blocks. In addition, the power supply of these sub-blocks

must be very clean in order to avoid noise coupling to low-noise amplifiers through power supply rails, which may result in an increase of the noise floor, consequently degrading the sensitivity.

There are some general rules and techniques which may be applied to cope with the mentioned issues. Nonetheless, due to the peculiarities of each PCB, they do not always yield good results. However, to be able to secure the positive design outcome, the traditional design methodology has to be upgraded with several design steps which are given below.

The first step in the methodology we applied for the purpose of developing the novel LoRa transceiver was to design a block diagram of the transceiver based on behavioral and functional requirements. This step is very important since it gives the general insight into the PCB that will be designed and directs the developer in the rest of the design process.

In the second step, the adequate components were selected keeping in mind behavioral and functional requirements. Special care was exercised in choosing the packages of the components, due to the reasons given later in this chapter. This step enabled the schematic to be drawn, and circuit level simulation of impedance matching networks to be performed.

After this phase, the design is prepared to be translated into a real domain, i.e. to PCB layout. This stage does not involve abstract circuit elements anymore, but each component is represented by its footprint which reflects the physical size of the component. This implies that physical dimensions of the PCB can be determined. Nevertheless, this is not a straight-forward task since there are three additional parameters that have to be taken into account: the mechanical outline of the transceiver's enclosure, partitioning of the PCB, and component placement. It is worth mentioning that the mechanical requirements in this stage have a slightly higher priority than electrical. The results of this stage are the defined enclosure, and mechanical outline of the PCB.

The steps provided are common for virtually any hardware development process. However, to successfully cope with the noise on the PCB, additional steps are required. Firstly, we developed the PCB model of the transceiver and identified the

major contributors to the noise floor increase. In other words, the model helped us to detect the sources of the noise, as well as coupling and transfer mechanisms through the PCB. Using that, we were able to develop adequate routing strategy which focused on noise reduction in RF sub-block of the transceiver.

In the final stage, we routed the PCB. It is worth mentioning that we used the advantage of 2.5D field solver to tune the layout and improve the overall characteristics of the transceiver in an iterative process. Also, we developed the test firmware which was used to verify the basic functionalities of each sub-block of the transceiver, as well as the more advanced version which was used in both laboratory and field experiments. The methodology presented in this section is summarized in Fig. 3.1.

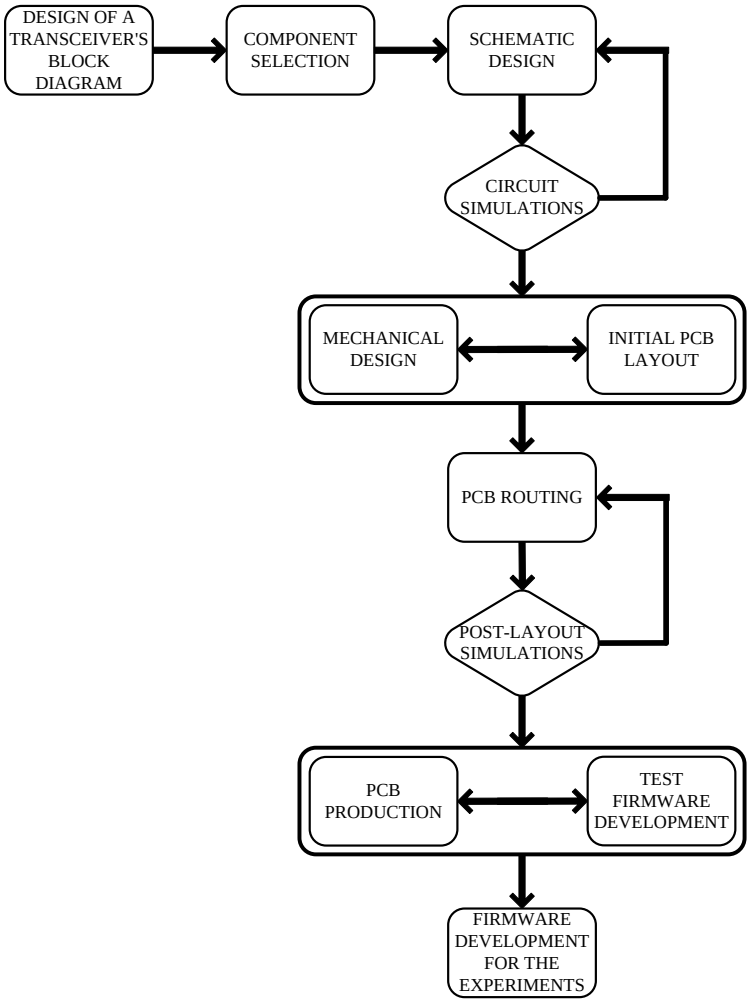

Figure 3.1: Transceiver design methodology summarized in flow chart.

3.3 Hardware Development and Implementation

Hardware design is the critical part of the transceiver design bearing in mind demands for high sensitivity and immunity to external interferences. We start with an explanation of the block diagram of the transceiver that fits behavioral and functional requirements. The corresponding transceiver's block diagram is given in Fig. 3.2.

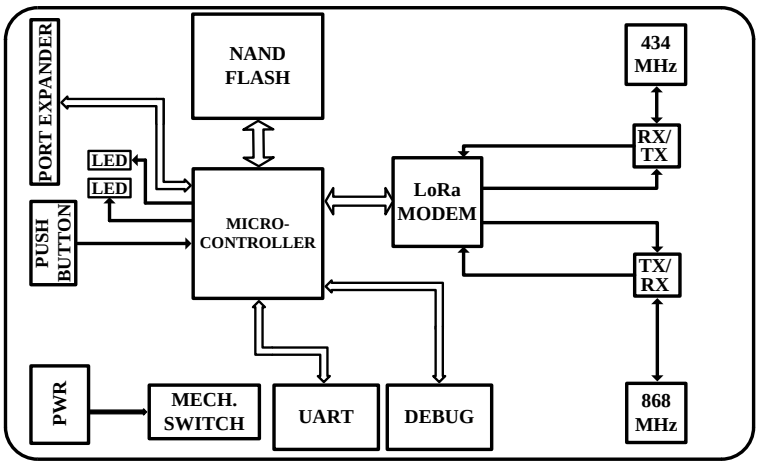

Figure 3.2: Transceiver block diagram.

As can be observed, a microcontroller manages the operation of the transceiver which is connected to LoRa modem and NAND flash. On the other hand, the port expander provides microcontroller bus extensions such as I2C, SPI, and UART. Push button and two LEDs enable user interaction. There is also an additional dedicated UART port, implemented to provide the connection of external devices since the port expander connector provides the connection to a carrier board.

The power connector is connected to the three-pole switch, which can turn off the transceiver, power it from the battery, or use the debugger's power supply. This was done on purpose, to simplify power supply of the transceiver during firmware development phase since, in that case, there is no need to connect battery together with debugger thus providing a simple manipulation with the transceiver.

As can be seen in Fig. 3.2, the transceiver modulates signals at two operating frequencies with separated RX/TX paths for both frequency bands. Separated

RX/TX paths are chosen because the attenuation in receive path is lower in this case. Paths are separated with RF switches whose operation is controlled by the microcontroller.

3.3.1 Transceiver Component Selection

We opted for EFM32GG990F1024 [81] microcontroller from Silicon Labs to manage the operation of the transceiver. It is selected due to unparalleled power consumption in both active and sleep modes. The core of the microcontroller is 32-bit ARM Cortex-M3 that can operate on up to 48 MHz. It provides DSP instruction support, as well as floating-point unit and memory protection unit. The microcontroller has 128 KB of RAM memory and 1024 KB of flash memory. It also incorporates a variety of peripherals: timers, DMA controller, integrated LCD controller, external bus interface, TFT controller, UARTs, SPIs, and I2Cs. Besides that, there are also low-energy UARTs which can operate autonomously with DMA in deep sleep mode. Additionally, there is a fully USB 2.0 compliant bus with on-chip PHY and embedded voltage regulator.

Furthermore, there is also a plethora of analog peripherals: 12-bit A/D converters, on-chip temperature sensor, 12-bit 500 ksamples/sec D/A converter, analog comparators, operational amplifiers, etc. These peripherals simplify the connection of analog sensors to the transceiver and minimize Bill of Material (BOM) of the carrier board equipped with sensors, therefore lowering the overall price of the LoRa node. It is also important to mention that operating temperature enable the transceiver to be deployed in extreme weather conditions since the operating temperature range is $-40°$ C to $85\,°$ C.

A NAND flash is used to store measured data. We opted for the capacity of 32 MB, deploying NAND256-A from Numonyx. The density of the memory is 256 Mbit, with 8-bit bus width. The page size is 512 byte with 16 spare bytes, while block size is 16 Kb with 512 spare bytes. The memory provides One Time Programming (OTP) area, and each IC has a unique ID (serial number).

Due to a requirement for two operating frequency bands of the transceiver, we opted for SX1276 from Semtech. The SX1276 [82] includes LoRa modem, (G)FSK

modem, and OOK modem. It provides a very huge link budget, according to the datasheet, up to 168 dB. In addition, it has two different RF ports that can be set to operate in three frequency bands: $137 - 175$ MHz (low-frequency port), $410 - 525$ MHz (low-frequency port), and $862 - 1020$ MHz (high-frequency port). The modem is capable of providing 20 dBm of constant output power, which can be used on both ports, namely low-, and high-frequency.

Power consumption in receive mode is low, achieving 9.9 mA, while for registers' retention only 200 nA is needed. In transmit mode, the current consumption can be limited to the desired value by setting the value in the corresponding register, making this feature useful in battery-operated systems.

The packet engine of SX1276 can process packets up to 256 bytes with CRC, which can be controlled by setting the corresponding register. Moreover, the RSS and SNR of each packet are available upon the packet reception and can be read from the corresponding register via SPI bus. The packet reception can be improved by adjusting the Low-Noise Amplifier (LNA) gain, however, this mode of operation implies higher power consumption.

As far as LoRa parameters are concerned, the SX1276 offers utilization of a variety of parameters. For example, it can modulate signals within several different bandwidths, such as: $7.8, 10.4, 15.6, 20.8, 31.2, 41.7, 62.5, 125, 250,$ and 500 kHz. However, it has to be noted that, to be able to exploit bandwidths less than 62.5 kHz, the referent clock source for the modem has to be provided from the oscillator. For LoRa bandwidths equal to or greater than 62.5 kHz, the low-cost crystal can be used.

The SX1276 offers different spreading factors as well. The modem is capable of deploying spreading factors in the range of $\mathrm{SF} \in [6, 12]$. However, spreading factor $\mathrm{SF} = 6$ can be used only when implicit header mode is enabled. In addition, SX1276 provides 4 different coding rates, by adding $1, 2, 3,$ or 4 bits at each 4 bits of payload data. This makes the data transfer more resilient to external interference bursts.

The SX1276 also provides a very important feature, a low data rate optimizer, which improves the packet reception when packet airtime is long; its use is mandatory when the symbol time exceeds 16 ms.

For communication with a host processor, the SX1276 provides SPI bus and 6 I/O digital pins. Their function can be configured through corresponding registers, offering state change on a packet sent/received, or on CRC error. All this information is available in the registers as well and can be read by polling mechanism via SPI bus.

The SX1276 can operate in different modes. For example, a sleep mode provides the lowest power consumption, disabling everything except access to configuration registers and switching between two modes, namely between FSK/OOK and LoRa mode. In standby mode, the baseband blocks are enabled as well as the crystal oscillator, while in the frequency synthesizer mode PLLs are locked for transmission/reception but the RF part is off. Finally, in transmit/receive mode the RF part is on and is fully initialized to send/receive packets. Here it is important to emphasize that when SX1276 transmits the packet, it automatically goes to standby mode.

The SX1276 provides two reception modes: Rx Continuous and Rx Single. When the SX1276 is in the continuous reception mode, upon receiving a packet, it stays in the same operating mode until the modem is put in another operating mode by setting corresponding registers. Contrariwise, in the Rx Single mode, after receiving the packet, the SX1276 goes to standby mode automatically.

Scanning the channel occupancy in spread spectrum systems is inherently complicated, however, the SX1276 provides Channel Activity Detection (CAD) mode of operation where it is possible to detect other LoRa signals in the channel. This may be very useful to avoid collisions and increase the packet reception rate in different LoRa applications. In addition, the modem offers RSS and SNR values of the received packet, which are available in the corresponding register.

To separate RX/TX paths, two RF switches PE4259 from Peregrin Semiconductor are used. The switch covers a broad range of frequencies $10 - 3000\,\mathrm{MHz}$, and can be controlled either using a single pin or complementary control inputs. The insertion loss of the switch is very low, yielding $0.35\,\mathrm{dB}$ at $1\,\mathrm{GHz}$. Maximum allowed power at $1\,\mathrm{GHz}$ is $32\,\mathrm{dBm}$ which allows the maximum output power of SX1276 to be used. Maximum switching rate is $25\,\mathrm{KHz}$, which enables the use of all sets of

LoRa parameters to transmit/receive packets with no inter-packet delay time.

The power supply is implemented using the TPS73633 from Texas Instruments. This is a low-dropout regulator which can tolerate input voltages in the range of $1.7 - 5.5\,\mathrm{V}$, enabling the use of a lithium-polymer battery as the main power supply. A very low quiescent current, less than 1 uA in shut down mode fits the battery-operation requirement. In addition, it can source up to 500 mA at 3.3 V and provide stable regulation over a wide range of output capacitors. A very precise, band-gap reference is used to generate the internal reference voltage, generating approximately $30\,\mu\mathrm{V}_{\mathrm{rms}}$ in the bandwidth of $10 - 100\,\mathrm{kHz}$.

3.3.2 Transceiver Schematic Design

The schematic of the transceiver consists of the two sub-blocks: digital and RF. The digital sub-block encompasses the microcontroller, NAND flash, port expander, and user interface, while in RF part LoRa modem and RF front-end are included. The digital part of the transceiver does not pose a significant development challenge since there are no high frequencies (up to 48 MHz), and no short rise times of the digital pulses (nano-second domain).

On the other hand, the development of the RF sub-block requires a careful approach. Special caution must be exercised in the following design steps:

- the impedance matching of the RF IC pin output impedance to a PCB trace impedance,
- the design of harmonics filter,
- the impedance matching of the antenna to the PCB trace impedance.

The output impedance of the RF IC pin is usually complex, while the PCB trace characteristic impedance is normally designed to be $50\,\Omega$. Therefore, to enable maximum power transfer from, e.g. transmit pin of the RF IC one must implement the proper passive impedance matching network. After the impedance matching network, a harmonic filter must be realized to suppress unwanted harmonics with minimal impact on a signal to be transmitted. Here it has to be noted that the

input and output impedance of this filter must also be 50 Ω since the impedance that filter sees on both sides is 50 Ω.

The impedance matching network for the antenna maximizes the radiated power from the transceiver. Usual engineering practice when designing the RF front-end is to provide the footprints on the PCB which are later used to investigate and implement optimal matching. If the antenna impedance is 50 Ω, the footprints serial to signal being transmitted are simply shorted with 0 Ω resistors.

The proper design of the RF front-end is of paramount importance because it determines the attenuation which will experience the transmitted or received signal. This has a direct consequence on maximum achievable output power, as well as the sensitivity of the transceiver. The usual engineering practice is to simulate the RF front-end in terms of the insertion loss in the frequency band of interest in order to confirm the desired characteristics, and then to proceed to route the PCB.

To be able to design the impedance matching networks, one must know the output impedance of the corresponding pins of the IC used as a LoRa modem. The AC analysis has to be performed in the frequency range of interest, and ideally, the attenuation at desired frequencies has to be 0 dB. In Fig. 3.3 we present the RF front-end recommended by the manufacturer [83] of the LoRa modem for the transmit mode at 868 MHz together with the transmit pin output impedance and the load we used in our SPICE simulation. The load impedance of 50 Ω is selected since it is the impedance of the antenna used in the field experiments at a frequency of interest.

As can be seen in Fig. 3.3, the transmit pin output impedance at 868 MHz is modeled as a serial connection of the resistance, $R = 14\,\Omega$, and the inductance of $L = 733.432$ pH. This is calculated from the complex impedance of the pin, measured by the manufacturer and provided in the corresponding application note, $\underline{Z} = 14 + j4$. The result of the AC analysis performed in LT Spice and plotted with Python's Matplotlib library is presented in Fig. 3.4.

We observe that attenuation at 868 MHz is approximately 2 dB. This result indicates that transceiver's output power could be 2 dB less than the maximum specified by the manufacturer of the LoRa modem used to implement the transceiver. In ad-

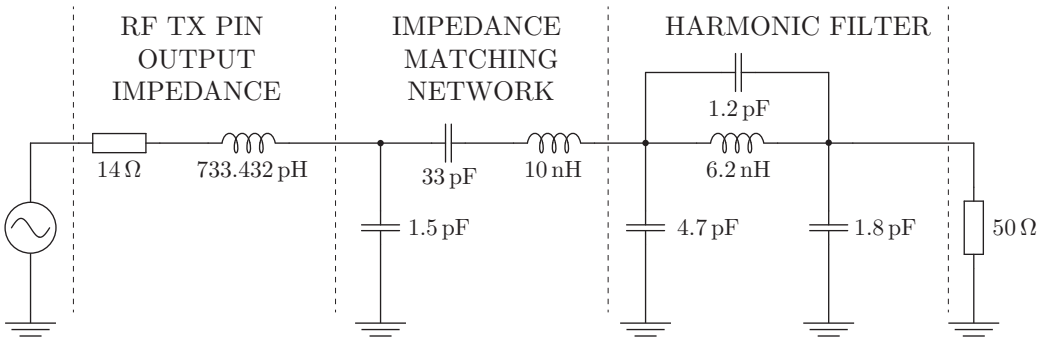

Figure 3.3: RF front-end recommended by Semtech [83] for transmit mode at 868 MHz used in SPICE simulation to determine the insertion loss.

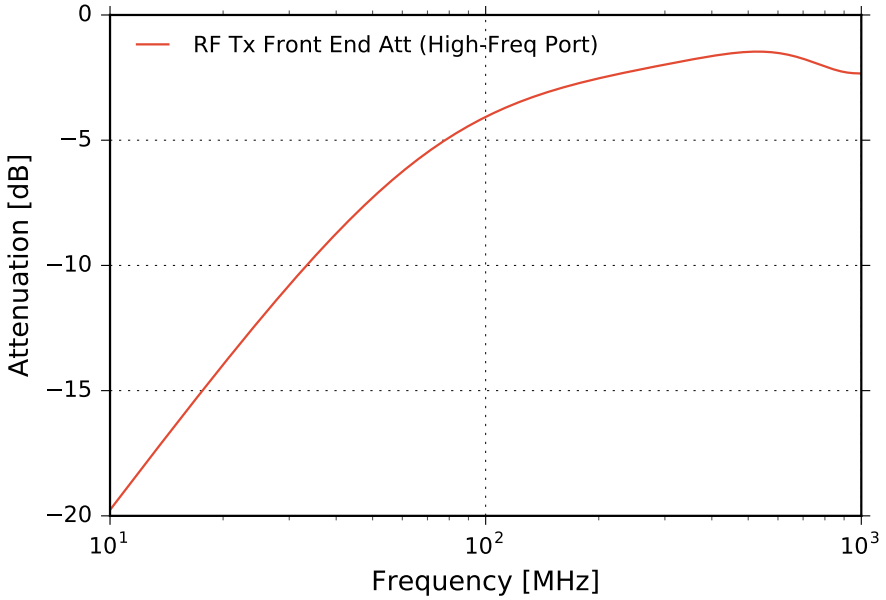

Figure 3.4: AC analysis of RF TX front-end suggested by the Semtech for 868 MHz frequency band, simulated with LT Spice and plotted with Python's Matplotlib.

dition, it can be seen that the bandwidth of the harmonic filter is tuned and centered to the frequency of interest. However, the overall attenuation is high, and laboratory measurements are required to confirm the real attenuation and tune the impedance matching accordingly.

Figure 3.5 shows impedance matching network for 434 MHz, also proposed by the manufacturer in the corresponding application note [83]. The transmit output impedance is modeled as a serial connection of the resistance, $R = 13.7\,\Omega$, and the

inductance of $L = 953.462\,\text{pH}$. These values are calculated from the complex output impedance of PA_BOOST transmit pin provided in the corresponding application note, namely $\underline{Z} = 13.7 + j2.6$. Here it has to be noted that maximum output power at PA_BOOST pin is 20 dBm. The result of the AC analysis performed in LT Spice is presented in Fig. 3.6.

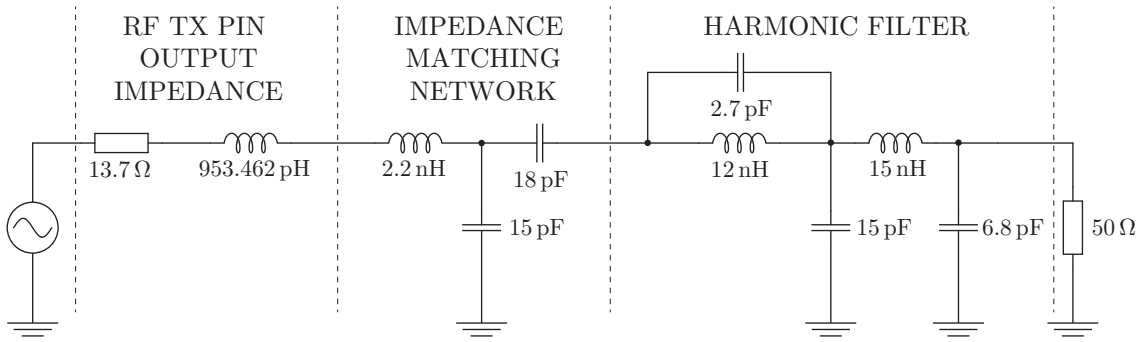

Figure 3.5: RF front end recommended by Semtech [83] for transmit mode at 434 MHz used in SPICE simulation to determine insertion loss.

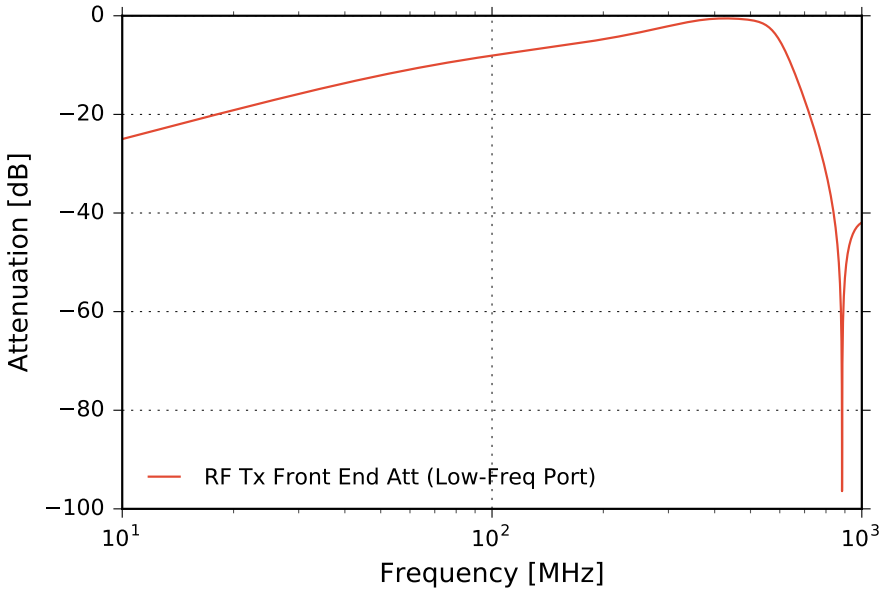

Figure 3.6: AC analysis of RF TX front-end suggested by the Semtech for 434 MHz frequency band, simulated with LT Spice and plotted with Python's Matplotlib.

We observe that attenuation at 434 MHz is almost 0 dB which is exactly what is needed to provide the maximum output power. The central frequency of the

harmonic filter is tuned; in this case, the laboratory measurements will be required only to confirm the results of the simulation.

The simulations are the last step before transferring the schematic design to the PCB design environment; the next section deals with the PCB design and layout verification through simulations.

3.3.3 Transceiver PCB Design

As already indicated, the proper schematic does not guarantee that the transceiver is going to operate flawlessly with required characteristics. On the contrary, to provide the operation in accordance with the requirements, one must ensure that the PCB design is adequate. Wireless transceivers pose a special design challenge because the PCB design impacts the sensitivity and immunity to interference significantly, which are two characteristics of paramount importance of each wireless transceiver.

PCB model used to analyze noise sources and noise transfer through the board

Based on the requirements and block diagram of the new LoRa transceiver, we present a PCB model of the transceiver in Fig. 3.7 used to analyze sources of the noise on the PCB and noise coupling and transfer mechanisms.

As can be seen in Fig. 3.7 the model includes a power supply, digital ICs, and RF IC. Depending on the type of power supply used, the power supply can be a major contributor to the noise level present on the board. For example, if switching regulator is used, it will generate the switching noise which must be filtered appropriately; failing to do so, will enable the noise to propagate through the PCB traces and planes to sensitive parts of the board; the higher their inductances, the more noise will be induced; this noise will be coupled to sensitive circuits, such LNAs which will result in increased noise floor and degraded sensitivity of the transceiver.

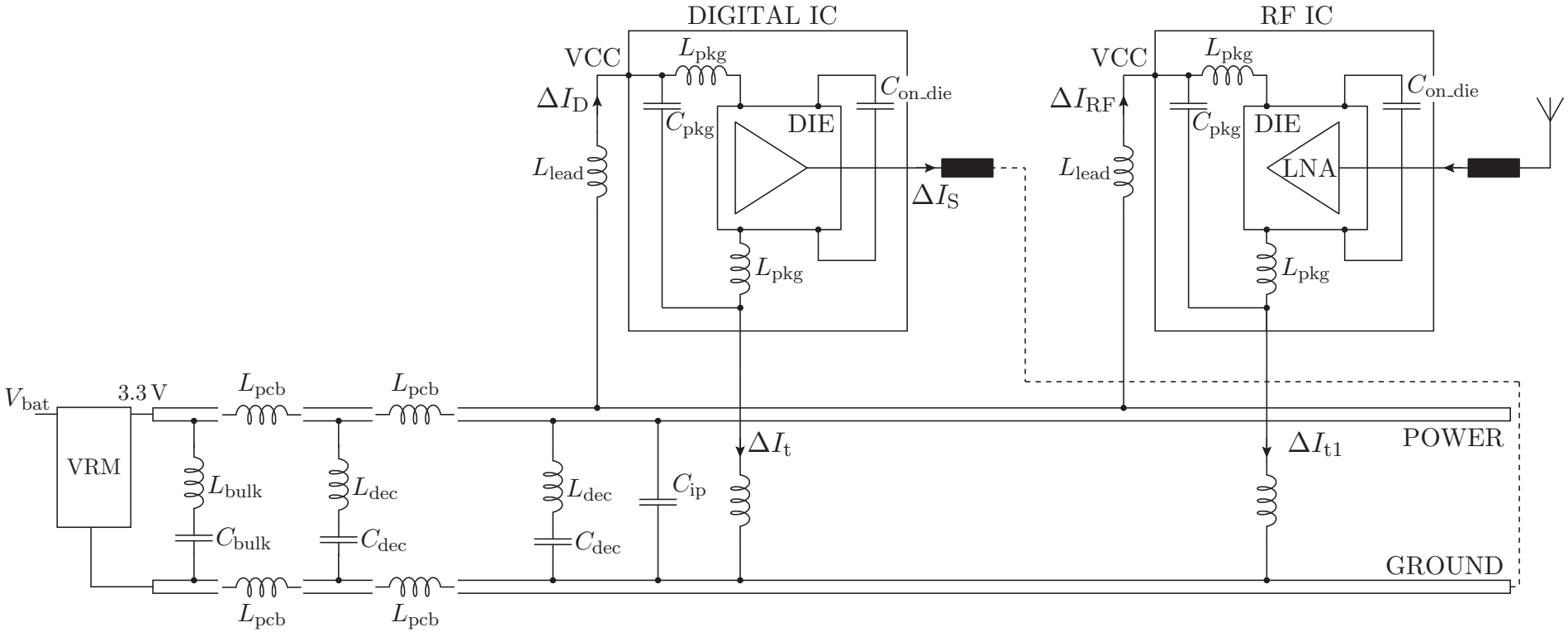

Figure 3.7: LoRa transceiver PCB model derived from [84] used to analyze noise sources and noise transfer mechanisms.

To minimize the level of the noise generated by the power supply, linear power supplies should be used. This, of course, has its downsides which are reflected in the fact that a significant amount of energy will be dissipated inside the regulator. If we take into account that the transceiver is powered from the battery, the effects of deploying a linear regulator become obvious. The solution is to use a Low-Dropout (LDO) linear regulator with the high Power Supply Rejection Ratio (PSRR) over a broad frequency spectrum.

Besides this, the inductances on the board must be minimized, as well as parasitic capacitances, to suppress the noise transfer through the board. This can be accomplished by using a proper routing strategy and adequate IC packages. Namely, to decrease trace inductances, wider trace geometry has to be applied. When changing the routing layers, the usage of vias with bigger diameter should be adopted since it provides lower inductance loops. Furthermore, the package of the ICs may also play a role since the total inductance of the net will be increased by the lead inductance plus inductance of the bond which connects the pin with the IC die.

To further decrease the noise level on the PCB, it is important to design the adequate decoupling scheme of the board. For that purpose, there are three types of capacitance that can be used to filter low, mid-range and high frequencies. The bulk capacitance is used to filter low-frequency noise due to high capacitance of the bulk capacitors. For mid-range values, up to approximately 100 MHz, multi-layer ceramic capacitors may be deployed since for higher frequencies they become ineffective due to their lead inductance which causes them to start to behave as inductors after the resonant frequency while their impedance increases. For high-frequency noise components, capacitors with small lead inductance have to be applied. This can be achieved only by taking advantage of the inter-plane capacitance of the PCB, C_{ip}, (see Fig. 3.7) which is formed by ground and power plane, and a dielectric between them. This capacitor inherently has virtually zero lead inductance and can be used to filter very high frequency components of the noise.

On the other hand, the impedance of the Power Distribution Network (PDN) significantly contributes to noise transfer throughout the PCB. Therefore, the main objective is to design a flat and low PDN impedance profile in the wide frequency

range. This is of paramount importance since the noise at a load point will be proportional to the PDN impedance. This implies that if the PDN impedance profile is kept low and flat, the impact of the generated noise on sensitive parts will be minimized. The main question that has to be answered in this case is in what frequency range the PDN impedance must be kept low and flat.

If we analyze what is the primary source of the noise on the PCB, we can conclude that it is the digital circuitry since there is no switching power supply on the board. The digital circuitry produces Simultaneous Switching Noise (SSN) which is a consequence of simultaneous switching of the buffers inside an IC. Since the clock frequency of the microcontroller is the highest frequency on the board, 48 MHz, we can assume that it is enough to provide low and flat PDN impedance profile in the range of 10 MHz up to 20th harmonic, i.e. 960 MHz.

Additionally, the rise time of the digital pulses can also play a significant role in creating noise due to the potentially high harmonic content of the digital signals with very short rise time. In our analysis, we will suppose that the lowest rise time is 10 % of the digital signal period generated by the microcontroller since it is the highest frequency on the board. The rise time in this case yields $t_{\text{rise}} = 2.1\,\text{ns}$. We can assume that the bandwidth of such a signal, according to [85], is:

$$\text{BW}[\text{MHz}] = \frac{0.35}{t_{\text{rise}}[\text{ns}]} = 167\,\text{MHz} \tag{3.1}$$

The above calculus shows that it is safe to set the higher frequency bound to 960 MHz, since the bandwidth of the highest rise time is 167 MHz.

In addition, special care must be exercised when designing power planes. Namely, due to their geometry, PCB dielectric properties, and via geometry used in the design, a resonant cavity can be formed between power planes. In that case, if the noise component coupled to a power supply voltage has the same frequency as the resonance frequency of that cavity, the voltage delivered to a load will have the same noise component significantly amplified. This can have detrimental effects on RF circuitry performance and it is very hard to detect these peaks by measurements. To successfully cope with this kind of problem, adequate simulations are required.

Finally, a very important part in the development of the transceiver is designing

the traces in the RF front-end using controlled impedance. This is one of the several necessary conditions that contribute to a maximum power transfer to the antenna. Therefore, the insertion loss of these traces must be minimal. To achieve that, dielectric losses must be minimized, and the proper routing strategy applied when changing routing direction.

To adequately address all the potential problems listed, we start with a careful design of the PCB stackup and dielectric selection presented in the next subsection.

Transceiver PCB Stackup

The transceiver's stackup is designed to address several trade-offs regarding inter-plane capacitance, trace geometry of 50 Ω controlled impedance, and mechanical properties of the PCB. Namely, to maximize inter-plane capacitance, the core material between power and ground plane must be as thin as possible; on the other hand, to provide mechanical strength of the board, the prepreg material thickness has to compensate for a thin core material. The thick prepreg material implies wide 50 Ω controlled impedance traces, which can pose a problem if the raster of ground pins on antenna connector is smaller than the trace width. The assumption is that Micro-Miniature Coaxial Connector (MMCX) is used for the antenna connection due to transceiver miniaturization requirement. If this is the case, the routing of transmit/receive traces might not be possible. Taking into account the listed requirements and trade-offs, we designed the PCB stackup presented in Fig. 3.8.

As can be seen in Fig. 3.8, the stackup is realized in 4 layers. The core material thickness is selected to be 0.2 mm, whereas the prepreg thickness is selected to be 0.36 mm. The copper thickness is different in different layers, yielding 0.035 mm for inner layers, while for the outer layers it is 0.018 mm. Due to a copper galvanization in outer layers, the overall thickness becomes 0.053 mm after the process. This is very important for controlled impedance geometry calculation. Finally, solder mask thickness is 0.022 mm.

We used FR-4 based material for the core and prepreg. The Panasonic R-1755V was selected for the core, while for the prepreg Panasonic R1650V was used. The

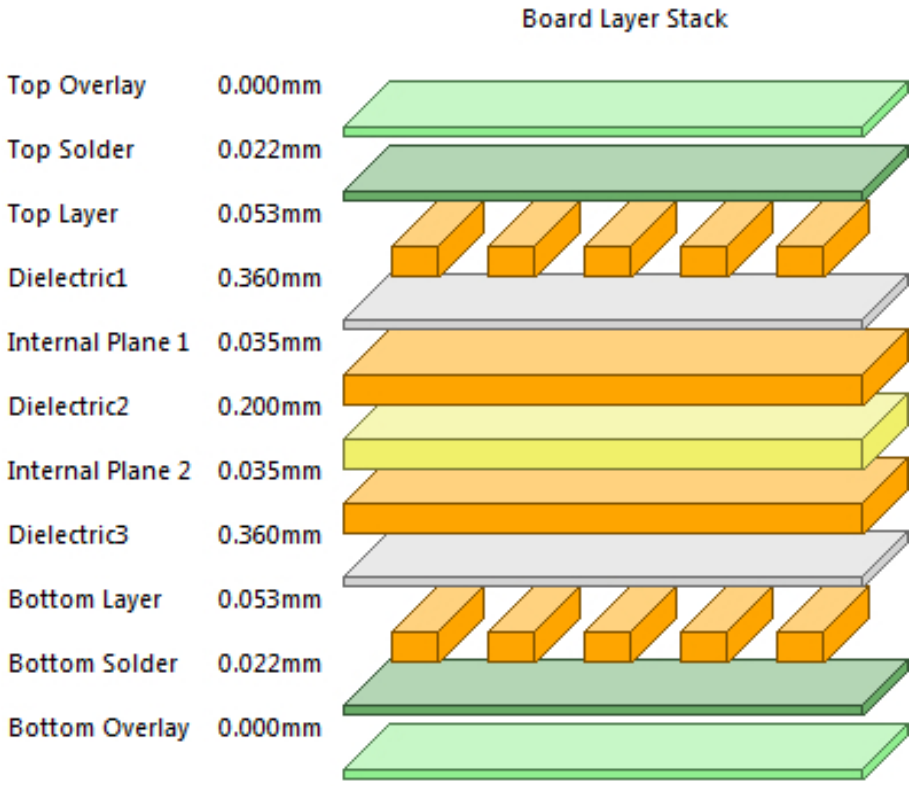

Figure 3.8: LoRa transceiver PCB stackup.

core material has a dielectric constant of $\epsilon_r = 4.45$ at 1 GHz, while the dissipation factor at the same frequency is $D_f = 0.016$. The glass transition temperature is $T_g = 170\,°C$. On the other hand, dielectric constant of the prepreg material at 1 GHz is $\epsilon_r = 4.5$, while the dissipation factor is $D_f = 0.014$. The glass transition temperature is also $T_g = 170\,°C$. The solder mask we used was blue with a dielectric constant of $\epsilon_r = 3.1$.

The microstrip designed and used for the transmit/receive traces was simulated in terms of a conductor and dielectric loss, as well as in terms of trace attenuation. The results are given in Fig. 3.9. Since the maximum trace length of the microstrip is 33 mm, it can be easily calculated that maximum trace attenuation at 1 GHz is 0.01 dB which is negligible in this case.

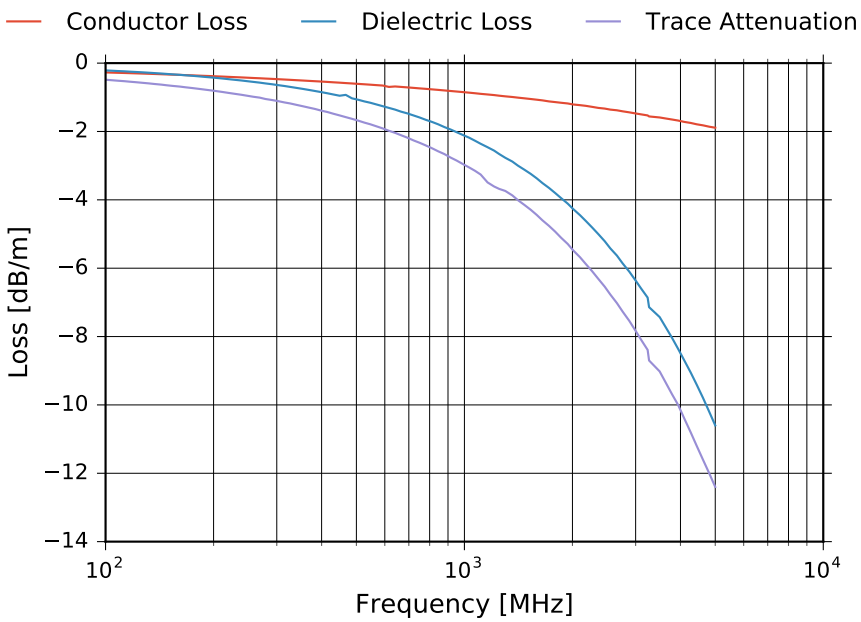

Figure 3.9: Losses of microstrip simulated in Polar Si9000 and plotted with Python Matplotlib.

Transceiver PCB Layout

In this part, we provide the PCB layout of the transceiver. It is worth noting that this is the final version obtained in the iterative process which was deployed to optimize the PCB layout using simulations. Therefore, we first present the layout and explain it briefly; after that, we present the results of the simulations of the final PCB layout version and discuss them.

As can be seen in Fig. 3.10 the four-layer PCB provides one ground, one power, and two signal layers. The PCB is divided into two regions: digital and RF region. The moat that separates these two regions can be clearly identified on internal layers as well as on the bottom layer. It is used as one of the measures to prevent the noise coupling from digital to RF part. In addition, it can be noticed that the traces that go from one domain to another are routed via "bridge" to avoid additional radiated emissions from the PCB.

The loop inductances of the component connections to power planes are minimized by providing a miniature copper fills which directly connect a component pad (without using thermal relief) to a power plane using several vias in parallel. In this way, the equivalent inductance of the vias is reduced. To further minimize the loop

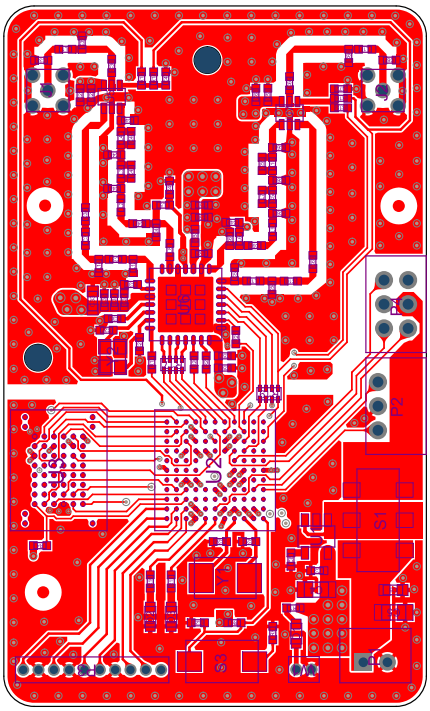

(a) Top layer

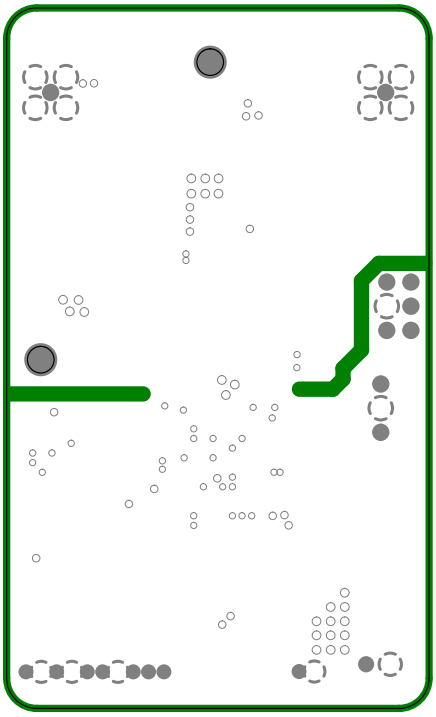

(b) Internal plane 1 (GND)

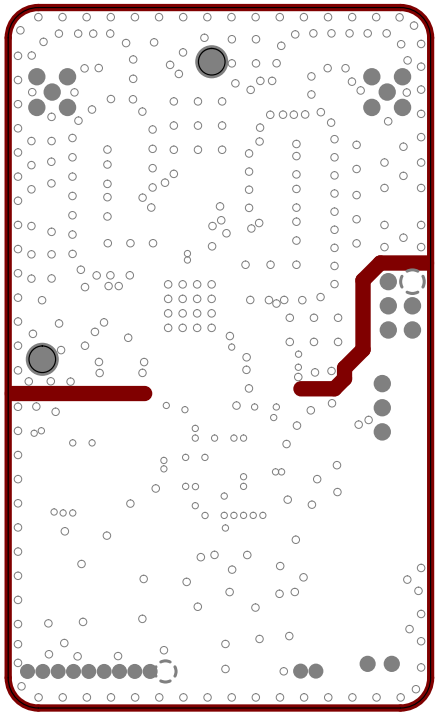

(c) Internal plane 2 (PWR)

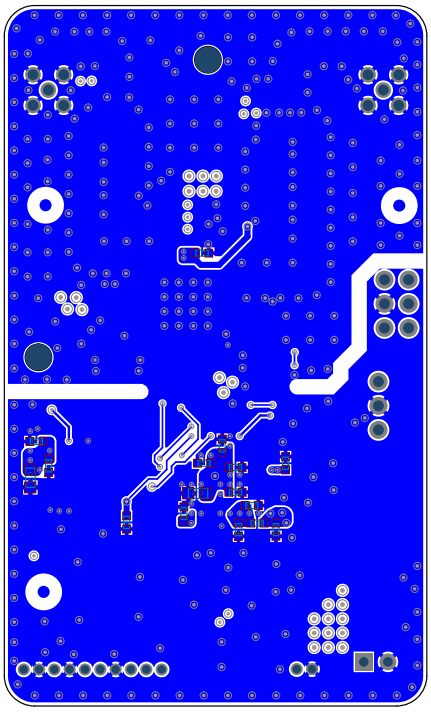

(d) Bottom layer

Figure 3.10: Transceiver PCB layers.

inductance, we used the Ball Grid Array (BGA) packages for microcontroller and NAND flash since the lead inductance for this package type is the lowest. On the

other hand, for the RF IC we used Quad Flat No-leads (QFN) package since it is the only available.

Taking into account the dielectric properties and physical dimensions of the stackup, we calculated the width of the $50\,\Omega$ microstrips used in RF front-end, which yields $W = 0.6\,\text{mm}$. To reduce the effects caused by the reflections that occur when the RF signal is injected into the microstrip, we placed the impedance matching networks as close as possible to the IC RF pins, at a distance significantly shorter than the signal wavelength (approximately by a factor 1/100). In addition, we calculated the angles of chamfered corners for microstrips to compensate for impedance discontinuities when changing the routing direction. Moreover, to further minimize discontinuities, we equipped the PCB with 0402 size components. The impedance controlled trace width is wider than the size of the pad of such components, which implies that the pad does not pose impedance discontinuity for the trace, providing no reflections on the transmit/receive path.

As can be observed, there is a significant number of vias in the RF region of the PCB. These vias are very important to preserve equipotential ground plane, which can be the source of ground noise due to possible common return current paths of several signals. On the other hand, the number of vias must not be too high because the effects of ground plane will be nullified and additional problems will be caused in that case, such as increased radiated emissions and susceptibility to external interferences.

The above was a presentation of the main steps applied in the PCB design. In the next subsection, we provide the results of simulations performed to verify the final version of the PCB layout.

PCB Simulation Results

There are a number of modeling technologies which enable simulations of PCBs. The most accurate are based on the full-wave methods; besides them, widely used are so-called 2.5 dimensional modeling technologies. Those technologies offer a balance between the accuracy of the full-wave methods and the speed of circuit-based methods [86].

As a simulation tool, we used Ansys SiWave. It is a 2.5D simulation tool that utilizes the Finite Element Method (FEM) and the Method of Moments (MoM). It is capable of solving complete layouts including the traces, planes, through-hole vias, metal thickness, and dielectric effects.

In Fig. 3.11 positions of the ports, voltage and current sources used in the corresponding simulations are presented. Their description is summarized in Table 3.1.

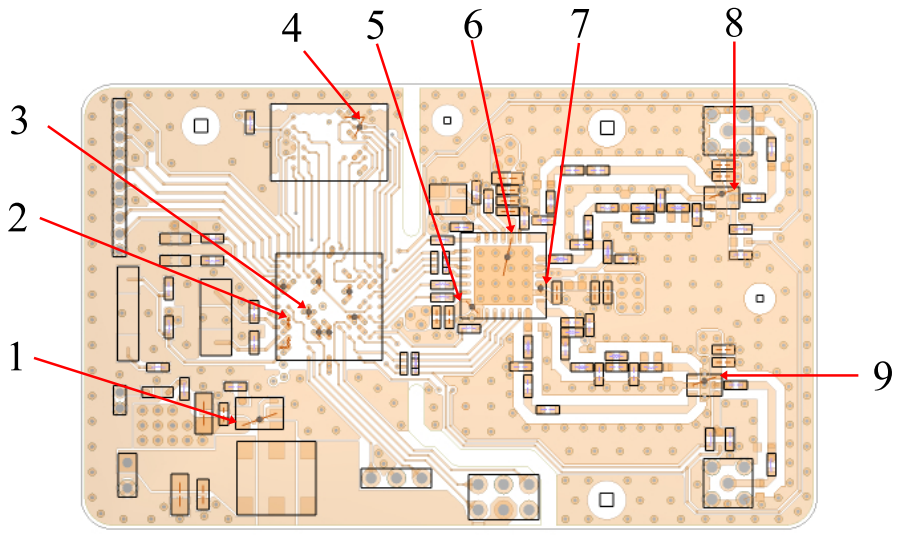

Figure 3.11: Ports, voltage and current sources used in the simulations.

Table 3.1: Positions of the ports, voltage and current sources used in the simulations.

Point	**Component**	**Pin, description**	**SiWave Element**
1	Voltage regulator	5, DVDD	port, voltage source
2	Microcontroller	K8, AVDD	port, current source
3	Microcontroller	H7, DVDD	port, current source
4	NAND flash	H7, DVDD	port, current source
5	LoRa modem	14, DVDD	port, current source
6	LoRa modem	3, AVDD	port, current source
7	LoRa modem	24, AVDD	port, current source
8	RF switch 1	6, DVDD	port, current source
9	RF switch 2	6, DVDD	port, current source

As can be noticed, the ports used in the simulations are placed on the VDD pins of the components. This is done so because we wanted to simulate PDN impedance between the voltage regulator and power pins of the ICs placed on the board. These ports are also used in the simulation of resonant modes between power planes. In the DC voltage drop simulation, instead of ports, we used voltage and current sources. The only voltage source was placed on the voltage regulator output pin while current sources configured as sinks were placed on the power pins of remaining ICs mounted on the PCB.

The first set of simulations that we performed was a DC voltage drop on power and ground planes, as well as DC current density. The voltage source was set to Vdd = 3.3 V, while the current sinks were set with a 100 % margin, implying that we doubled the current consumption of each power supply pin based on the maximum values taken from the corresponding datasheets. The board was fitted with all capacitors, inductors, and resistors during the simulation.

The DC voltage distribution on the power plane (Internal plane 2) is presented in Fig. 3.12a. The minimum voltage, blue color, yields $V_{\text{low}} = 3.297\,\text{V}$, while the red represents maximum DC voltage $V_{\text{max}} = 3.298\,\text{V}$. It can be seen that the power plane distributes nominal power supply voltage to each component on the board with minimal voltage difference across the board even for the power consumption margin of 100 %.

In Fig. 3.12c DC current density of the power plane (Internal plane 2) is presented. The blue color presents the lowest current density, which yields $J = 2.191\,\text{A/m}^2$, while the highest density is represented in red and yields $J = 1.802 \times 10^7\,\text{A/m}^2$. We observe that the highest current density is under the microcontroller. This is expected because the microcontroller has the highest number of power supply pins, and the current sinks are set with a 100 % margin. It can be concluded that this current density does not pose any problem in terms of PCB heating, and cannot lead to solder mask and/or PCB traces damage.

In Fig. 3.12b DC voltage distribution for ground plane (Internal plane 1) is given. The lowest voltage is depicted in blue and yields $V_{\text{low}} = 1.086\,\text{mV}$, while the highest voltage is presented in red, $V_{\text{high}} = 1.536\,\text{mV}$. The difference between the

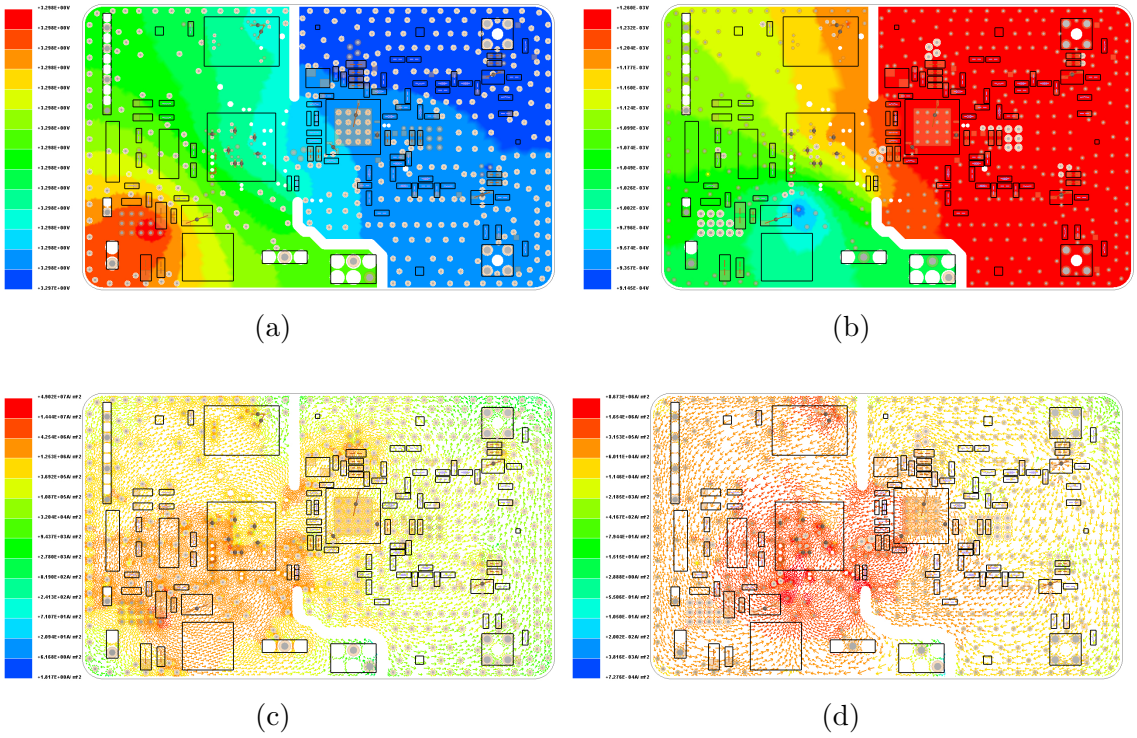

Figure 3.12: DC IR analysis: (a) DC voltage distribution on Internal plane 2 (PWR), (b) DC voltage distribution on Internal plane 1 (GND), (c) DC current density on Internal plane 2 (PWR); and (d) DC current density on Internal plane 1 (GND).

lowest and highest value is only $V_{\text{diff}} = 0.45\,\text{mV}$ which is negligible. As expected, the higher voltage drop is observed in the RF part of the board because of the moat that separates the ground plane into two regions increasing the PDN impedance of RF region slightly.

Figure 3.12d depicts the DC current density in ground plane (Internal plane 1). The lowest current density is represented with a blue color and yields $J = 8.868 \times 10^{-4}\,\text{A/m}^2$, while the highest is marked with red color and yields $J = 1.016 \times 10^{7}\,\text{A/m}^2$. The current density is the highest in the region of vias connected to ground since they are part of the return path with higher resistance than the plane.

This group of simulations shows that each component has a stable DC power supply, and also that the power planes, copper fills, and vias are properly dimensioned and can provide reliable power transfer to each point of load.

As already stated, the power planes form a cavity, potentially introducing res-

onances with a high quality factor. The resonances with high quality factor are dangerous since they will increase the power supply voltage of a component on their resonant frequency, also increasing the noise. Furthermore, if the resonance frequency is within the frequency range of interest, it can deteriorate the transceiver's performance. To cope with this problem, we performed simulations in which we determined the frequencies of resonances and their quality factors. The simulations of resonant modes between power (Internal plane 2) and ground plane (Internal plane 1) are given in Fig. 3.13, while the numerical details of resonant modes are presented in Table 3.2.

Table 3.2: PCB Resonant Modes.

Mode	**Re. Freq. [GHz]**	**Im. Freq. [GHz]**	**WL [m]**	**Q**
1	0.136170698	0.003805546	2.201593016	17.898068600
2	0.150867628	0.004389634	1.987122495	17.191806200
3	0.152298323	0.004420523	1.968455414	17.233532600
4	0.186278775	0.007810281	1.609375295	11.935705500
5	0.992072495	0.019825592	0.302188055	25.024992700
6	1.180545350	0.010588930	0.253944042	55.746558600
7	1.337296614	0.012147450	0.224177983	55.046607200
8	1.343093821	0.019752663	0.223210362	34.001466900
9	2.088486526	0.023019184	0.143545316	45.225359800
10	2.302021174	0.025640808	0.130230104	44.892579000

We observe that there are 10 resonant modes in the range of up to 2.3 GHz. The modes that are in the frequency range of interest, up to 960 MHz, have lower quality factors and do not pose a problem since the maximum quality factor in this range yields $Q = 17.89$. The first resonance with higher quality factor is at a frequency of $f_{\text{mode\_5}} = 992\,\text{MHz}$ yielding $Q = 25.02$. It is important to mention that the PCB was populated only with the decoupling capacitors during the simulation, and for each capacitor, we deployed the S-parameters provided by its manufacturer. In this way, we ensured a maximum reliability of the simulation results.

The simulations of PDN impedance were performed by placing SiWave ports on

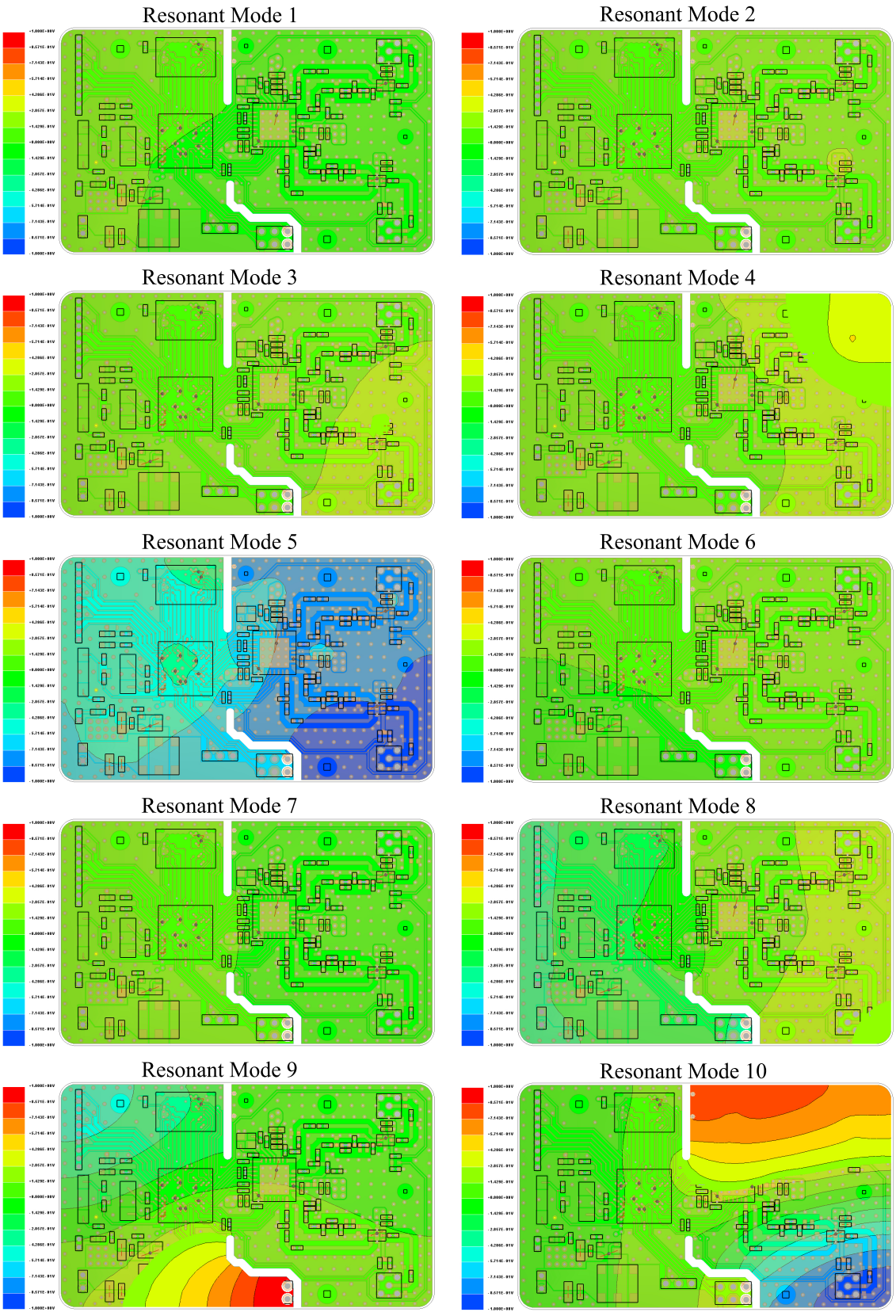

Figure 3.13: Resonant modes of the decoupled PCB. Red color on the color bar represents value 1, while blue color represents -1.

power pins of all ICs on the board. The simulation results are given in Fig. 3.14, while details of ports' designation and their placement is given in Table 3.3.

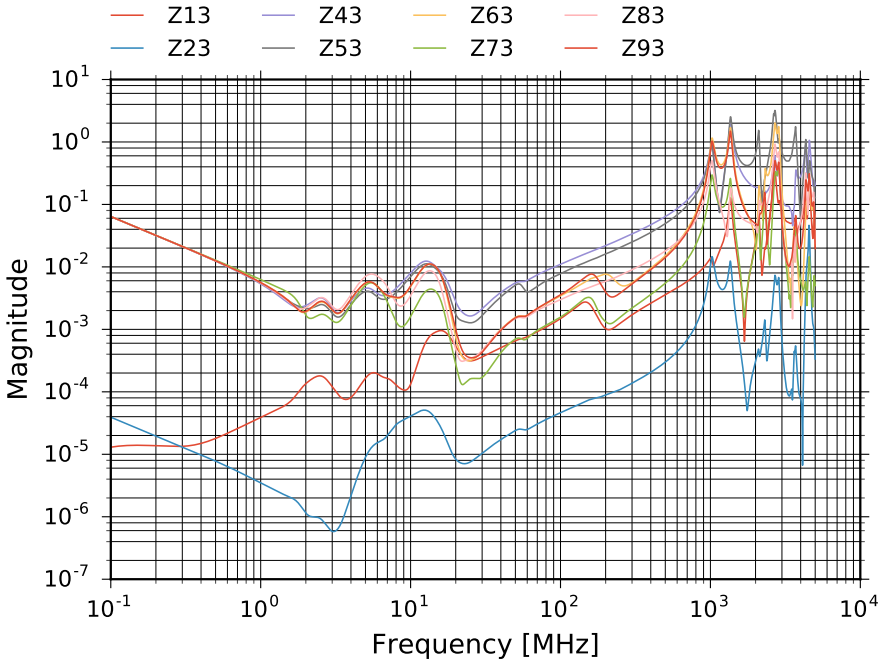

Figure 3.14: PDN impedance simulated in SiWave and plotted with Python Matplotlib.

Table 3.3: PDN impedance simulation port details.

Term	**Output port (first index)**	**Input port (second index)**
Z13	Microcontroller, pin K8, AVDD	Voltage regulator module, pin 5, VDD
Z23	LoRa modem, pin 24, AVDD	Voltage regulator module, pin 5, VDD
Z43	Microcontroller, pin H7, DVDD	Voltage regulator module, pin 5, VDD
Z53	NAND flash, pin H7, DVDD	Voltage regulator module, pin 5, VDD
Z63	RF switch 1, pin 6, DVDD	Voltage regulator module, pin 5, VDD
Z73	LoRa modem, pin 3, AVDD	Voltage regulator module, pin 5, VDD
Z83	LoRa modem, pin 14, DVDD	Voltage regulator module, pin 5, VDD
Z93	RF switch 2, pin 6, DVDD	Voltage regulator module, pin 5, VDD

As can be seen in Fig. 3.14, impedance magnitude profile is kept low in the frequency range of interest. The significantly lower profile is achieved for pin 24 of LoRa modem IC, which represents analog power supply, and for pin K8 which is also

an analog power supply for the microcontroller. This is beneficial since the analog blocks are the most sensitive parts of the transceiver. The PDN impedance profile clearly shows that the noise transfer through PDN is minimized in the frequency range of interest, which implies the lower noise floor and detection of very weak signals since LNA will have a power supply which is very clean. This is very important because LNA can amplify also noise, thus degrading SNR and the sensitivity of the transceiver.

After successful simulations of the final version of the layout, we generated the production files, manufactured, and assembled the transceiver. The transceiver size is $35 \times 58\,\text{mm}$ and the physical appearance of the top and bottom side of a bare and assembled PCB is reported in Fig. 3.15.

As can be noticed, the surface finish is Electroless Nickel Immersion Gold (ENIG). This type of surface finish was chosen since it provides a very flat soldering surface,

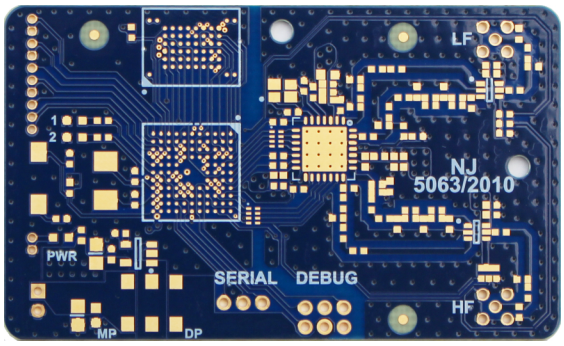

(a) Bare PCB - Top Side

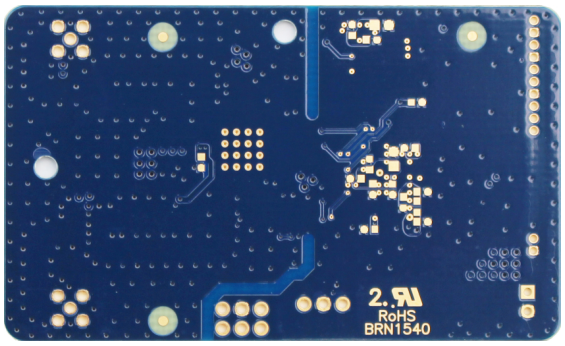

(b) Bare PCB - Bottom Side

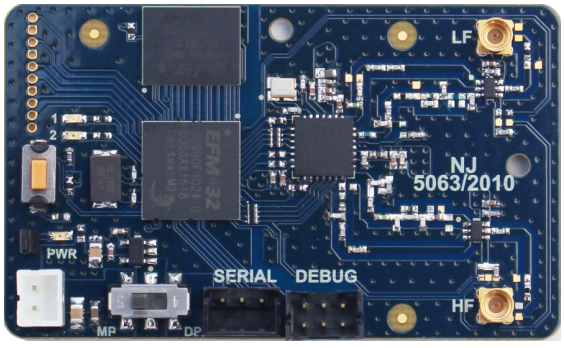

(c) Assembled PCB - Top Side

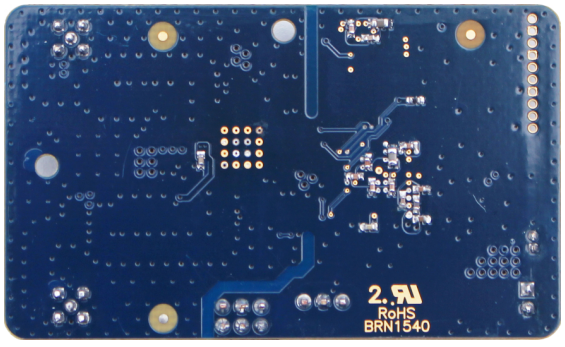

(d) Assembled PCB - Bottom Side

Figure 3.15: The physical appearance of top and bottom side of a bare and assembled PCB.

and was required in order to provide reliable soldering of BGA components. It can be seen that port expander is not mounted; this was done so because we did not need to connect any external sensor during the experiments, and it was simpler to mount the transceiver in the enclosure without the connector. The transceiver prototypes were manually assembled, however, there are 6 fiducials placed on the PCB to enable automatic assembly with the pick&place machine, as can be seen in 3.15.

3.4 Firmware Design

The operation of the transceiver is managed by the microcontroller. To be able to test functionalities of the prototype of the transceiver we developed test firmware which aimed to test each peripheral on the board, as well as LoRa connectivity. This firmware was later used only to test newly assembled boards and was not used in the experiments.

On the other hand, we developed new version of the firmware that we used exclusively in the experiments. That version covered all experimental scenarios, including both transmit and receive modes. Besides that firmware version, we developed a set of small standalone firmware applications that we used for simple operations such as dumping experimental data from NAND flash to the laptop, and erasing NAND flash. We opted to separate firmware in several smaller and compact applications due to easier debugging of the code and shortened time to obtain working applications and start experiments. It can be easily seen that our focus was not on optimizing firmware and building a universal application that will be able to manage everything from testing the transceiver to experimental deployment, but to develop a test environment for LoRa physical layer as fast as possible.

Furthermore, due to same reasons, we did not exploit the different sleep modes of the microcontroller. Namely, we used the transceivers in the experiments which lasted up to 8 hours; with sending rate used in the tests, we calculated that using the batteries of 1300 mAh, the transceivers could operate for, at least, 24 hours on a single battery charge, therefore we identified no reason to optimize power consumption for the experiments.

As far as drivers used in the application are concerned, we took advantage of different libraries provided by the manufacturer of the microcontroller. Those drivers encompass the driver for NAND flash, SPI bus, and UART; they did not require any modifications and we were able to use them in a straight-forward manner.

On the other hand, the LoRa modem manufacturer provided drivers for the SX1276, as well as the development kits for testing purposes. However, the drivers were written to be executed on a different microcontroller and we could not exploit the drivers without modifications. We opted to port manufacturer's drivers to the microcontroller we used in our implementation. Also, we inspected the application the manufacturer provided for testers and developers and found out that they used a polling mechanism to receive packets. After extensive testing of the application, we found out that sporadic packet loss occurs. We attributed this to the usage of a polling mechanism for packet reception, so we also modified the manufacturer's application to exploit interrupts for packet reception. This improved packet reception rate and we were able to receive packets without loss.

In Fig. 3.16 the firmware execution flow diagram is given. As can be seen, at the beginning of the code execution, the transmitter or receiver is enabled. After that, execution proceeds to initialization of microcontroller peripherals, as well as the NAND flash. Peripherals that are initialized in this stage are: SPI controller, USART, timers, and I/O. In both transceiver's operation modes, the next step is the initialization of the LoRa modem in corresponding operation mode. In this step, the following operations are carried out:

- putting the modem in standby mode
- setting the desired carrier frequency, spreading factor, bandwidth and coding rate
- enabling the CRC check, and disabling the use of implicit packet header
- setting the payload length
- setting the LNA gain and output power

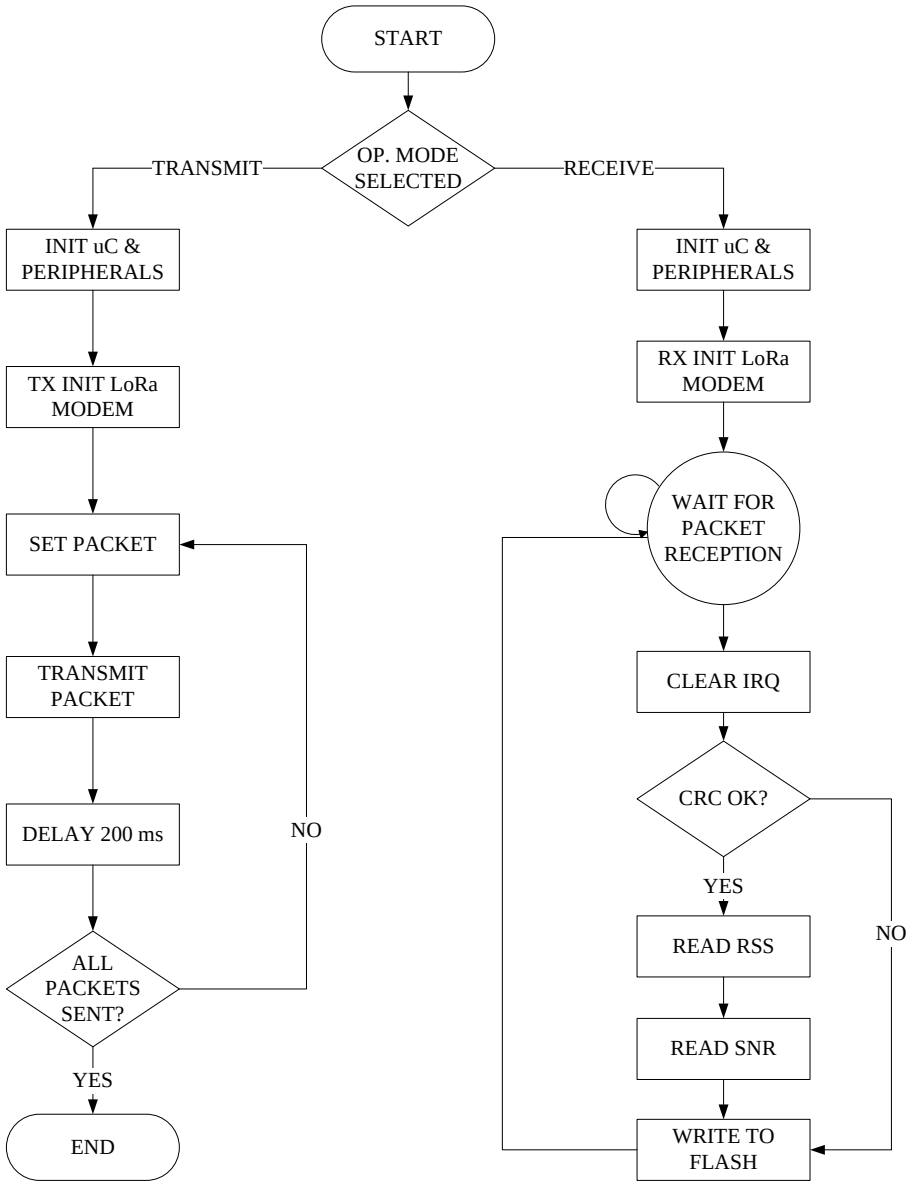

Figure 3.16: Flow diagram of the firmware executed on the transceiver during experiments.

After the LoRa modem initialization is finished, the transceiver goes into receive or transmit mode and is able to start transmission. In transmit mode, packet payload is populated with proper packet identification number (ID) and dummy bytes, and is transmitted afterward. There is also an inter-packet sending delay which is used to allow the receive side to perform necessary operations upon the reception of the packet. When a predefined number of packets is sent, code execution terminates.

In the receive operation mode, when all the initializations are finished, the

transceiver goes into the continuous receive mode, waiting for the interrupt signal from the LoRa modem which signalizes a packet reception. Firstly, the interrupt request is cleared and the CRC of the received packet is checked. If the CRC is bad, the time stamp and a bad CRC flag are written in the NAND flash. On the other hand, if the CRC is good, the RSS and SNR of the received packet are read from the corresponding register and logged into NAND flash along with the time stamp and packet ID. After this step, the transceiver again goes to receive mode, waiting for the next packet to be received.

Chapter 4

Laboratory Experiment Results and Discussion

In this chapter, we present the laboratory experiments we performed to investigate the characteristics of the new LoRa transceiver and methods to determine the RSS indicator correction factors and SNR measurement chain saturation region. Since the laboratory environment offers controllable experimental conditions, we also used it to compare the performance of different LoRa transceivers, which is one of the objectives of our work. It is important to note that experiments to be carried out in the laboratory, in the case of wireless transceivers, imply use of cables and attenuators for the connection of transceivers instead of antennas. In that way, the effects of multipath propagation are minimized and identical propagation conditions are provided for performance comparison. This is especially important for the transceiver's sensitivity measurements.

In industry, the laboratory verification tests are used to verify the transceiver's compliance with different standards based on the transceiver application. In our experimental work, we did not perform such tests because the transceivers were used only in experimental measurement campaigns in a limited amount of time.

To assess the performance of the new LoRa transceiver we carried out several different tests. The first one was the measurement of output power. This test is important because it can very quickly reveal design issues in the RF front-end of the transceiver. Namely, if the output power is not as expected, i.e. the one that was set in firmware by writing the desired value in the corresponding register of the LoRa modem, it can indicate several possible problems, such as wrong microstrip

geometry, high impedance matching network insertion loss, or both. An incorrect microstrip geometry will also degrade the sensitivity of the transceiver because the received signal will be additionally attenuated and possibly the LoRa modem will not be able to detect the signal and decode the received packet. On the other hand, since the output impedances of transmitting and receive pins of LoRa modem IC are different, further testing would be needed to measure the impedance matching network insertion loss in the receive path of the transceiver.

The next parameter that should be measured is the sensitivity of the transceiver which may indicate how good is the overall hardware design of the transceiver due to already mentioned reasons in the previous chapter. This measurement actually shows what is the minimum signal level at the input of the transceiver which can provide decoding of the received packet, recording the packet loss of 1 %. The experiment requires a special setup which would exclude the external factors which could degrade the transceiver's performance such as external interference and minimize the multipath propagation effects between transmitter and receiver. In addition, a sufficient number of packets must be sent in order to provide valid and reliable experimental results.

The power consumption requirements for systems deployed in IoT may be very strict if the devices are designed to be only battery-operated. It is required that a standalone device can operate for several years without any intervention. When a device is deployed outdoor, the autonomy can be relatively easily achieved provided that the device is not deployed in a harsh environment. The extended autonomy, in this case, can be accomplished using solar panels utilized to charge the device's battery. On the other hand, when a device is deployed indoor and external power supply is not available, the power consumption has to be controlled and managed by both the hardware and firmware design. We carried out power consumption measurements to determine the worst-case scenario battery life and to estimate how long the new LoRa transceiver could operate on a single battery charge in a specific use case scenario.

Finally, the emergence of IoT concept and wireless technologies such as Bluetooth, Zigbee, sub-gigahertz transmission technologies, etc. established the RSS as

a significant parameter to assess a link's behavior. Usually, RSS is available in the corresponding register as a number; however, there is typically no additional explanation what is the meaning of those values and how they are correlated with actually received signal strength present at the transceiver's input. The situation is similar for the SNR since it is unknown how the measured value is obtained, or when the measurement chain goes to saturation, and what is the range of linear operation of the measurement chain. To overcome this gap and to provide a reliable experimental data, we performed the experiments in which we determined the correction factors for the RSS values captured by LoRa modem IC and investigated the linear region of operation for both RSS indicator and SNR measurement chain.

4.1 Transceiver RF Output Power Measurements

We performed the RF output power measurements using spectrum analyzer Keysight N9915A FieldFox. The spectrum analyzer was used due to several reasons. Namely, besides the output power, we wanted also to capture the spectrum of the transmitted signal for three different LoRa bandwidths: 125 kHz, 250 kHz, and 500 kHz using the fixed spreading factor, SF = 10 and coding rate CR = 4/6.

The measurement setup consisted of one experimental Own Developed Transceiver (OdT) that was connected to the spectrum analyzer using very short and low-loss coaxial cable. To avoid additional losses in connector transitions, the coaxial cable was equipped with adequate connectors on both sides: a male MMCX connector on the side of the transceiver and an N-type connector on the side of the spectrum analyzer. The spectrum analyzer was set in "max hold" capturing mode which provided the recording of the envelope of the transmitted signal spectrum; the output power was set to 14 dBm in firmware, while the carrier frequency was tuned to 868 MHz. The measurement results are given in Fig. 4.1.

As can be observed, the envelope of all three spectra is constant; the amplitude is almost 14 dBm which is in accordance with the output power set in firmware. This implies several very important characteristics of the transceiver hardware design.

As already noted, to maximize the power transfer from the RF IC transmitting pin to the transceiver antenna, it is necessary to properly design the following RF sub-blocks:

- PCB trace that connects the RF IC transmitting pin with antenna connector,
- Impedance matching network between the transceiver RF IC transmitting pin and the PCB trace,
- Impedance matching network between the PCB trace and the antenna.

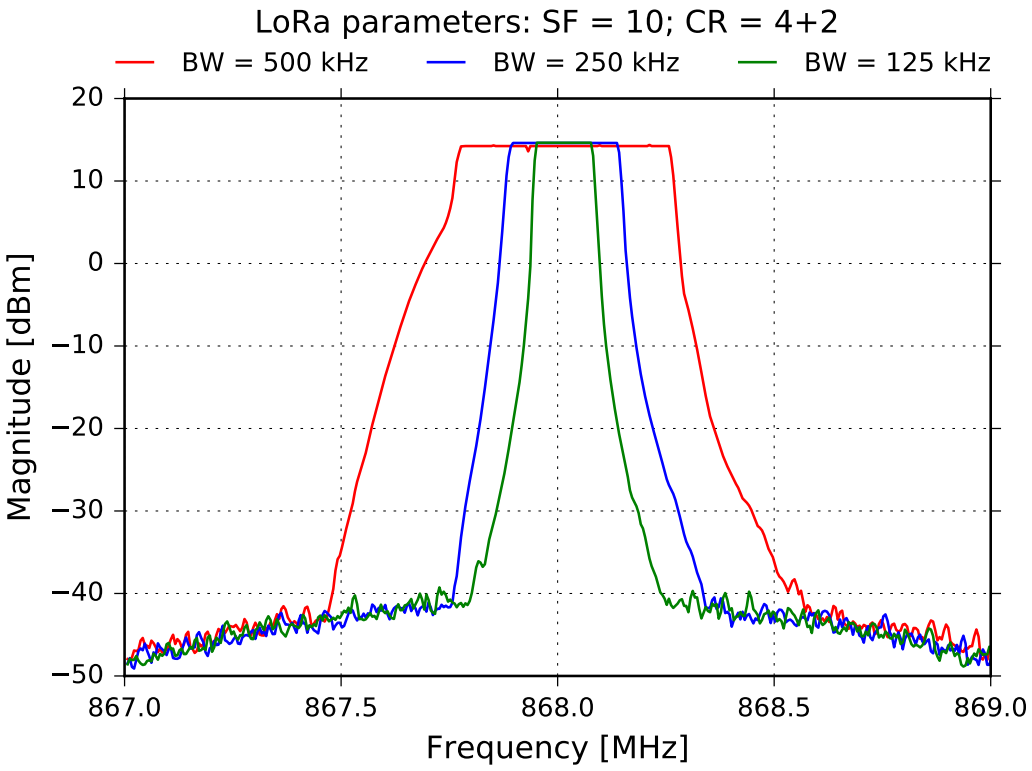

Figure 4.1: OdT RF output power at 868 MHz for SF = 10 and CR = 4/6 within three different LoRa bandwidths: 125 kHz, 250 kHz, and 500 kHz. The measurements are carried out with Keysight N9915A FieldFox Microwave Analyzer and plotted with Python Matplotlib.

Only under these conditions is the maximum transfer of power to the antenna guaranteed. Since there is almost 14 dBm measured at the transceiver output, it can be confirmed that each sub-block of the transceiver is properly designed and routed. That practically means that the microstrip characteristic impedance is accurately

designed to be 50 Ω, and that it is properly routed including the compensation of the impedance discontinuities due to changing of routing direction. Furthermore, the impedance matching network between the RF IC transmitting pin and the PCB trace exhibits minimal losses at a frequency of interest, namely 868 MHz; also, it is properly placed and routed to minimize inevitable signal ringing when the RF signal is injected into the PCB. It is worth mentioning that the PCB is equipped with footprints for the Π impedance matching network for the antenna, but in this measurement, those footprints were left unpopulated, except the serially inserted footprint where a zero-ohm resistor was mounted.

Finally, Fig. 4.1 shows how the spectrum of a LoRa signal looks for different bandwidths and fixed spreading factor and coding rate, namely SF = 10 and CR = 4/6, respectively. Because of the "max hold" mode set on a spectrum analyzer and constant amplitude of the chirp signals used to modulate transmitted data, we observe the constant envelope. The bandwidths set in firmware can be easily identified on the plots.

4.2 Transceiver Sensitivity Measurements and Comparison with Commercial Transceivers

The sensitivity of the transceiver is, besides its output power, one of the most important characteristics of the transceiver. It depends on many factors, however, the sensitivity of the LoRa modem IC used to implement the transceiver and the PCB design methodology applied to develop the transceiver are the two most important. The assumption is, of course, that the schematic of the transceiver is appropriate in terms of the transceiver functionality.

The sensitivity of an RF IC is defined by its design and is specified by the manufacturer in the corresponding datasheet. That implies that it contributes to the transceiver sensitivity as a constant, whereas the PCB design dictates the overall sensitivity of the transceiver. To perform the measurement of the RF IC sensitivity, the manufacturer must design the test PCB, where the RF IC will be mounted together with other components necessary for its operation, and execute the mea-

surement. Therefore, it is very important for the manufacturer to develop a high-end test PCB which is able to provide very low noise floor for the RF IC since it will directly scale the overall sensitivity of the unit under test. This practically means that it is possible to achieve higher sensitivity than that specified by the manufacturer if improved PCB design methodology is applied to design the transceiver.

The sensitivity of the RF transceivers is usually defined as the received signal strength at which the packet loss is 1 %. The number of packets sent in such measurements must be adequate to accurately reflect the overall sensitivity. In engineering practice, that number is usually taken to be $\geq 10\,000$. In addition, all the propagation effects that occur in the field measurements (multipath propagation, fading, external interferences) must be excluded from the measurement setup in order to get reliable measurement results. Usually, such experiments are performed in the controlled propagation environment, connecting the transmitter and receiver pair using coaxial cable, while the variable attenuator is inserted serially to the propagation path.

The experimental setup we used to measure the new LoRa transceiver's sensitivity, as well as to compare it with two commercial transceivers is given in Fig 4.2. The same setup was used to determine the correction factors for RSS indicator of all transceivers in the test and to investigate the linearity of RSS indicators and SNR measurement chains.

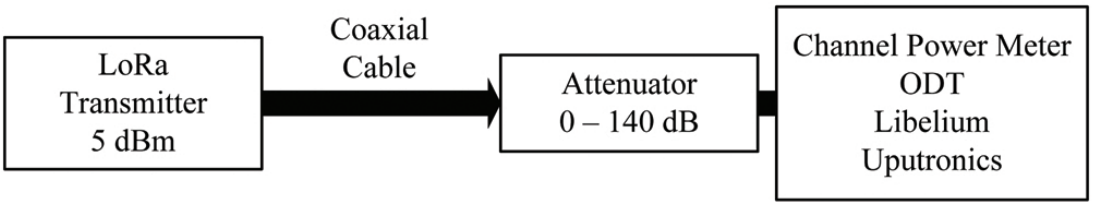

Figure 4.2: The experimental setup used to measure the OdT sensitivity and to compare its PRR with two commercial transceivers.

We measured sensitivity using the following LoRa parameters: SF = 10, BW = 125 kHz, and CR = 4/6 at 868 MHz. These are the same test conditions as provided in the SX1276 datasheet for the sensitivity measurement; we opted for these parame-

ters to be able to compare the results also with LoRa modem IC sensitivity specified by the manufacturer, indirectly comparing our PCB design to manufacturer's PCB design. Additionally, we set the maximum gain for the LNA, and enabled the boost option which provides the maximum gain, to provide exactly the same conditions specified by the manufacturer. Furthermore, the packet CRC was enabled and all the packets with a CRC error were discarded during the test. To enable reliable results, 20 000 packets were sent during each measurement. The output power was set to 5 dBm.

It is worth noting that the path loss tunning, although simple in theory, consumed significant time in practice because, to obtain attenuation granularity smaller than 1 dB provided by the variable attenuator, the coaxial cable needed to be shortened and the new connector mounted in each iteration. Using this procedure, we achieved a packet loss of 0.995 %.

During the measurement, time stamp, packet number, RSS, SNR, and PRR were logged. These are presented in Fig. 4.3. Dots represent current values, while solid lines present a moving average calculated on the 1-minute time window.

As can be seen in Fig. 4.3, RSS goes as low as −138 dBm, while SNR fluctuates between −11 and −14. The actual signal level at the transceiver input can be calculated as:

$$\mathrm{RSS} = P_{\mathrm{TX}} - L_{\mathrm{cable}} - L_{\mathrm{conn}} - L_{\mathrm{att}} \tag{4.1}$$

where,

- P_{TX} is transmit power,
- L_{cable} is loss in the coaxial cable,
- L_{conn} is aggregate loss in all connectors and transitions on the connection path between transmitter and receiver,
- L_{att} is the attenuation set on the variable attenuator.

When the concrete values are substituted in Eq. 4.1, we get:

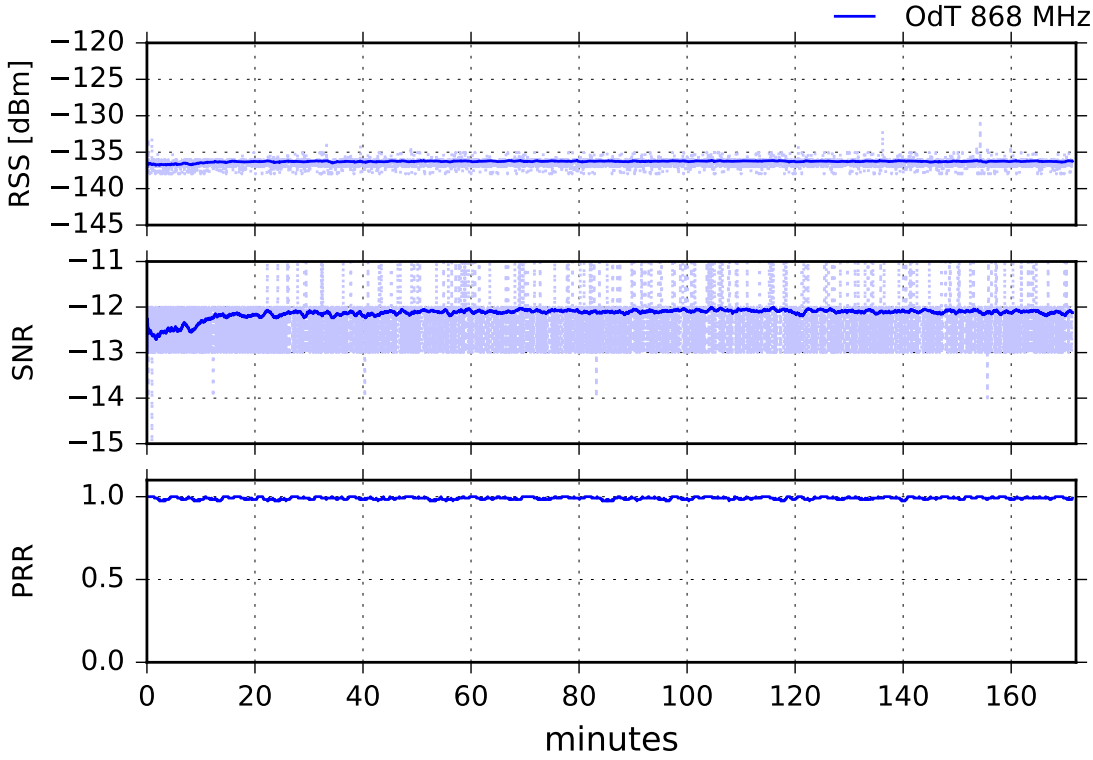

Figure 4.3: RSS, SNR, and PRR recorded during OdT sensitivity measurement.

$$\text{RSS} = 5\,\text{dBm} - 8\,\text{dB} - 1\,\text{dB} - 133\,\text{dB} = -137\,\text{dBm} \tag{4.2}$$

This is the actual received signal level at the transmitter input. We observe that the transceiver also recorded values which rolling mean is approximately $-137\,\text{dBm}$ during the measurement interval, while single values fluctuate between $-135\,\text{dBm}$ and -138 dBm. The SNR moving average values are also constant and are approximately -12. It can be also observed that there are excursions of RSS and SNR at the beginning of the experiment. However, this is not expected since the transmitter and receiver were connected with a cable, which implies no multipath and fading effects were present in the transmission path. Nonetheless, this can be explained by the fact that the receiver was not shielded, which implies that different interference signals could be coupled to the transceiver and cause fluctuations in RSS and consequently in SNR.

If the sensitivity of the OdT transceiver is compared to the sensitivity of the RF IC used to implement the OdT transceiver, namely Semtech SX1276, it can be

observed that OdT sensitivity is better for 5 dB than the sensitivity of the RF IC. This counterintuitive result has been already explained, and it clearly shows the hardware design advantages of the new LoRa transceiver.

On the other hand, the measured value can be compared with the theoretical value of the receiver's absolute noise floor. The theoretical absolute noise floor can be calculated as follows:

$$\text{NoiseFloor [dBm]} = 10 \times log_{10}(k \times T) + 10 \times log_{10}(\text{BW}) + \text{NF} \tag{4.3}$$

where:

- k is Boltzmann's constant, $k = 1.38 \times 10^{-23}$ joules per kelvin,
- T is the temperature of the receiver system in kelvins,
- BW is detection bandwidth in hertz
- NF is receiver noise figure in dB

For the bandwidth of BW = 125 kHz, the theoretical absolute noise floor at room temperature is -123 dBm. This is the theoretical value for transmission systems with a 0 dB noise factor. The receiver sensitivity is given by the sum of the noise floor and the SNR. As already stated, LoRa modulation uses chirp spread spectrum modulation, which provides the capability to detect signals below the noise power, that is with negative values of SNR, as shown in our measurements. It can be also observed that LoRa system based on newly developed transceiver offers better link margin for even 14 dB. That implies better range and better penetration into buildings and basements in the urban deployment scenarios. This is very important for the practical LoRaWAN implementations and deployments since better coverage can be achieved with fewer gateways, which are the most expensive elements of such networks.

We also carried out comparison tests with two widely adopted commercial transceivers in terms of sensitivity. The tests were carried out under equal and controlled conditions provided for all transceivers under test. As stated earlier, the sensitivity

of the overall transceiver module depends on two distinct factors: (a) the sensitivity of LoRa modem embedded therein, and (b) the hardware design of the whole transceiver. In a controlled laboratory setting, it is safe to assume that these factors contribute with two distinct terms that combine additively to the overall transceiver sensitivity. The first term (a), namely the modem sensitivity, is specified by the manufacturer and depends on the selected LoRa parameters. The second term (b) is independent of the LoRa parameters. Therefore, to compare different hardware design sensitivities (b), it is sufficient to compare three different transceivers for a single common set of parameter values. Since varying the parameter configuration chosen for the laboratory experiment would merely add a common offset value to all tests, we opted to use only one set of the LoRa parameters for the purpose of the comparison, and we chose the same as in the case for OdT: SF = 10, BW = 125 kHz, CR = 4/6.

As far as the commercial transceivers in the test are concerned, we used two: Libelium (LiT) and Uputronics (UpT). The Libelium was primarily chosen because it is one of the most expensive LoRa transceivers on the market, and produced by the biggest LoRa equipment manufacturer. The transceiver uses the Semtech SX1272 LoRa modem and supports only one frequency band, $860-1020$ MHz, offering output power up to 20 dBm. It can use spreading factors in the range of SF $\in [6, 12]$, within three different LoRa bandwidths: $125, 250$, and 500 kHz. This transceiver needs a host system to operate and during the experiments, it was mounted on a Seeeduino Stalker v2.3 carrier board.

There are several advantages of using such a transceiver in the experiments. Firstly, developing a firmware for an application is a straight-forward task since there are already tested LoRa libraries available which contain all the functions to manage the operation of SX1272. The host board enables simple connection of external sensors via its port expanders and data logging is also simplified since there is a Secure Digital (SD) slot mounted on the PCB.

However, there are also several drawbacks when such transceiver is used. Because it is designed to be used in a wide spectrum of applications as general-purpose LoRa transceiver, it is not optimized in terms of noise figure and consequently the

sensitivity. This implies decreased range and lower penetration in buildings when deployed in urban scenarios. In addition, the power consumption of this transceiver is increased, because of general-purpose peripherals on the host board which cannot be disconnected using e.g. load switches. This complicates power management strategy when it comes to the field deployment in long-run experiments.

The second commercial transceiver deployed in the comparison experiments was Uputronics (UpT). This transceiver is chosen because it is a low-cost and widespread solution, widely adopted in the industry. It exploits the RFM95 LoRa module from HopeRF, which has identical characteristics to those of the SX1276, as determined by comparing the corresponding datasheets. As well as the Libelium transceiver, this also requires a host system for its operation and was, therefore, mounted as a shield on a Raspberry Pi3. The benefits and downsides of using this transceiver in the experiments are similar to those for LiT, the only major difference is the cost of the transceiver.

It is important to emphasize that to adjust the packet loss to be the same on all three transceivers, i.e. 1 % in order to obtain transceivers' sensitivities, it is necessary to tune a different attenuation on variable attenuator for each transceiver. Based on the previous sensitivity measurement for OdT, we wanted to avoid this tedious task and provide the PRR comparison under the same experimental conditions, rather than to measure the sensitivity of all three transceivers. Therefore, we set the attenuation in such way that OdT started to lose packets sporadically, and then applied the same attenuation for remaining two transceivers under test.

The superior performance of OdT is evident from the laboratory results shown in Fig. 4.4. Namely, the packet losses were 77.38 %, 12.99 %, and 3.01 % respectively for LiT, UpT and OdT. The RSS plot in Fig. 4.3 reveals that the higher reception rate of OdT is a result of the better sensitivity of the hardware design as the LoRa modem in the OdT could decode packets with RSS as low as -139 dBm, while the second best device, namely UpT, would not be able to decode packets with RSS below -132 dBm. Note however that UpT had a packet loss rate four times higher than OdT (12.99 % vs. 3.01 %), meaning a significantly higher sensitivity gain of the OdT. The third tested device, LiT, showed considerably worse performance and

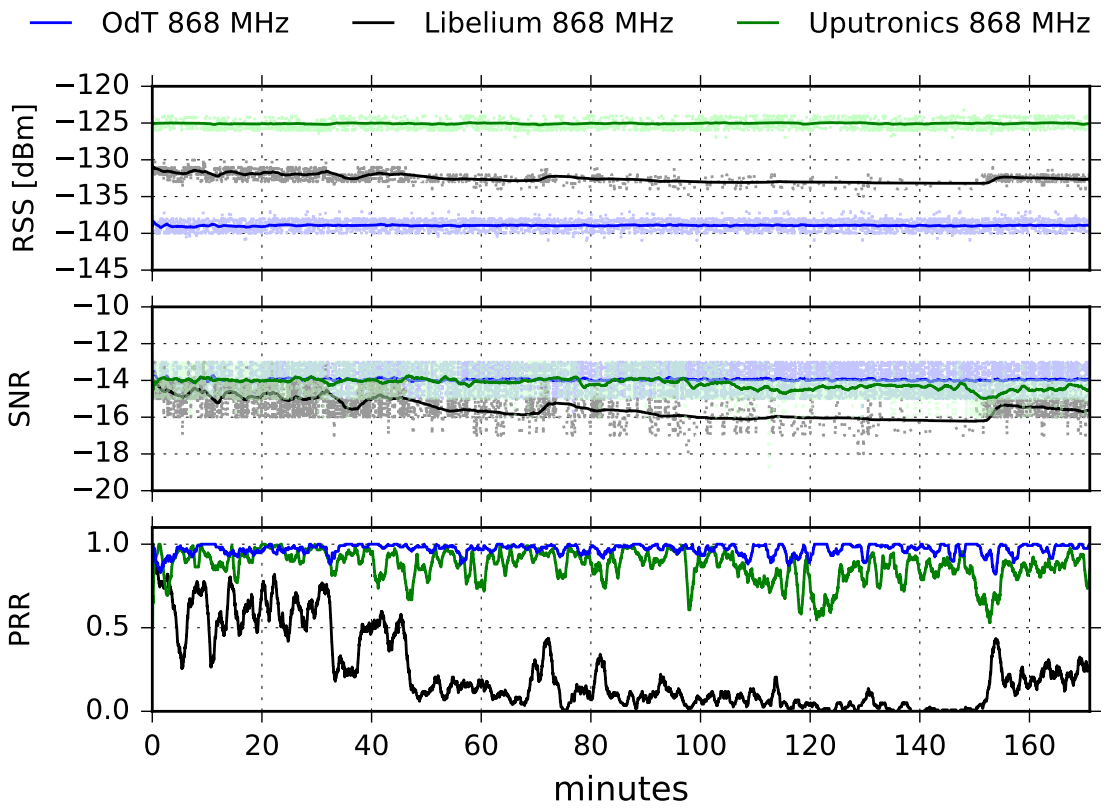

Figure 4.4: RSS, SNR and PRR in the laboratory comparison test for OdT, LiT and UpT at 868 MHz. LoRa test parameters: BW = 125 kHz, SF = 10.

sensitivity, with minimum RSS of −125 dB and very high packet loss.

Since the packet losses are not equal, sensitivities of the transceivers cannot be directly compared. Using a conservative comparison approach, it can be concluded that the OdT has at least 15 dB better sensitivity than UpT, and 25 dB better than LiT.

4.3 Power Consumption Measurements

Power consumption is one of the most important aspects of IoT systems. It is required that battery-operated devices are capable of standalone operation without any intervention for years. Different techniques must be combined to successfully cope with such stringent requirements. On the other hand, the power consumption measurement of such systems poses a challenge since it can vary in range from nano-to-mili amperes. Besides the static and dynamic power consumption of the

components used to implement device used in IoT, e.g. LoRa transceiver, a very important aspect is a design and implementation of the optimal strategy for managing different operating modes of the transceiver.

As pointed out in the previous chapter, OdT provides the possibility for the developer to implement very low power consumption since it integrates components, i.e. integrated circuits which have extremely low power consumption. However, in our experiments, we did not design any operation mode managing algorithm in firmware to minimize the power consumption since we did not need it in our experimental scenarios.

In this section we present the power consumption measurements of OdT performed with a DC power analyzer Keysight N6715C. This DC power analyzer is used to provide the power supply for the transceiver and, simultaneously, is used to log the current consumption of the transceiver versus time. The power supply voltage was set to $V = 3.9\,\mathrm{V}$ to emulate 50 % discharged lithium - polymer battery since this type of battery is usually used in such systems. The sampling interval of DC power analyzer was set to $T_{\mathrm{sample}} = 0.04\,\mathrm{ms}$. In this way, we were able to measure accurately current consumption profiles of OdT transceiver for different LoRa parameters since the minimum packet duration was approximately 56 ms.

The measurements were performed for three different spreading factors, namely $\mathrm{SF} \in \{7, 10, 12\}$, while bandwidth and coding rate were fixed to $\mathrm{BW} = 125\,\mathrm{kHz}$ and $\mathrm{CR} = 4/6$. The operating frequency was set to 868 MHz, and the output power was set to the 14 dBm which is the maximum output power on the high-frequency port in this implementation.

The format of the packets sent in experiments is depicted in Fig. 4.5. The preamble is used to synchronize the receiver with the incoming data packet. Besides the preamble, there is also an explicit header incorporated in the packet. The header contains additional information about the packet structure, namely about the payload length in bytes, the coding rate, and the presence of a 16-bit CRC for the payload. The header has its own CRC, but there is no information provided about its length, as well as the length of the whole header in the corresponding datasheet.

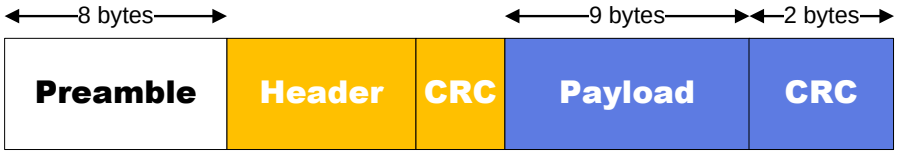

Figure 4.5: Format of the message sent in the experiments.

In each measurement 20 000 packets were sent. The inter-packet delay was set to 200 ms. On the receiving side, for each correctly decoded packet, the receiver logged the time-stamp, the packet identifier, RSS and SNR values as reported in the corresponding modem registers. The measurement results are given in Fig. 4.6.

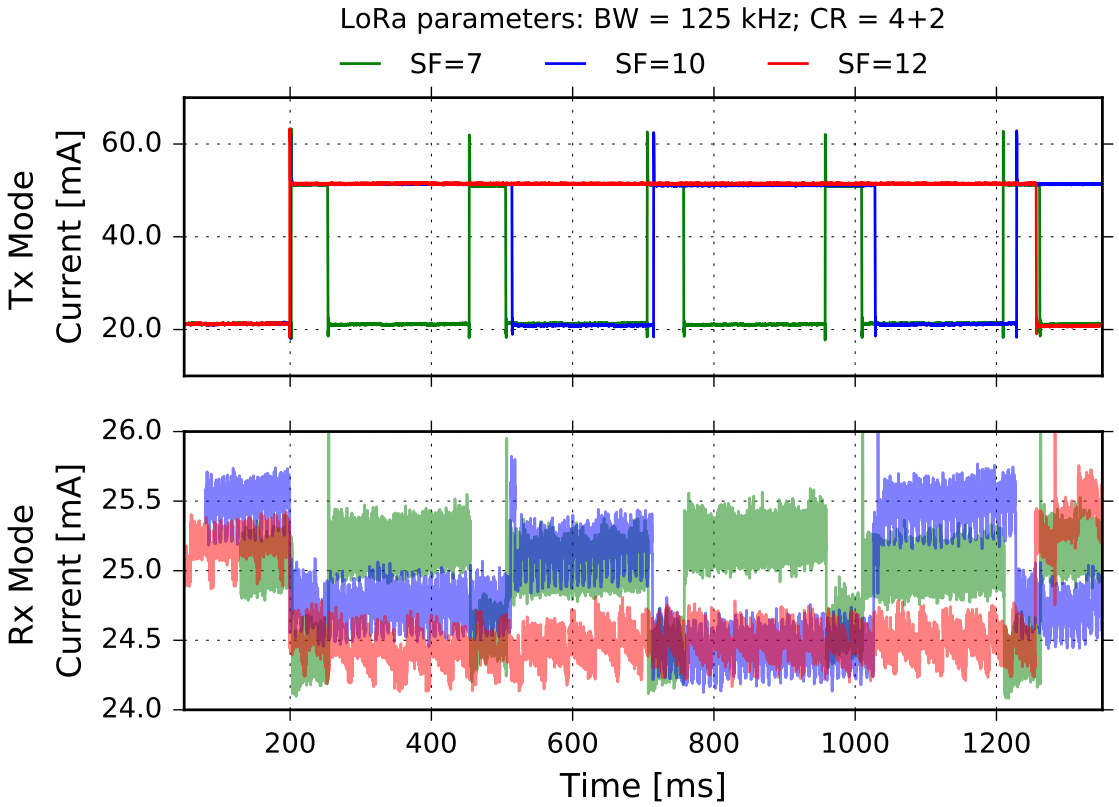

Figure 4.6: OdT current consumption for three different LoRa parameter sets: SF $\in \{7, 10, 12\}$, BW = 125 kHz, CR = 4/6 measured with Keysight N6715C and plotted with Python Matplotlib.

From Fig. 4.6 we observe that in transmit mode, the peak values are the same for all three sets of parameters. For a very short time, the peaks go to approximately 62 mA, and after the abrupt decrease, the current consumption goes to a constant value of 50 mA. It can also be noticed that, while the transceiver is in idle

mode, the current consumption is 21 mA, which is very high for the battery-operated transceivers. However, as already stated, there is no algorithm implemented in the firmware that would manage the power consumption of the transceiver by putting it into different sleep modes when the transceiver is idle.

While receiving packets, the transceiver goes through different operating modes which is reflected in the current consumption fluctuations of approximately 1 mA, in the range $I_{\mathrm{RX}} = [24.5, 25.5]$ mA. Here has to be noted that higher consumption after receiving the packet is due to writing data in the NAND flash memory.

The power consumption measurements reveal also the packet airtime for the different LoRa parameters since it can be clearly distinguished when the transceiver transmits or receives packets from the plots in Fig 4.6. To be able to check whether the packet airtime is in accordance with theoretical packet airtime, we firstly present the calculus of LoRa packet airtime, based on the available documentation provided by Semtech. The LoRa packet airtime is defined as:

$$T_{\mathrm{packet}} = T_{\mathrm{preamble}} + T_{\mathrm{payload}} \tag{4.4}$$

Duration of the payload is defined as:

$$T_{\mathrm{payload}} = n_{\mathrm{payload}} \times T_{\mathrm{s}} \tag{4.5}$$

where T_{s} is the symbol duration:

$$T_{\mathrm{s}} = \frac{1}{R_{\mathrm{s}}} \tag{4.6}$$

and R_{s} is the symbol rate. The symbol rate is defined as the rate at which the spread information is sent:

$$R_{\mathrm{s}} = \frac{\mathrm{BW}}{2^{\mathrm{SF}}} \tag{4.7}$$

Now, the duration of the preamble can be calculated as:

$$T_{\mathrm{preamble}} = (n_{\mathrm{preamble}} + 4.25) \times T_{\mathrm{s}} \tag{4.8}$$

which, after the substitution for R_s, becomes:

$$T_{\text{preamble}} = \frac{2^{\text{SF}} \times (n_{\text{preamble}} + 4.25)}{\text{BW}} \tag{4.9}$$

The number of bytes in the preamble is set by the user and can be read in the corresponding registers: *RegPreambleMsb* and *RegPreambleLsb*. The number of symbols in the payload can be calculated as follows:

$$n_{\text{payload}} = 8 + \max\left(\text{ceil}\left[\frac{(8\text{PL} - 4\text{SF} + 28 + 16\text{CRC} - 20\text{IH})}{4(\text{SF} - 2\text{DE})}\right](\text{CR} + 4), 0\right) \tag{4.10}$$

where:

- PL is the number of payload bytes; it can take values in range $[1 - 255]$,
- SF is the spreading factor,
- IH is the implicit header; IH $= 0$ when the explicit header is enabled, IH $= 1$ when there is no header,
- DE is the flag for *Low Data Rate Optimizer*; DE $= 1$ when optimizer is enabled, DE $= 0$ otherwise,
- CR is the coding rate (1 corresponds to 4/5, 4 to 4/8).

Finally, the packet airtime can be calculated according to the following formula:

$$\begin{aligned} T_{\text{packet}} =& \frac{2^{\text{SF}} \times (n_{\text{preamble}} + 4.25)}{\text{BW}} + 8 \times \frac{2^{\text{SF}}}{\text{BW}} + \\ &+ \max\left(\text{ceil}\left[\frac{(8\text{PL} - 4\text{SF} + 28 + 16\text{CRC} - 20\text{IH}) \times 2^{\text{SF}}}{4 \times \text{BW} \times (\text{SF} - 2\text{DE})}\right](\text{CR} + 4), 0\right) \end{aligned} \tag{4.11}$$

When we substitute the LoRa parameters used in the experiments in Eq. 4.11, we obtain: 51.46 ms, 313.14 ms, and 1056.77 ms, for SF $= 7$, SF $= 10$, and SF $= 12$,

respectively, which is in accordance with experimental results, see Fig. 4.6.

It is interesting to estimate the autonomy of the new LoRa transceiver, equipped with a battery that can provide e.g. 5 Ah, for the following LoRa parameters: SF = 10, BW = 125 , and CR = 4/6. The estimation assumes the maximum output power, no power management algorithm implemented, and that the battery provides a constant voltage of 3.9V constantly, which can differ from real exploitation conditions.

Energy consumed in one cycle (transmit plus idle time) can be calculated as follows:

$$E = \int_0^{T_{tx}} v(t)\, i(t)\, dt + \int_{T_{tx}}^{T_{idle}} v(t)\, i(t)\, dt \tag{4.12}$$

Reading the values from Fig. 4.6, it can be calculated that energy consumed in one cycle is $E = 22.28\,\mu\text{W h}$. That implies that electric charge per one cycle yields $Q = 5.71\,\mu\text{A h}$. This practically means that transceiver can achieve 875 657 cycles. Translated into the time domain, it can be calculated that transceiver can continuously send packets with an inter-packet delay of only 200 ms for $T = 125.02$ hours. However, this extremely high sending rate cannot be exploited in LPWANs due to the violation of European spectrum duty cycle regulation [87]. On the other hand, the usual use case scenario would be to take and send measurements only several times per day.

If we assume that the transceiver has to send three packets per day and that it is in deep sleep mode of operation between sending, we can recalculate the operating time without the charging the battery. We can assume that the power consumption of the transceiver, while in sleep mode, is approximately $\text{I} = 52\,\mu\text{A h}$ at 3.9 V, based on the datasheets of the corresponding components. Since the time duration of the 3 packets in this operation mode is $T_{\text{airTime}} = 939\,\text{ms}$, using the Eq. 4.12, we can calculate the energy consumption for this particular case per day: $E = 4.9\,\text{mWh}$. That yields the estimated autonomy of $T_{\text{autonomy}} = 10.86$ years on a 5 Ah battery. This shows that the transceiver can fit the LPWAN deployment scenarios in remote locations since in such scenarios there is usually no need for frequent data sending.

4.4 RSSI Correction Factors and SNR Measurement Chain Linearity

LoRa modem ICs are equipped with RSS Indicators (RSSI) and SNR measurement capabilities. Measured values are stored in the corresponding registers and can be read via the SPI bus by the host processor. For an accurate interpretation of the experimental results, it is necessary to assess RSSI accuracy and determine the saturation threshold for the SNR measurement chain. However, until now, there has been no work which fully addresses this issue. For example, Gaelens et al. [33] found the SNR measurement chain saturation threshold for the transceiver used in their experiments, but without finding RSSI correction factors.

RSSI correction factors imply correlation of actual received power at the LoRa modem IC's RF pin and the value available in the corresponding transceiver's register. The measurement offset may be a consequence of the transceiver's RF front attenuation and/or the inherent IC production tolerances.

To investigate SNR measurement chain linearity and find RSSI correction factors, we arranged the setup shown in Fig. 4.2. An OdT was used as a transmitter set to 5 dBm of output power. The output was connected through a coaxial cable and a variable attenuator to the channel power meter (Keysight FieldFox N9915A handheld microwave analyzer). We performed channel power measurements on LoRa signals at different attenuations and for both frequencies of interests. The results are presented in Figs. 4.7 and 4.8 in magenta color for both 868 MHz and 434 MHz, respectively. In that way, we obtained reference RSS values for both frequencies.

We then repeated the same measurements replacing the channel power meter with each of the LoRa transceivers used in the field experiments, recording RSS and SNR for both frequencies of interest. The results are presented in the same plots.

Applying a least squares error polynomial fit through the measured points we obtained the following equations:

$$\text{Reference}\,[434\,\text{MHz}] = -0.9948 \times \text{att} + 4.556 \tag{4.13}$$

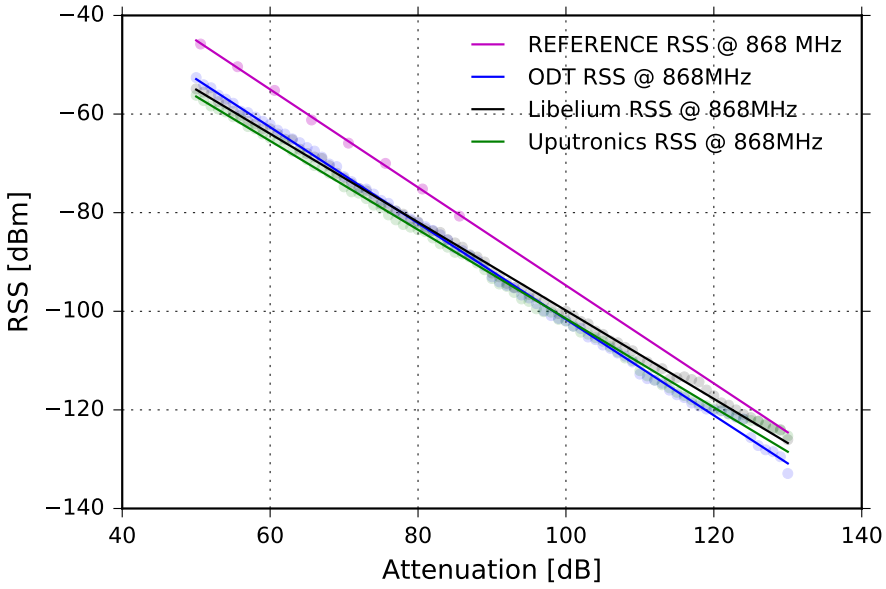

Figure 4.7: Received signal strength vs. channel attenuation for reference RSS and OdT (868 MHz), Libelium (868 MHz), and Uputronics (868 MHz).

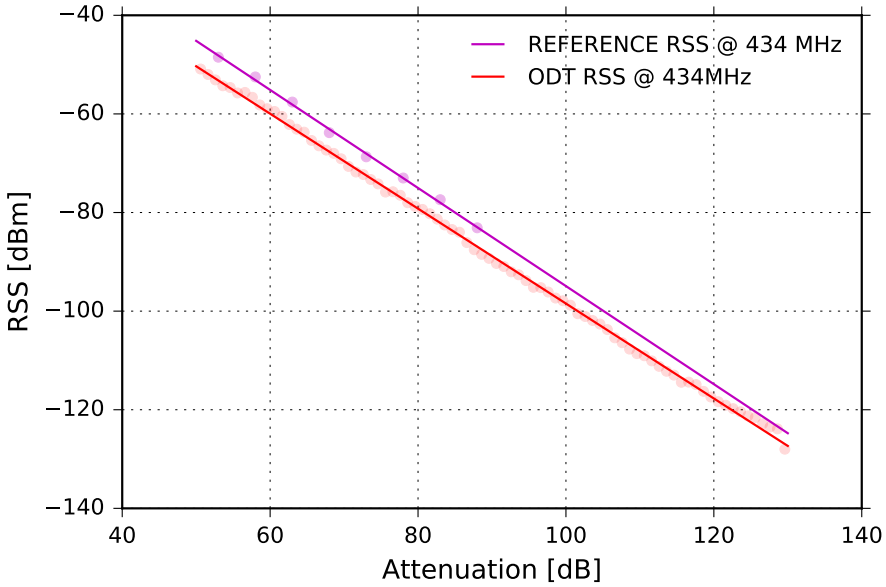

Figure 4.8: Received signal strength vs. channel attenuation for reference RSS and OdT (434 MHz).

$$\text{Reference}\,[868\,\text{MHz}] = -0.9938 \times \text{att} + 4.628 \tag{4.14}$$

$$\text{OdT}\,[434\,\text{MHz}] = -0.9626 \times \text{att} - 2.205 \tag{4.15}$$

$$\text{OdT}\,[868\,\text{MHz}] = -0.9743 \times \text{att} - 4.194 \tag{4.16}$$

$$\text{Uputronics}\,[868\,\text{MHz}] = -0.9007 \times \text{att} - 11.41 \tag{4.17}$$

$$\text{Libelium}\,[868\,\text{MHz}] = -0.8962 \times \text{att} - 10.22 \tag{4.18}$$

The obtained equations were used to correct the values reported by corresponding transceivers. As can be seen in Figs. 4.7 and 4.8, RSS reported by the transceivers is linear in a wide range, although there is a constant offset between the power measured with the power meter and the corresponding values read in the transceivers' registers. The difference is about 6.7 dB at 434 MHz and about 8.8 dB at 868 MHz for OdT. The commercial devices exhibit different offsets due to different RF front-end attenuations: 16 dB for the Uputronics and 14.8 dB for the Libelium. It can be inferred that the devices are self-coherent but the absolute values reported by the transceivers significantly differ from absolute values measured with the power meter.

The linearity of the SNR reported by the transceivers is also experimentally verified for all transceivers used in the experiments. As can be noticed in Fig. 4.9, SNR measurement chain enters saturation when the RSS approaches −100 dBm for all three transceivers.

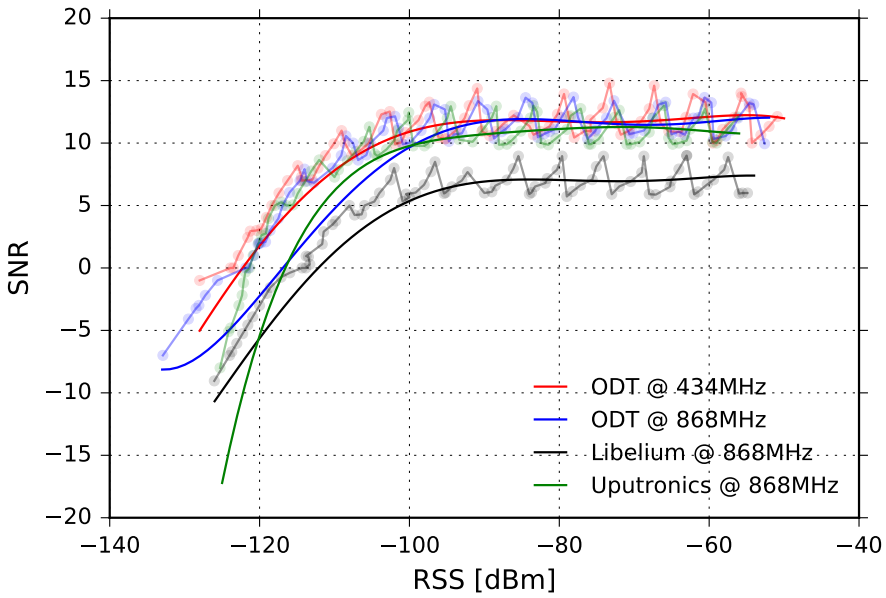

Figure 4.9: Signal-to-Noise ratio vs. Received Signal Strength for OdT (434 MHz), OdT (868 MHz), Libelium (868 MHz), and Uputronics (868 MHz).

Chapter 5

Field Experiment Results and Discussion

The field experiments aim to investigate the OdT performances under real operating conditions, as well as to compare them with characteristics of the commercial transceivers under identical experimental conditions. Besides that, the purpose of these experiments is also to provide deeper insight into LoRa technology in several deployment scenarios, namely in very long ($> 100\,\text{km}$) and ultra-long links ($> 300\,\text{km}$) over land, as well as in long links ($> 20\,\text{km}$) over seawater. It is worth remembering that, despite the fact that LoRa has been developed to be used in such scenarios (long range), the scientific community still lacks experimental studies and conclusions that can provide a deeper insight into technology advantages and limitations in such deployment scenarios.

5.1 Experimental Transceivers and Antennas

To provide more reliable experimental data and therefore conclusions drawn from the experiments, various transceivers were deployed in different testbeds, exploiting a variety of LoRa parameters in two different frequency bands. Besides the Own Developed Transceiver (OdT), two additional commercial transceivers were used in the experiments: Libelium (LiT) and Uputronics (UpT). In order to make the experimental conclusions usable in real applications, we deployed low-cost Commercial Off-the-Shelf (COTS) rubber duck antennas for both frequency bands of interests, namely 868 MHz and 434 MHz.

Low-cost COTS antennas usually do not have good characteristics in terms of

specified impedance and radiation pattern due to huge manufacturing variations and tolerances. To characterize the antennas used in the experiments, we measured their resonant frequency (S11 parameter), and Standing-Wave Ratio (SWR). Since the measured parameters were similar for all antennas used within the same frequency band, we provided measurement results from one 868 MHz and one 434 MHz antenna.

In Fig. 5.1 S11 parameter and SWR of the COTS antenna used in 868 MHz experiments are given. The measurements are carried out in the field, using Keysight N9915A FieldFox Microwave Analyzer.

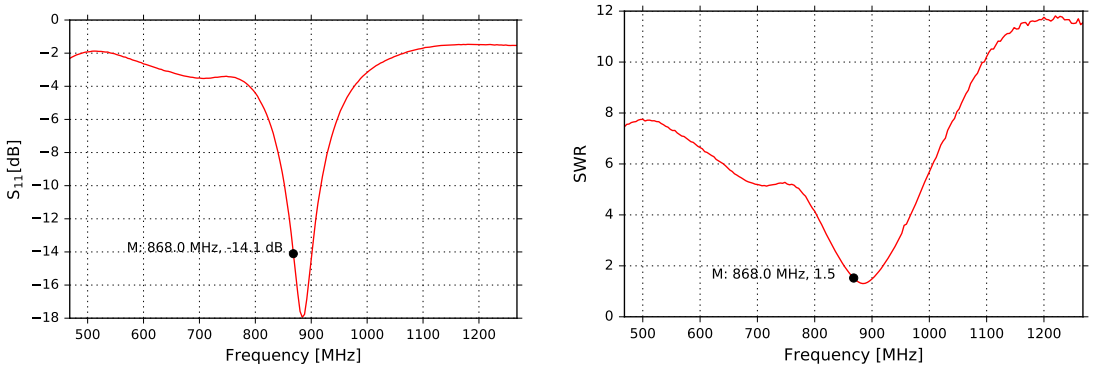

(a) S11 parameter for 868 MHz COTS antenna

(b) SWR for 868 MHz COTS antenna

Figure 5.1: S11 and SWR for 868 MHz COTS antenna measured with Keysight N9915A FieldFox Microwave Analyzer and plotted with Python Matplotlib.

We observe that COTS antenna used in 868 MHz band is suitable to be used in the experiments since S11 parameter (Return Loss, RL) is smaller than −10 dB. This claim is based on the common engineering practice, which suggests a maximum acceptable return loss of −10 dB. That implies that 90 % of the transmitted power is delivered to the antenna, while 10 % is returned to the transmitter. Combined with SWR measurement, SWR = 1.5, it can be concluded that the impedance of the antenna is acceptable to be used on the frequency of interest, therefore we did not perform impedance matching by inserting additional passive network on PCB between the harmonic filter and antenna connector.

In the case of 434 MHz COTS antenna, the situation is somewhat different. Measurements of S11 and SWR parameters in the field are given in Fig. 5.2. As can

be observed, the parameters of the COTS antenna for 434 MHz are on the boundary to be acknowledged as suitable for the experiments: the return loss is, RL = −9.9 dB, while SWR = 2. However, we did not perform any impedance matching because we wanted to have identical conditions for both bands.

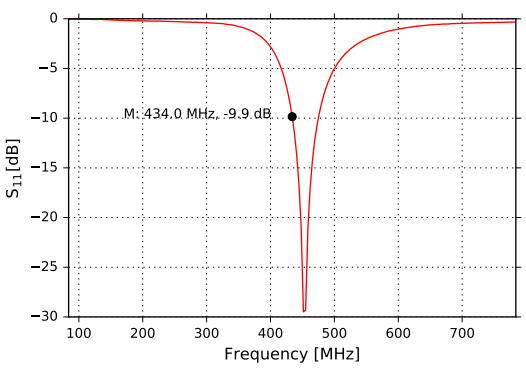

(a) S11 parameter for 434 MHz COTS antenna

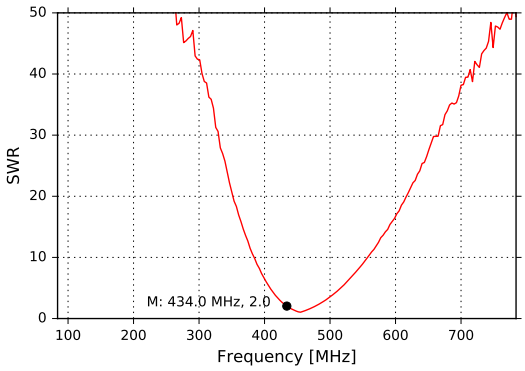

(b) SWR for 434 MHz COTS antenna

Figure 5.2: S11 and SWR for 434 MHz COTS antenna measured with Keysight N9915A FieldFox Microwave Analyzer and plotted with Python Matplotlib.

The measurements of S11 and SWR showed, that despite the fact that antennas are specified for nominal frequencies of 868 MHz and 434 MHz, and impedance of $Z_{\text{ant}} = 50\,\Omega$, there can be huge variations. On the other hand, since we were not able to accurately measure the gain and radiation pattern of the antennas, we relied on the manufacturer specifications which claim the following gains: 4.5 dBi and 0.7 dBi for 868 MHz and 434 MHz, respectively, with omnidirectional radiation patterns.

Finally, in some of the measurements, we deployed costly and bulky antennas for both frequencies of interest. Those antennas are also omnidirectional, three-element collinear dipoles providing significantly higher gain than COTS antennas used: 8.5 dBi and 6.5 dBi for 868 MHz and 434 MHz band, respectively.

5.2 Experimental Locations

The experimental locations are very important since they have to provide adequate propagation path conditions for complete evaluation of the performances of the developed transceiver and to put all transceivers in the test to the reception boundary

so their sensitivities can be compared. Moreover, the test locations should reflect one or more real-case scenarios and therefore make this experimental study useful also for practical deployments in industry.

In order to meet above requirements, we opted for two types of test scenarios: (1) Line-of-Sight (LOS) scenario over land, establishing very long links (> 100 km); and (2) LOS and obstructed LOS scenario over seawater, establishing long links (> 20 km). The first experimental scenario is very important for the implementation of early warning systems for e.g. volcano eruptions, landslides, avalanches, etc., while the second experimental scenario may be useful to connect environmental monitoring stations on islands inside archipelagos, which is, on a side note, a huge problem in island developing countries.

To find suitable test locations, a simulation software must be used which can calculate path loss between two arbitrary geographical points and depict terrain profile between them. For that purpose, we used BotRf [88], a software tool for wireless link planning that uses the Longley-Rice model to estimate path loss on a given trajectory using digital elevation maps. The process of finding suitable test locations was carried out through several iterations, to accommodate both LOS and obstructed LOS propagation paths, considering also the physical suitability for equipment deployment. Based on the outputs in BotRf, we created four different testbeds:

(a) 112 km long LOS testbed over land,

(b) 316 km long LOS testbed over land,

(c) 22 km long LOS testbed over seawater,

(d) 28 km long obstructed LOS testbed over seawater.

Geographical details of the test sites are summarized in the Table 5.1. Using coordinates of the test sites, we built the testbeds and calculated path losses for each propagation path at both frequencies of interests, namely 868 MHz and 434 MHz.

The location of testbeds and their description with the results of simulations obtained in BotRf are provided in Table 5.2, while the terrain profiles for the exper-

Table 5.1: Geographical details of test sites.

Site	Latitude	Longitude	Altitude	Toponym	Country
A	45.703800	13.720100	76 m	ICTP, Trieste	Italy
B	46.039200	12.362900	1406 m	Monte Pizzoc	Italy
C	45.521777	13.589979	133 m	Pacug	Slovenia
D	45.477700	13.557300	64 m	Kanegra	Croatia
E	46.212100	13.529400	1633 m	Matajur	Italy
F	44.132130	10.778920	1673 m	Croce Arcana	Italy

imental testbeds are depicted in Fig. 5.3.

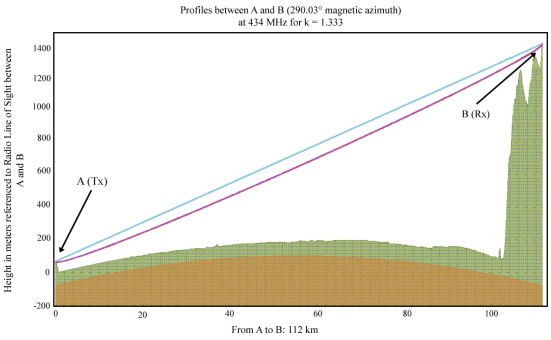

(a) Link A-B (112 km)

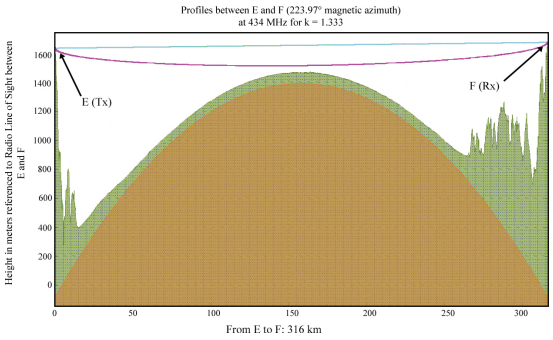

(b) Link E-F (316 km)

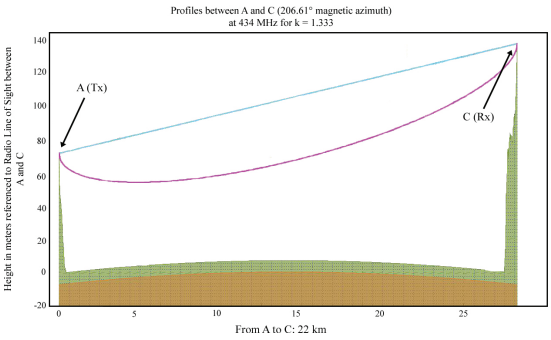

(c) Link A-C (22 km)

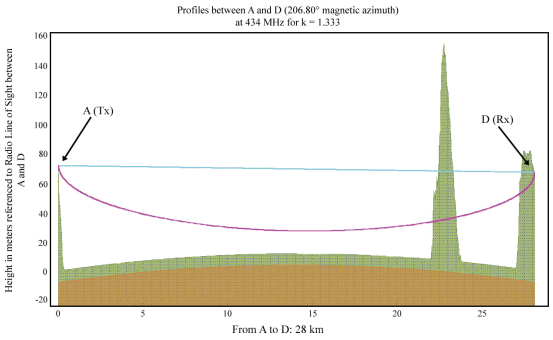

(d) Link A-D (28 km)

Figure 5.3: Terrain profiles for experimental testbeds: **(a)** Link A-B (LOS over land, 112 km); **(b)** Link E-F (LOS over land, 316 km); **(c)** Link A-C (LOS over seawater, 22 km); **(d)** Link A-D (blocked LOS over seawater, 28 km). Brown area indicates the curvature of the earth, modified by the refraction index; green area is the terrain profile as seen by the radio wave; magenta line corresponds to 60% of the first Fresnel zone; and blue line is the optical line of sight.

Table 5.2: Experimental testbeds' details.

Testbed	A-B	A-C	A-D	E-F
Mode of propagation	LOS over land	LOS over seawater	BLOS over seawater	LOS over land
Length	112 km	22 km	28 km	316 km
Longley-Rice path loss (868 MHz)	131.91 dB	118.26 dB	176.7 dB	152.82 dB
Longley-Rice path loss (434 MHz)	125.91 dB	112.25 dB	166.12 dB	145.96 dB
Free-space path loss (868 MHz)	132.18 dB	118.33 dB	–	141.24 dB
Free-space path loss (434 MHz)	126.16 dB	112.31 dB	–	135.22 dB
Terrain shielding att. (868 MHz)	−0.27 dB	−0.07 dB	56.47 dB	11.58 dB
Terrain shielding att. (434 MHz)	−0.26 dB	−0.06 dB	51.91 dB	10.74 dB

Finally in Fig. 5.4 details of the experimental testbeds are presented on the maps, using the same scaling for each map.

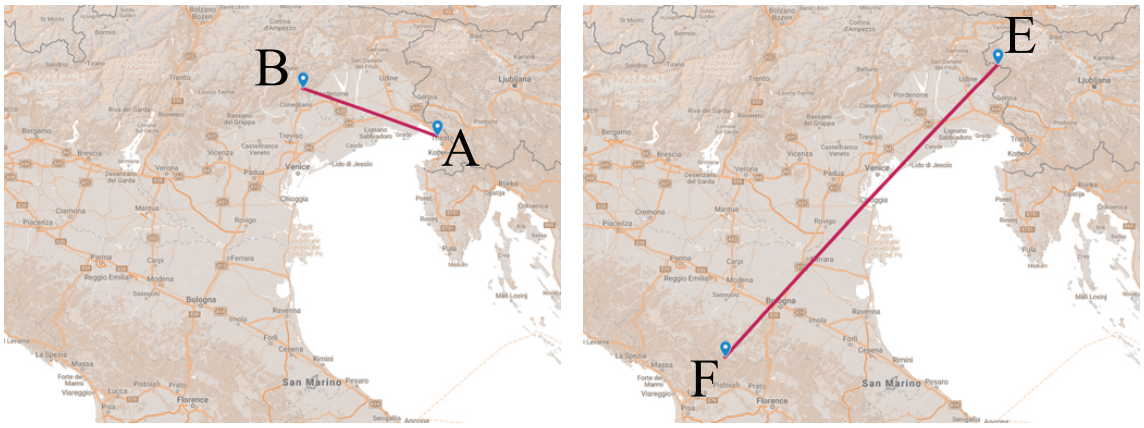

(a) Link A-B (112 km)

(b) Link E-F (316 km)

(c) Link A-C (22 km)

(d) Link A-D (28 km)

Figure 5.4: Experimental testbeds presented on the maps: **(a)** Link A-B (LOS over land, 112 km); **(b)** Link E-F (LOS over land, 316 km); **(c)** Link A-C (LOS over seawater, 22 km); **(d)** Link A-D (blocked LOS over seawater, 28 km).

5.3 Experimental Setup

All the experiments were carried out using the same layout. In each experiment, on the transmit side, two OdT transceivers were configured and deployed to transmit on two frequencies, namely on 868 MHz and 434 MHz. Transceivers were not synchronized, but they were operating simultaneously. On the receive side, there were always four transceivers configured as receivers - three were operating on 868 MHz, while one was operating on 434 MHz. The group of receivers operating on 868 MHz

consisted of two commercial transceivers (UpT and LiT) and one OdT, while on 434 MHz only one OdT was deployed. The reason that only one receiver was deployed at 434 MHz was purely technical - LiT and UpT do not have low-frequency port. Block diagram of the test setup is given in Fig. 5.5.

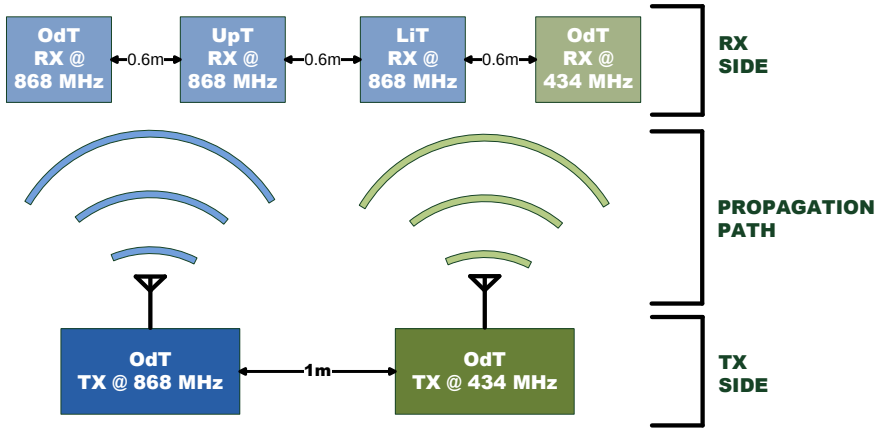

Figure 5.5: Block diagram of experimental setup.

The transmitters were mounted on a plastic antenna mast at a vertical distance of 1 m, which is enough to cancel mutual near-field effects on antenna radiation pattern of both transceivers. On the receive side, the receivers were mounted on a horizontal plastic bar, at a distance of 60 cm; the horizontal bar was attached on antenna mast forming a T-shape. In all experimental sites, receivers were mounted at 2.5 m above ground, while the transmitters were mounted on the antenna mast on the roof of the building, approximately 15 m above the ground.

The transceivers were mounted into IP-67 rated enclosures; the appearance of the OdT transceiver inside the enclosure is shown in Fig. 5.6.

5.4 Packet Transmission Pattern

The packet transmission pattern was designed to accommodate three main goals of the experimental study: (1) to investigate performances of the new LoRa transceiver in the field, (2) to compare it with two widely adopted commercial transceivers; and (3) to investigate very long LoRa links in two characteristic propagation scenarios, namely LOS and obstructed LOS.

Figure 5.6: OdT mounted inside IP-67 rated enclosure.

Since the improved performance of the new transceiver is mainly due to the hardware design of the transceiver, the communication protocol must not contain any overhead which can improve the transmission reliability because, in that case, we cannot distinguish whether the improvements are a consequence of the protocol, hardware design, or both. The same applies when it comes to comparison with commercial transceivers - we want to examine improvements and limitations that new transceiver exhibits analyzing exclusively the physical layer.

Keeping in mind the communication protocol limitations, we opted to implement a very simple transmission pattern, without sending any acknowledgments or retrial packets. In this way, the conclusions drawn from the experiments accurately reflects LoRa physical layer characteristics since the packet reception cannot be improved by the communication protocol. In addition, because we used three different transceivers in the tests, we excluded effects which could be a consequence of a single transceiver manufacturing peculiarities.

The transmitters were configured to send packets with an 8-byte preamble and 9-byte payload, with CRC and explicit header enabled. After transmitting a packet, the transmitter waited for $T_{\mathrm{w}} = 200\,\mathrm{ms}$ before sending the next packet. The resulting sending packet rate violates the maximum duty cycle allowed by European regulations [87] and therefore such configuration should not be adopted for commercial solutions to be deployed in Europe. However, for these experiments, this setting was required in order to observe the short-term temporal variability in re-

ception quality, which was one of the aspects in the focus of this research study. The transmit power on 868 MHz was set to the nominal value of 14 dBm, while for 434 MHz it was set to 20 dBm.

In each experiment 20 000 packets were sent. The LoRa bandwidth and coding rate were fixed to BW = 125 kHz and CR = 4/6 whereas for spreading factor we tested three different values, namely SF $\in \{7, 10, 12\}$. On the receiving side, for each correctly decoded packet m the receiver logged the time-stamp, the packet identifier, RSS $r[m]$ and SNR $s[m]$ values as reported in the corresponding modem registers. These were the input measurement data to the analysis presented in the next section.

It is worth remembering that experiment durations are different for different LoRa parameters, despite the fact that the same number of packets was sent. In Table 5.3 LoRa packet timing details for parameters used in the experiments are given based on the calculus provided in the previous chapter.

Table 5.3: Packet airtimes for different SFs when BW = 125 kHz and CR = 4/6.

	SF=7	**SF=10**	**SF=12**
Symbol Time	1.02 ms	8.19 ms	32.77 ms
Preamble Duration	12.54 ms	100.35 ms	401.41 ms
Airtime	51.46 ms	313.14 ms	1056.77 ms
Equivalent Bitrate	4557.29 bps	813.8 bps	244.14 bps
Experiment Duration	84 min	171 min	419 min

As can be seen, by increasing the spreading factor within the same bandwidth of BW = 125 kHz, the symbol time is increasing. Consequently, the preamble duration and packet airtime are increasing. It is interesting to note that packet airtime for the SF = 7 is shorter by 1 second than for the SF = 12. On the other hand, the equivalent bit rate is decreasing by increasing the spreading factor. For example, for spreading factor SF = 12, it yields only 214 bps. Finally, there are significant differences in experiment durations as well: for SF = 7 the duration is only 84 minutes, while for SF = 12 the experiment duration is 7 hours for the same number of packets sent!

5.5 Experimental Results and Discussion

The measurement campaign encompassed a variety of experimental scenarios, transceivers, and LoRa parameters. As stated earlier, we explored two characteristic propagation paths: LOS over land and LOS over seawater. In addition, we investigated packet reception over seawater when LOS is obstructed with knife-edge obstacle. In LOS over land scenario, we focused our research on very long and ultra-long links.

By using three different transceivers in the experiments, we improved the accuracy of the conclusions drawn from the experiments. Moreover, we chose characteristic LoRa parameters in order to make our conclusions general and relevant also in real use case scenarios. We opted to investigate three different spreading factors $\mathrm{SF} \in \{7, 10, 12\}$ within a fixed bandwidth of $\mathrm{BW} = 125\,\mathrm{kHz}$, using coding rate of $\mathrm{CR} = 4/6$. The bandwidth is chosen based on the specification of LoRaWAN standard which restricts the use of other values. On the other hand, we opted for the specified coding rate because it is the mid-range of possible values, and since it does not influence the sensitivity of the transceiver, we decided not to vary this parameter. On the contrary, because the spreading factor significantly impacts the sensitivity, we opted to vary this parameter and investigate how it affects the packet reception rate in the different experimental scenarios. We selected it based on a lowest, mid-range and highest spreading value. One can notice that we chose $\mathrm{SF} = 7$ as a minimum value, despite the fact that RF ICs are capable of using $\mathrm{SF} = 6$. This was done because the usage of $\mathrm{SF} = 6$ is limited to a special packet structure, i.e. a packet with explicit header disabled. Since this is a special case, rarely used in practice, we decided not to include this value in the experiments.

From the presented, it can be inferred that we performed three experiments on every testbed, incrementing the spreading factor in each experiment and keeping the bandwidth and coding rate fixed.

During the experiments, we logged the time stamp, packet identification number, RSS and SNR in the local memory of the transceivers. In the post-processing of the recorded data, we added a flag Packet Reception Indicator (PRI) in the following manner: for each received packet we added $\mathrm{PRI} = 1$, whereas for the missing packet

we added PRI = 0 together with missing packet identification number. That was performed in order to plot packet reception rate, calculated as a rolling mean on the 1-minute window. The same calculations were performed for RSS and SNR, to differentiate between slow and fast-term fluctuations. To be able to estimate adequate value for a time window, we plotted the distribution of the difference between the current and rolling mean values of RSS and SNR. The time window was set to be 1 minute since, in this case, their distribution can be approximated with Gaussian; this is exactly how these distributions must look because they represents the measurement "noise".

The experimental results and analysis are divided into four groups: (1) LOS over land, (2) LOS over seawater, (3) obstructed LOS over seawater; and (4) cumulative packet loss analysis. Further, the results are divided based on the testbed length, and the frequency band of interest. In each scenario three different sets of LoRa parameters were investigated, namely SF $\in \{7, 10, 12\}$ within a fixed bandwidth of BW = 125 kHz and using coding rate CR = 4/6. The graphical organization of the experimental results is given in Fig. 5.7.

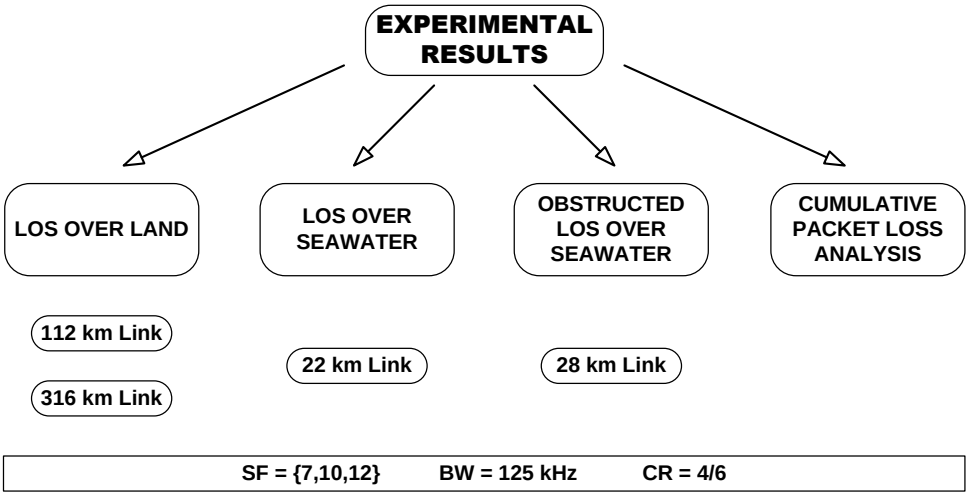

Figure 5.7: Organization of the experimental results.

The experimental results are presented both in the time domain and cumulatively, using histograms. The plots in time domain show current values represented by dots, and their moving average values represented with solid lines. The colors on the plots are consistent throughout the chapter, namely blue represents OdT at

868 MHz, black represents LiT at 868 MHz, green represents UpT at 868 MHz, while red represents OdT at 434 MHz.

5.5.1 LOS Over Land Experimental Scenario

This group of experiments aimed to investigate very long LoRa links in LOS over land scenario at two link lengths, namely 112 km and 316 km, as well as to comparatively explore performances of the new transceiver and two widely adopted commercial transceivers. As already stated, two transmitters were mounted at point A (ICTP), transmitting on 868 MHz and 434 MHz, while three different receivers operating on 868 MHz and one on 434 MHz were mounted at point B (Monte Pizzoc) covering the length of 112 km. On the other hand, in 316 km long link, transmitters were deployed at point E (Matajur), while the receivers were deployed at point F (Croce Arcana). Various LoRa parameters were investigated in three consecutive experiments in 112 km experimental scenario, namely SF $\in \{7, 10, 12\}$, within a fixed bandwidth, BW = 125 kHz and coding rate, CR = 4/6. In 316 km experimental scenario only one spreading factor was tested, SF = 10.

112 km LOS over land results at 868 MHz

In Fig. 5.8 experimental results for SF = 7 are given. It can be seen that the RSS fluctuation trend for all three transceivers is approximately the same during the whole experiment, except in the periods between $40 - 60$ and $70 - 80$ minute. In those two intervals, OdT experienced the biggest dip in RSS, while LiT and UpT maintained relatively small change, about 2 dB. However, SNR of OdT constantly stays the highest, which can be explained by the highest sensitivity of OdT transceiver. This is based on the fact that all the transceivers in the test receive packets from the same transmitter while positioned on the same location. Inspecting PRR during those intervals, we observe that the packet loss experienced by the OdT was 0 %, whereas LiT and UpT recorded significant packet loss. Since these two intervals are the intervals where strong external interference occurred, we infer that the OdT has the highest immunity to external interference. On the contrary, LiT was severely impinged by external interference revealing its high susceptibil-

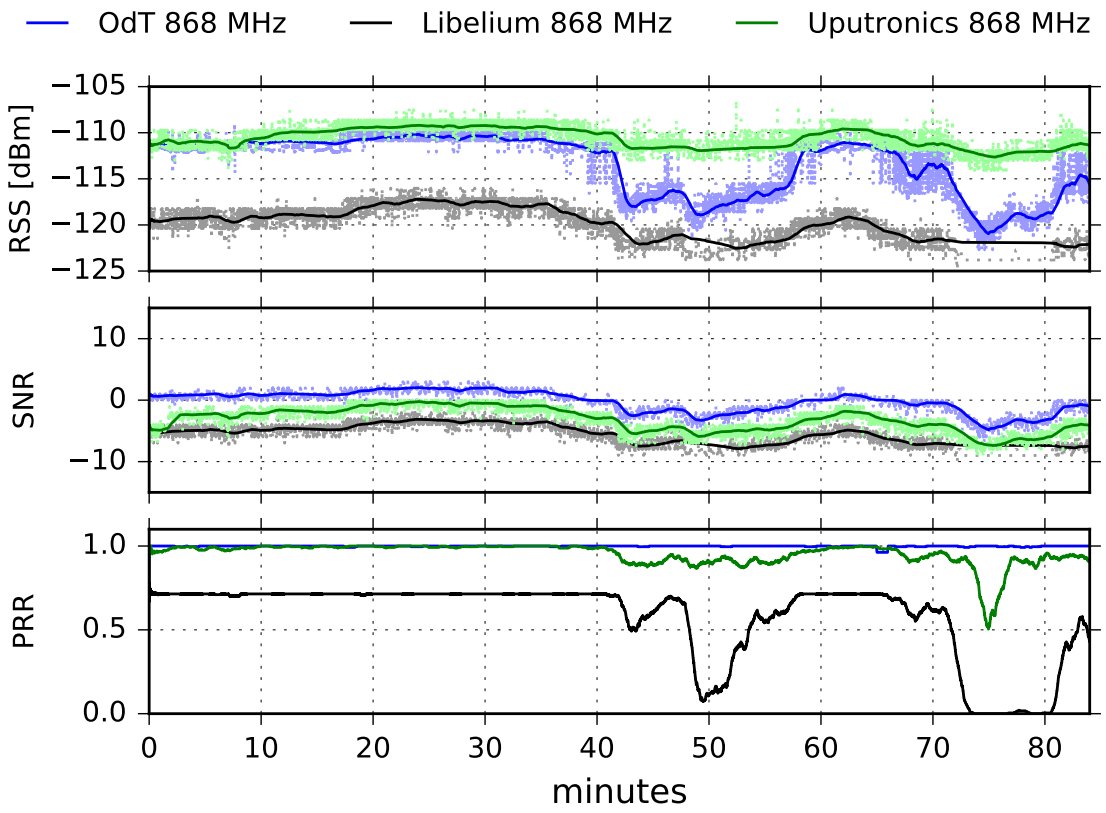

Figure 5.8: RSS, SNR, and PRR for 112 km LOS link over land for OdT, LiT, and UpT at 868 MHz. LoRa test parameters: BW = 125 kHz, SF = 7, CR = 4/6.

ity to external noise, while UpT exhibited moderate level of immunity to external interferences.

Figure 5.9 gives cumulative results in the form of histograms for 112 km LOS experimental scenario deploying SF = 7 on 868 MHz. In 5.9a, distribution of RSS moving average samples is given, while in 5.9b a distribution of the difference between moving average and current value of RSS is given. In that way, we isolated RSS "noise" caused by multipath and fading effects from the signal received. Moreover, the distribution of RSS samples, in this case, is Gaussian, which indicates that the 1-minute sliding window is adequate value for calculating the moving average values. In addition, distribution of moving average values also shows that there were no big fluctuations of RSS except in the case of OdT.

Similar observations can be made for the results presented in Fig. 5.9c and 5.9d. These figures present the SNR moving average values and the difference between moving average and current values of SNR for the same LoRa parameters as in

Figs. 5.9a and 5.9b. The distribution of the SNR samples in Fig. 5.9b is also Gaussian which confirms the previous conclusions.

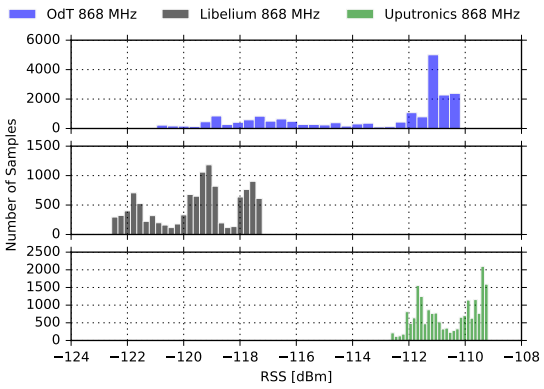

(a) RSS: 1-minute window moving average

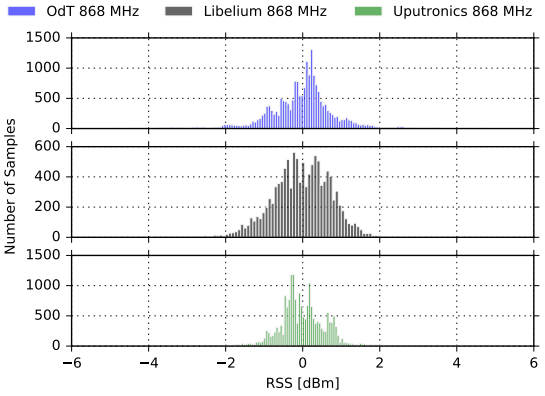

(b) RSS: 1-min window m. avg. fluctuations

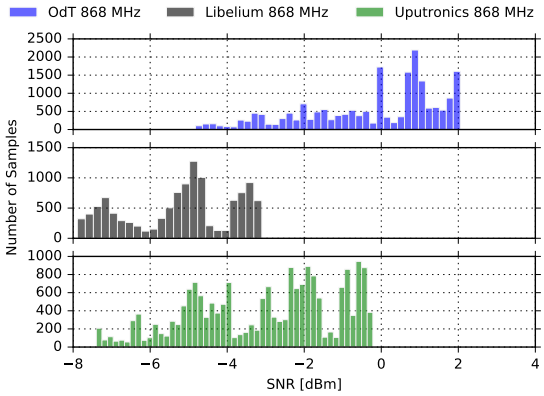

(c) SNR: 1-minute window moving average

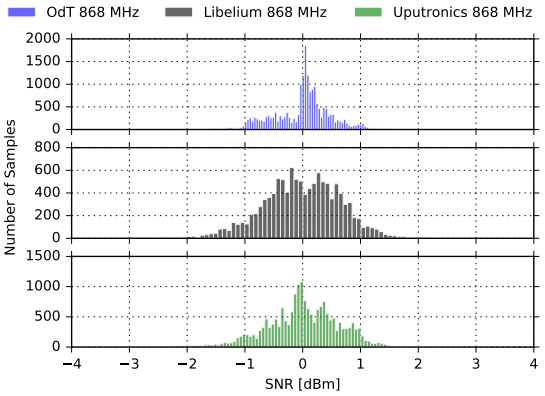

(d) SNR: 1-min window m. avg. fluctuations

Figure 5.9: RSS and SNR histograms for OdT, Uputronics, and Libelium: $f = 868\,\text{MHz}$, $\text{BW} = 125\,\text{kHz}$, $\text{SF} = 7$, $\text{CR} = 4/6$, LOS over land, 112 km.

Figure 5.10 shows results for the OdT, LiT and UpT transceivers over 112 km long link in LOS over land scenario, using following LoRa parameters: $\text{SF} = 10$, $\text{BW} = 125\,\text{kHz}$, and $\text{CR} = 4/6$. We observe very strong external interference in the interval $130-170$ minute. In that interval, the RSS values recorded by OdT reach the lowest values, while the commercial transceivers do not receive the packets almost at all (recall that RSS and SNR are logged only for the received packets). Despite the fact that the RSS values at the receive pins of OdT transceiver were not the highest, the SNR values were again the highest during the whole experiment. This once again confirms superior characteristics of the OdT in terms of noise floor and consequently

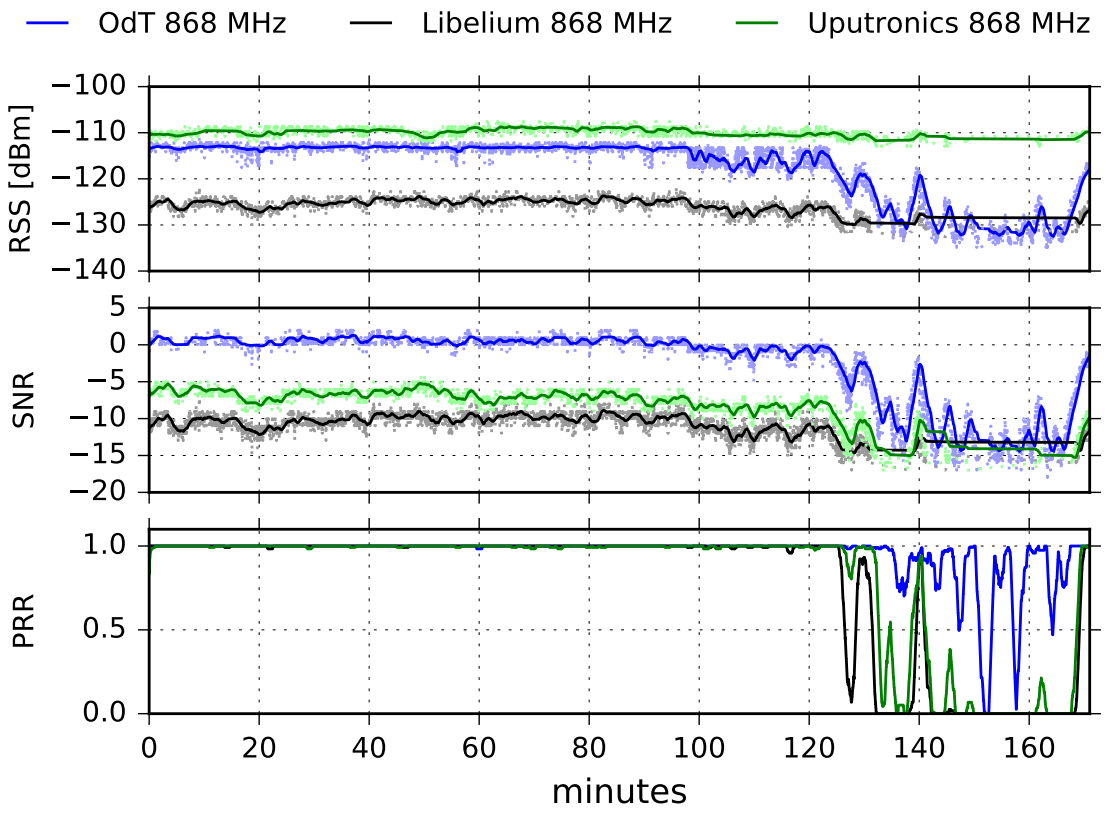

Figure 5.10: RSS, SNR, and PRR for 112 km LOS link over land for OdT, LiT, and UpT at 868 MHz. LoRa test parameters: BW = 125 kHz, SF = 10, CR = 4/6.

the sensitivity, compared to commercial transceivers. In addition, comparing the PRR values in this interval, we clearly see that OdT shows the highest immunity to the external interference in comparison to commercial transceivers. Namely, while LiT and UpT PRR was almost PRR = 0 %, OdT had moderate packet loss with only two short dips down to PRR = 0 %.

Figures 5.11a and 5.11b show RSS moving average values and fluctuations of RSS calculated for the 1-minute window for the following LoRa parameters: SF = 10, BW = 125 kHz, and CR = 4/6. As can be seen in Fig. 5.11b, the distribution of the samples is Gaussian, which confirms adequate time window for RSS calculation of moving average; the same also applies to SNR calculations. From Fig. 5.11a we can observe the multipath propagation effect which was recorded by all three transceivers. On the other hand, Fig. 5.11b again shows OdT's superior characteristics in terms of noise floor. Namely, most of the packets received by OdT were logged with very high SNR, namely SNR = 1; at the same time, two other receivers,

LiT and UpT, recorded SNR = −10 and SNR = −7, respectively. Due to this difference in the noise floors, the OdT was able to maintain the lowest packet loss even during high interference bursts.

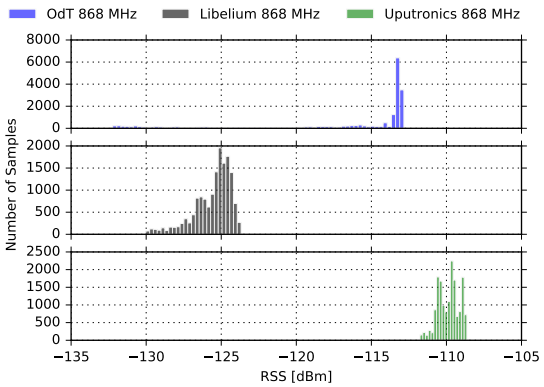

(a) RSS: 1-minute window moving average

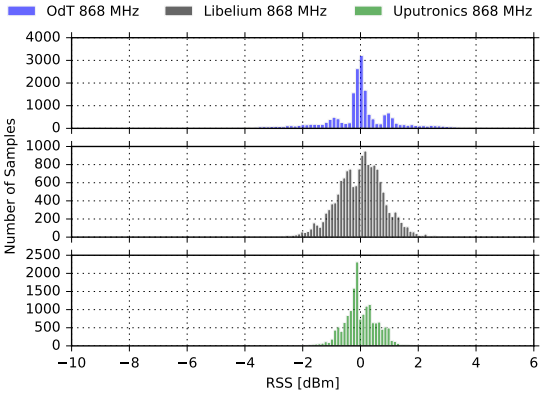

(b) RSS: 1-min window m. avg. fluctuations

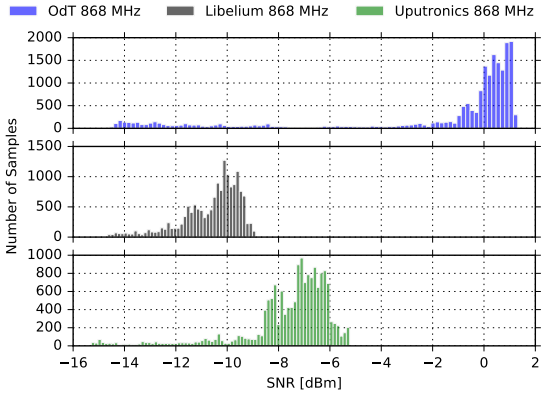

(c) SNR: 1-minute window moving average

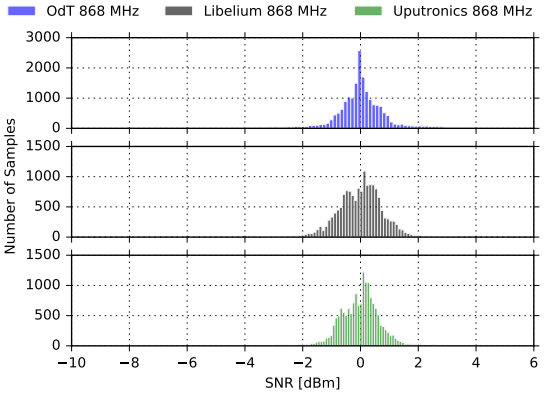

(d) SNR: 1-min window m. avg. fluctuations

Figure 5.11: RSS and SNR histograms for OdT, Uputronics, and Libelium: $f = 868\,\text{MHz}$, $\text{BW} = 125\,\text{kHz}$, $\text{SF} = 10$, $\text{CR} = 4/6$, LOS over land, 112 km.

Figure 5.12 shows results obtained in the experiment for the SF = 12, BW = 125 kHz, and CR = 4/6. The huge fluctuations of the received signal strength are recorded by all three receivers; this implies very pronounced multipath propagation effects. It can be noticed that, when the SNR reaches the minimum value, the receivers experience packet loss. In addition, the packet loss can be observed also when the RSS and SNR are within the link margins. This packet loss is attributed to the effects of external interference. In addition, due to very long packet airtime in this case (more than 1 second), the probability for external interference to couple to

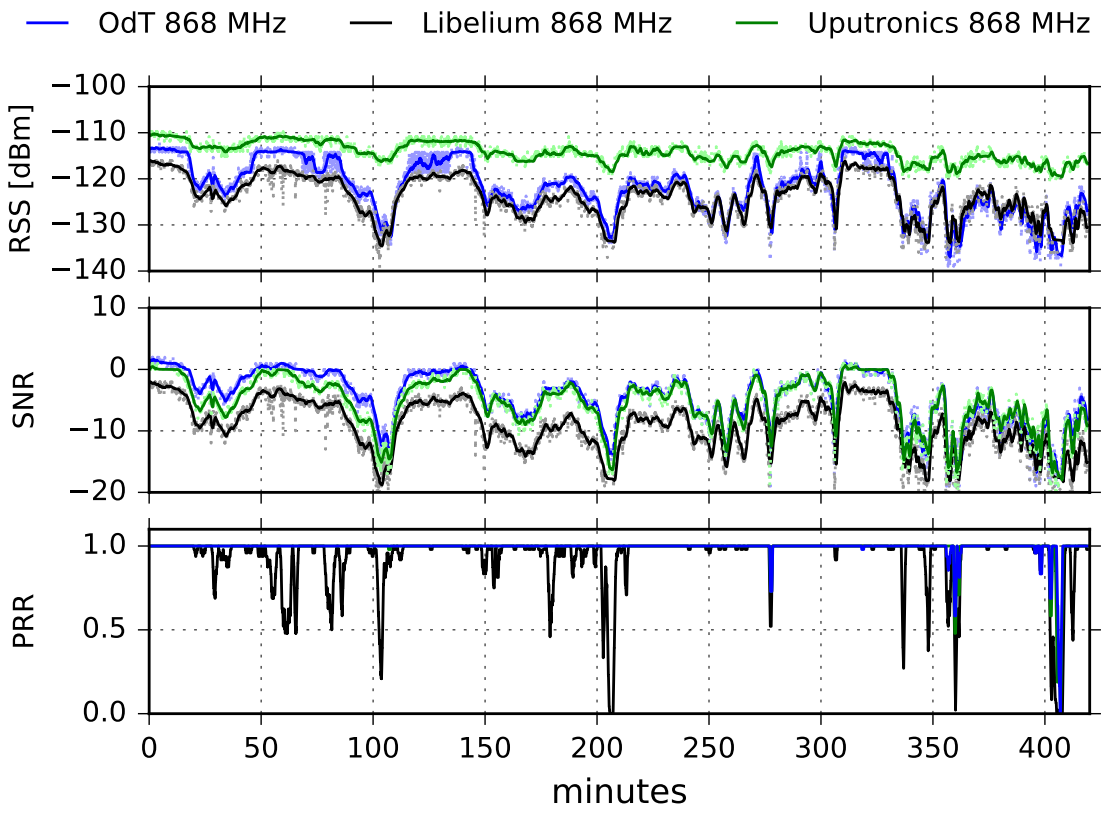

Figure 5.12: RSS, SNR, and PRR for 112 km LOS link over land for OdT, LiT, and UpT at 868 MHz. LoRa test parameters: BW = 125 kHz, SF = 12, CR = 4/6.

the transceivers and impair the packet reception is increased. This has to be taken into account when it comes to link planning since this experiment showed that a higher sensitivity of the transceiver in LoRa networks does not necessarily imply a higher transmission reliability. The SNR values again indicate lower noise floor of OdT since it recorded the highest SNR values; this is also valid in the regions where the SNR values are equal to the values recorded by the UpT since in this regions the OdT logged lower values of RSS.

Figure 5.13 presents the distribution of the moving averages of RSS and SNR as well as their fluctuations calculated as a difference between the corresponding moving average and their current values. The results are obtained using following LoRa parameters: SF = 12, BW = 125 kHz, and CR = 4/6. Distributions of RSS and SNR fluctuations verify the appropriate time window selection also in this case. On the other hand, the distribution of moving average values confirms that there was a dominant multipath effect in the case of all three transceivers.

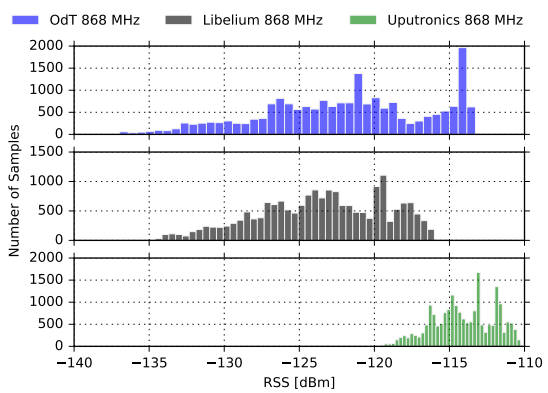

(a) RSS: 1-minute window moving average

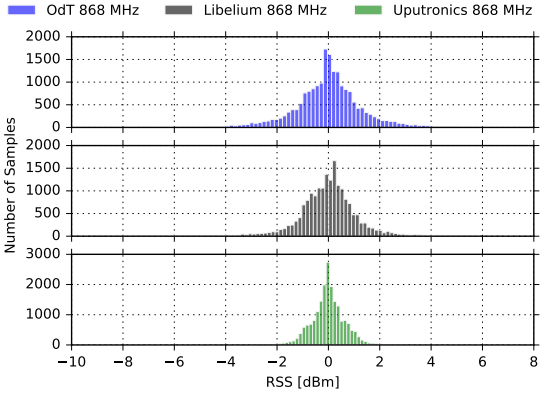

(b) RSS: 1-min window m. avg. fluctuations

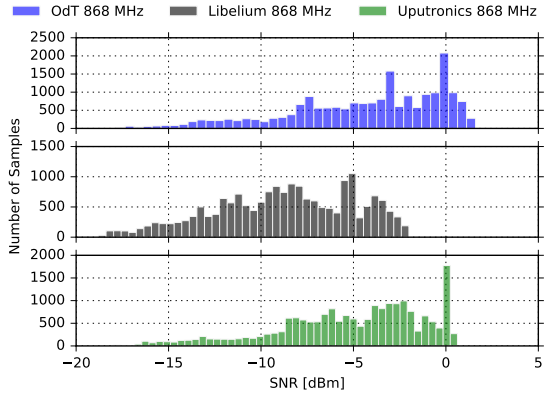

(c) SNR: 1-minute window moving average

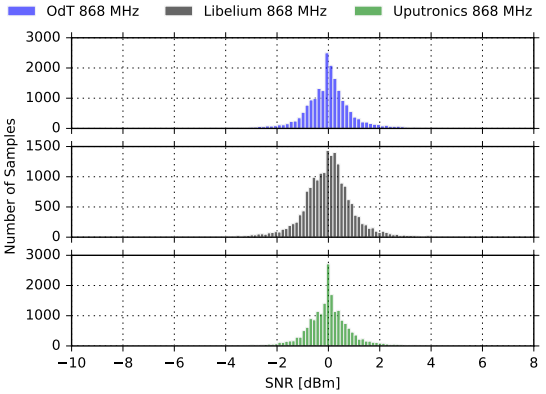

(d) SNR: 1-min window m. avg. fluctuations

Figure 5.13: RSS and SNR histograms for OdT, Uputronics, and Libelium: $f = 868\,\text{MHz}$, $\text{BW} = 125\,\text{kHz}$, $\text{SF} = 12$, $\text{CR} = 4/6$, LOS over land, 112 km.

112 km LOS over land results at 434 MHz

The experiments on 434 MHz were carried out using a pair of OdT transceivers, namely one was configured as a transmitter while the second was configured as a receiver; there were no commercial transceivers in the test since they have only 868 MHz frequency port. As already said, three different sets of LoRa parameters were investigated: $\text{SF} \in \{7, 10, 12\}$ within a fixed bandwidth of $\text{BW} = 125\,\text{kHz}$ and coding rate, $\text{CR} = 4/6$.

Figure 5.14 shows experimental results for the $\text{SF} = 7$, $\text{BW} = 125\,\text{kHz}$ and $\text{CR} = 4/6$. Received signal strength does not exhibit huge slow-term fluctuations, while SNR records significant fluctuations at the same time. This can be explained

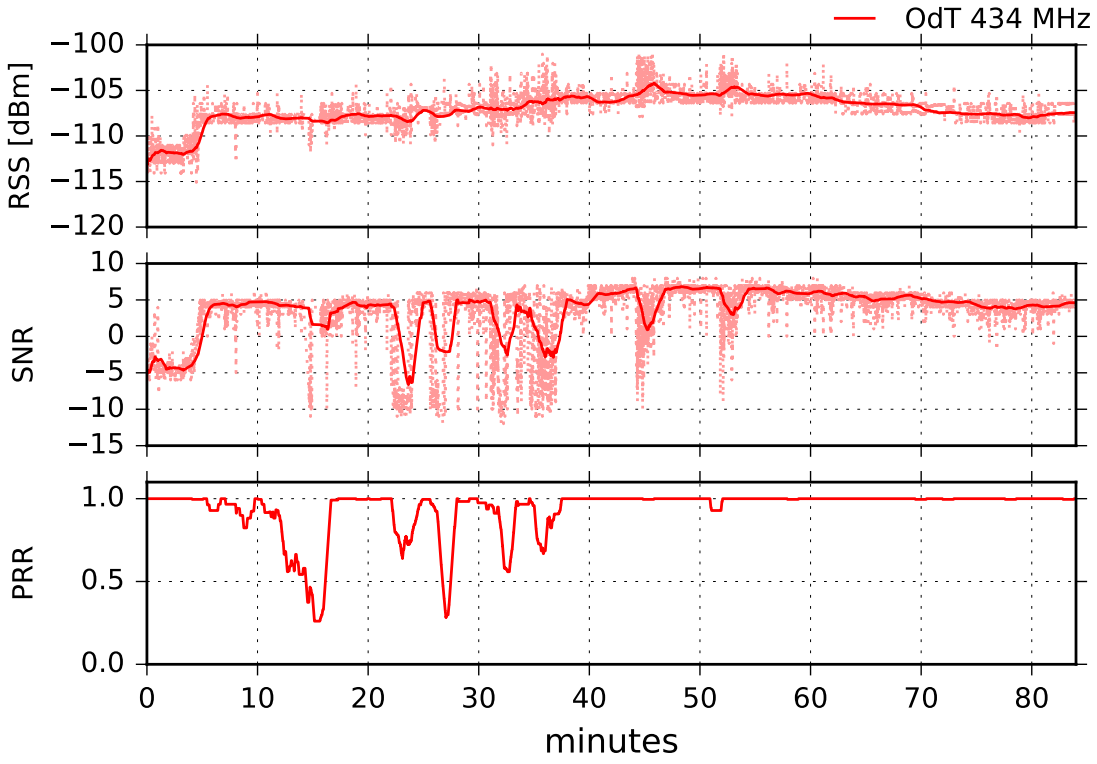

Figure 5.14: RSS, SNR, and PRR for 112 km LOS link over land for OdT at 434 MHz. LoRa test parameters: BW = 125 kHz, SF = 7, CR = 4/6.

by external interference which sporadically affects the transceiver. The external interference also affected PRR; packet loss occurs whenever the current value of SNR reaches SNR $= -10$, despite the fact that the RSS is significantly above the reception margin. This implies that SNR can also be used as a valid parameter for the link assessment in LoRa systems.

Figure 5.15 represent cumulative results for the same LoRa parameters. Distribution of RSS and SNR fluctuations can be approximated with Gaussian which confirms proper time window for moving average calculations. On the other hand, RSS averaged values are concentrated in a narrow range, between RSS $\in [-108, -105]$ dBm, which indicates the absence of the strong multipath propagation effects.

Figure 5.16 shows experimental results obtained for the following LoRa parameters: SF = 10, BW = 125 kHz, and CR = 4/6. We observe a strong decrease of RSS between $20 - 30$ minute of the experiment which is reflected in the decreased PRR in the same interval. The RSS and SNR exhibit the same fluctuation trend

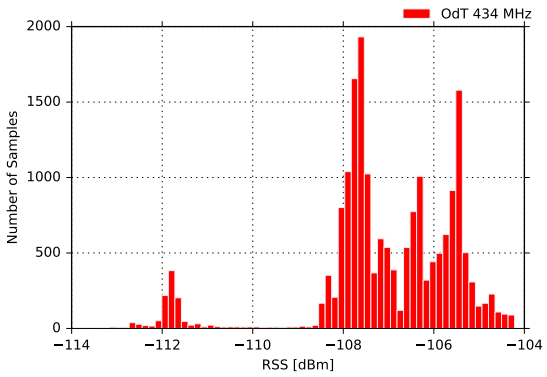

(a) RSS: 1-minute window moving average

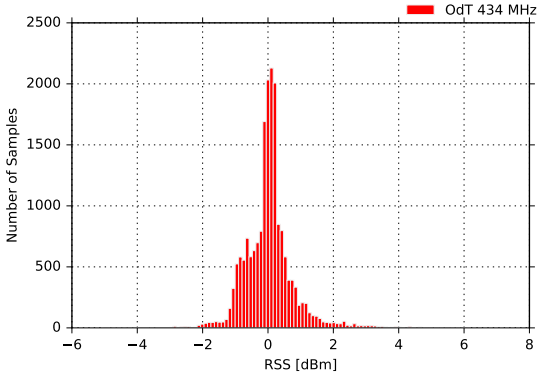

(b) RSS: 1-min window m. avg. fluctuations

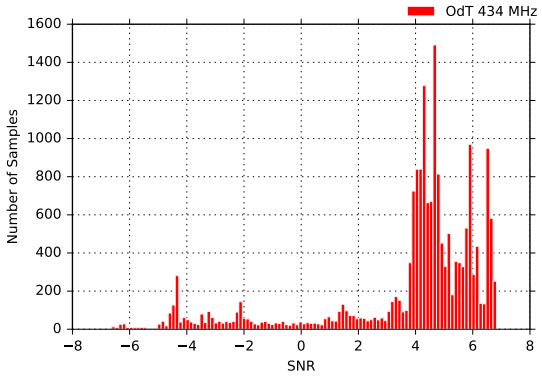

(c) SNR: 1-minute window moving average

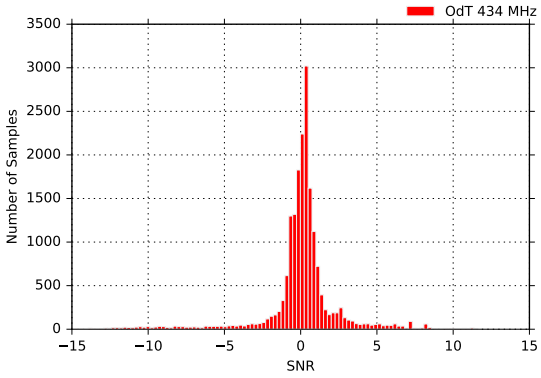

(d) SNR: 1-min window m. avg. fluctuations

Figure 5.15: RSS and SNR histograms for OdT: $f = 434\,\text{MHz}$, BW $= 125\,\text{kHz}$, SF $= 7$, CR $= 4/6$, LOS over land, 112 km.

during the whole experiment and since the changes are slow, we can attribute this to multipath propagation effect; the external interference did not have any significant impact on the packet reception rate nor on the RSS or SNR.

The distribution of the RSS and SNR fluctuations is depicted in Figs. 5.17b and 5.17d. It can be noticed that the distribution is Gaussian, therefore we can infer that moving average calculations are valid also in this case. The same conclusions made in the time domain can be also observed in this case: the huge fluctuation range of RSS and SNR is clearly observed, indicating a pronounced multipath propagation.

Figure 5.18 shows experimental results acquired for the SF $= 12$, BW $= 125\,\text{kHz}$, and CR $= 4/6$. We observe that SNR follows RSS fluctuation trend very accurately. On the other hand, due to very high fluctuations, we can infer that in this experiment, multipath propagation effect was very strong; however, it did not impair the

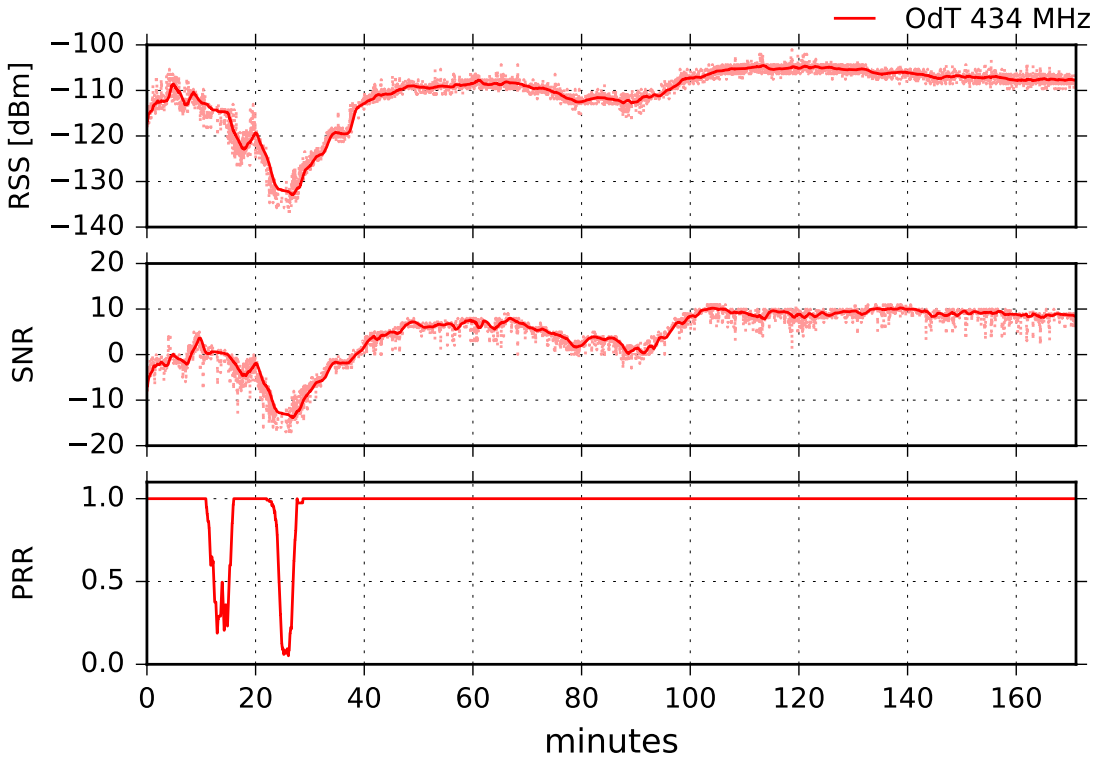

Figure 5.16: RSS, SNR, and PRR for 112 km LOS link over land for OdT at 434 MHz. LoRa test parameters: BW = 125 kHz, SF = 10, CR = 4/6.

packet reception except in two very short periods: at the beginning, and at the end of the experiment.

Multipath propagation effect can be even better recognized in the Figs. 5.19a and 5.19c. It can be seen that the samples are distributed in the very wide range, RSS $\in [-120, -105]$ dBm, indicating huge fluctuations; this is similar with SNR values. In addition, we observe that SNR sporadically reaches SNR $= -20$ which shows again very low noise floor of the OdT since, even in that case, the OdT was able to receive packets.

316 km LOS over land results at 868 MHz

The focus of this group of experiments was to test maximum range that could be achieved using newly developed transceiver as well as commercial transceivers. Due to very difficult terrain where the transceivers had to be deployed, we decided to experiment with only one set of LoRa parameters, using SF = 10 as a mid-range

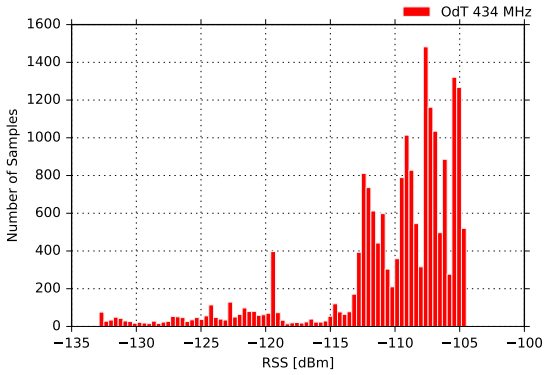

(a) RSS: 1-minute window moving average

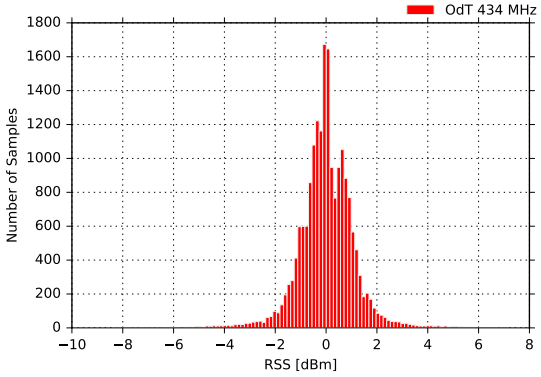

(b) RSS: 1-min window m. avg. fluctuations

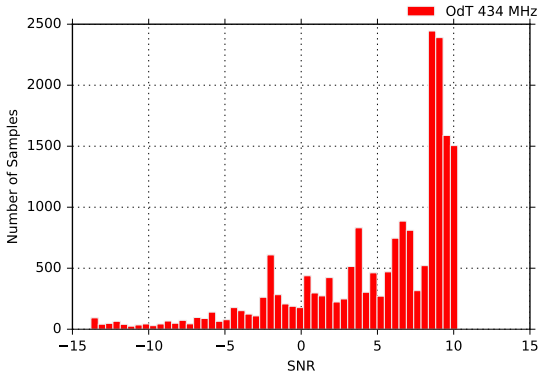

(c) SNR: 1-minute window moving average

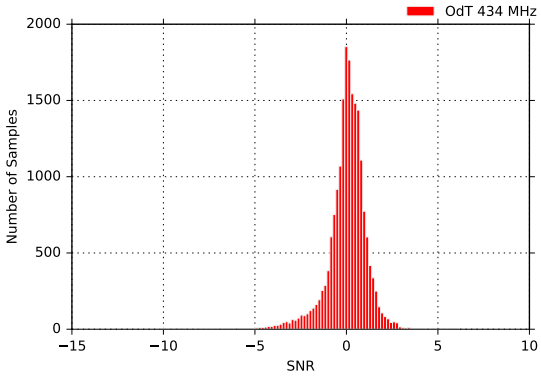

(d) SNR: 1-min window m. avg. fluctuations

Figure 5.17: RSS and SNR histograms for OdT: $f = 434\,\text{MHz}$, BW $= 125\,\text{kHz}$, SF $= 10$, CR $= 4/6$, LOS over land, 112 km.

value, a bandwidth of BW $= 125\,\text{kHz}$, and CR $= 4/6$. Here it has to be noted that only OdT transceiver was able to receive the packets at this distance.

The initial setup for this experiment included low-cost omnidirectional COTS antennas installed on both ends. Since we were not able to receive any packet in this case, we replaced the antenna on transmit side with omnidirectional, three-element collinear dipole with a higher gain of 8.5 dBi; after that we were able to receive packets.

As can be seen in Fig. 5.20, the 868 MHz link is entirely feasible. Receive signal strength experienced significant fluctuations which was the consequence of the multipath propagation effects and the SNR followed the same fluctuation trend. Both RSS and SNR were on the boundaries of the reception margin, but the OdT was still able to receive packets. There was one interference burst in the interval of

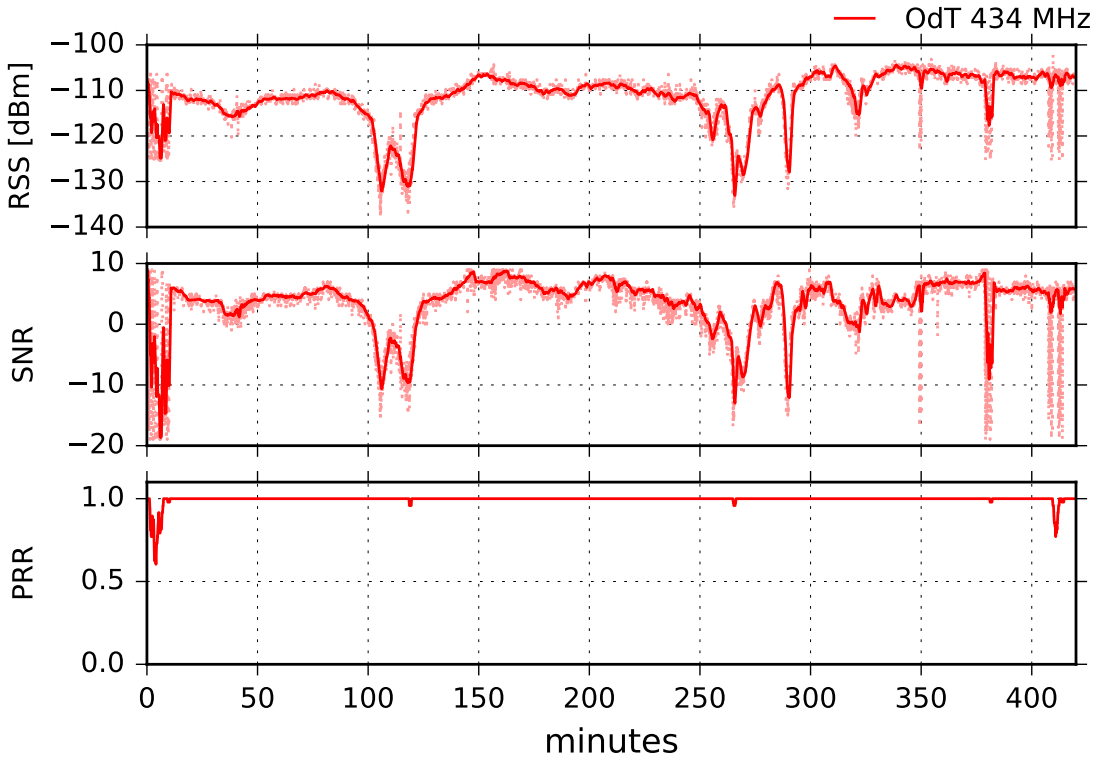

Figure 5.18: RSS, SNR, and PRR for 112 km LOS link over land for OdT at 434 MHz. LoRa test parameters: BW = 125 kHz, SF = 12, CR = 4/6.

18 − 22 minute, however, PRR still remained reasonably high.

It is interesting to note that both RSS and SNR reached values below the minimum specified in the corresponding datasheet for SX1276 RF IC and the OdT was still able to decode received packets. This confirms the conclusions drawn from the sensitivity experiments carried out in the laboratory, and previously performed field experiments.

Figure 5.21 shows cumulative results for both RSS and SNR fluctuations and their moving average values calculated within a 1-minute time window. We used the following LoRa parameters: SF = 10, BW = 125 kHz, and CR = 4/6. The distribution of the RSS and SNR fluctuations clearly shows that the time window for the calculation of moving average was properly selected. Moreover, the distribution of the RSS and SNR moving averages confirms the very strong multipath effect. The RSS reaches −134 dBm while SNR goes down to −16. This again confirms the low noise floor of the OdT transceiver, which in this particular case exceeded the

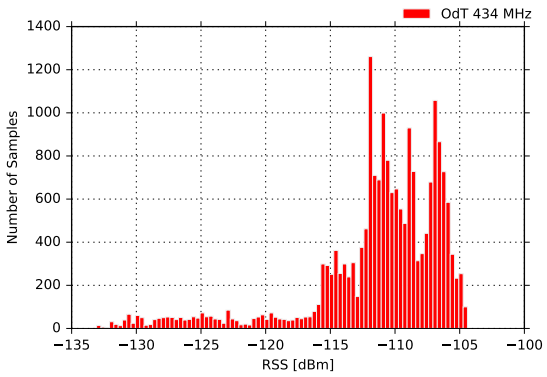

(a) RSS: 1-minute window moving average

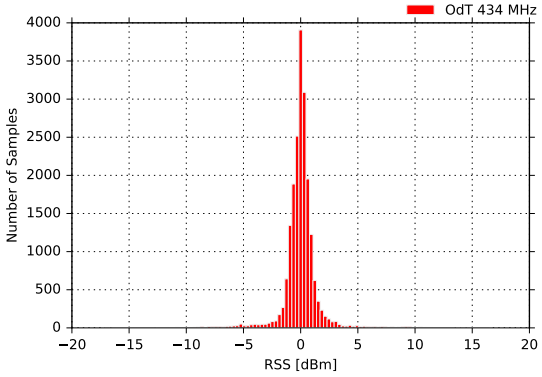

(b) RSS: 1-min window m. avg. fluctuations

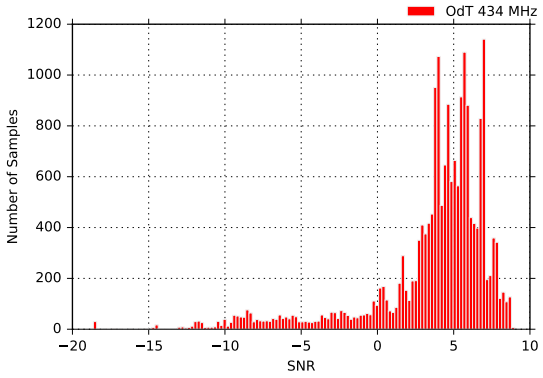

(c) SNR: 1-minute window moving average

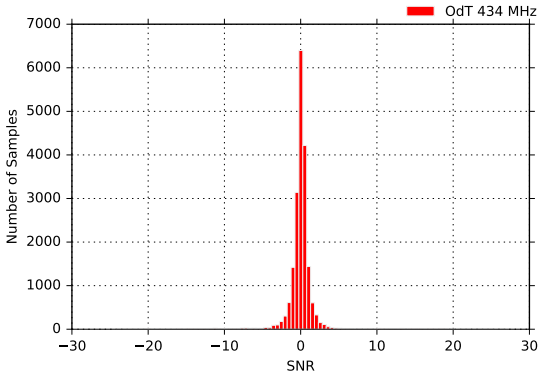

(d) SNR: 1-min window m. avg. fluctuations

Figure 5.19: RSS and SNR histograms for OdT: $f = 434\,\text{MHz}$, BW $= 125\,\text{kHz}$, SF $= 12$, CR $= 4/6$, LOS over land, 112 km.

one specified in the datasheet for RF IC used to implement OdT transceiver. This is due to, as already explained, the methodology used in the hardware development of the transceiver.

316 km LOS over land results at 434 MHz

Figure 5.22 presents results obtained in the experiment for the following LoRa parameters: SF $= 10$, BW $= 125\,\text{kHz}$, and CR $= 4/6$. Due to the already explained reasons, only this set of LoRa parameters was investigated.

We observe very huge fluctuations of both RSS and SNR, and also the identical fluctuation trend of RSS and SNR. These fluctuations are a consequence of the dominant multipath propagation effects. On the other hand, packet reception was

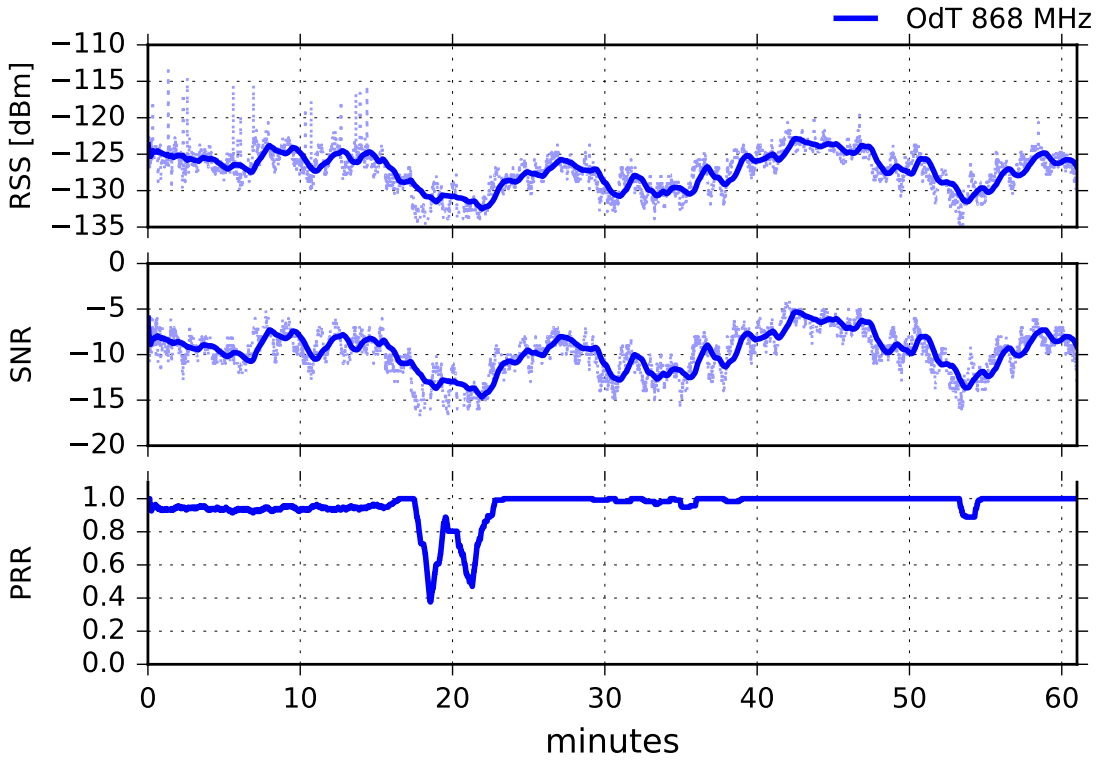

Figure 5.20: RSS, SNR, and PRR for 316 km LOS link over land for OdT at 868 MHz. LoRa test parameters: BW = 125 kHz, SF = 10, CR = 4/6.

not significantly affected, namely there was a sporadic packet loss which could be easily handled with a communication protocol.

Cumulative experimental results given in Fig. 5.23 reflect the conclusions drawn from the time domain. Namely, Fig. 5.23a shows that RSS excursions are in the wide range, RSS $\in [-135, -107]$, reaching again RSS values below the theoretical minimum specified in the datasheet for RF IC used to implement the OdT transceiver. The distributions of the difference between RSS and SNR moving average and current values are Gaussian, indicating again the proper time windowing for the calculation of the RSS and SNR moving average values.

The experimental results obtained in this group of measurements show that LoRa links can be established over extended ranges in both frequency bands for virtually any combination of LoRa parameters. Furthermore, it has been shown that packet transmission is possible even over extreme link lengths, longer than 300 km, using omnidirectional antennas. This qualifies LoRa technology to be deployed in early

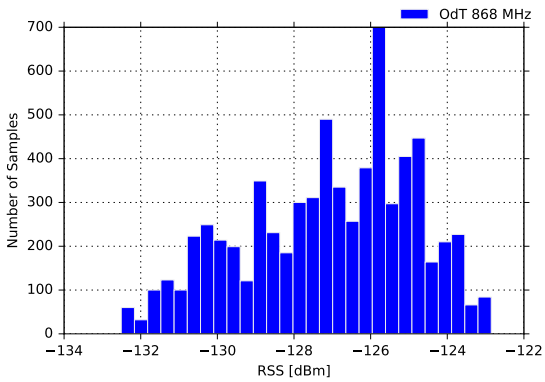

(a) RSS: 1-minute window moving average

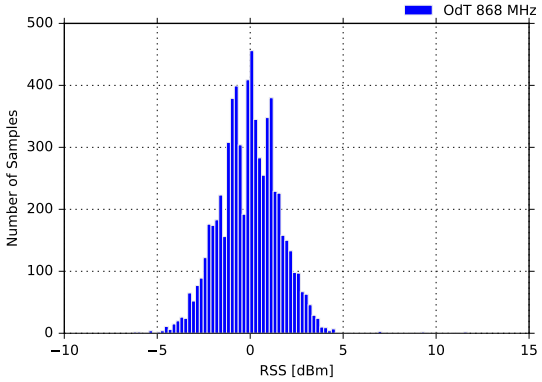

(b) RSS: 1-min window m. avg. fluctuations

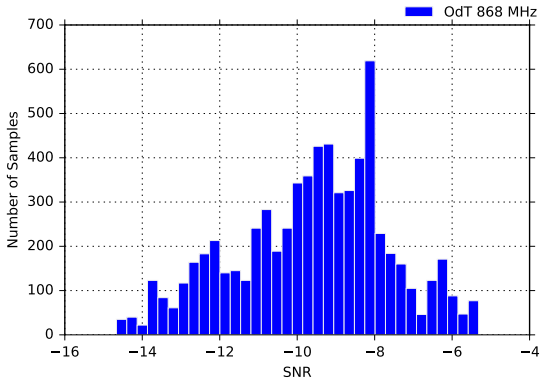

(c) SNR: 1-minute window moving average

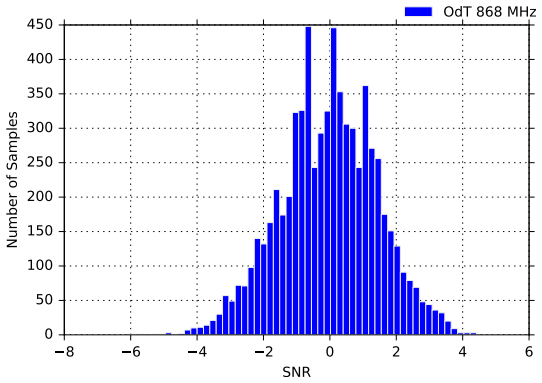

(d) SNR: 1-min window m. avg. fluctuations

Figure 5.21: RSS and SNR histograms for OdT: $f = 868\,\text{MHz}$, BW $= 125\,\text{kHz}$, SF $= 10$, CR $= 4/6$, LOS over land, $316\,\text{km}$.

warning systems for the detection of different natural disasters such as landslides, volcano eruptions, etc.

Furthermore, each experimental scenario also confirmed the advanced characteristics of the new LoRa transceiver in terms of sensitivity and immunity to external interferences. This is very important since it proves that hardware design is also appropriate to be deployed in development of the devices that could be potentially used in commercial applications offering improved characteristics in terms of two most important parameters of any wireless transceiver, namely sensitivity, and immunity to external interferences.

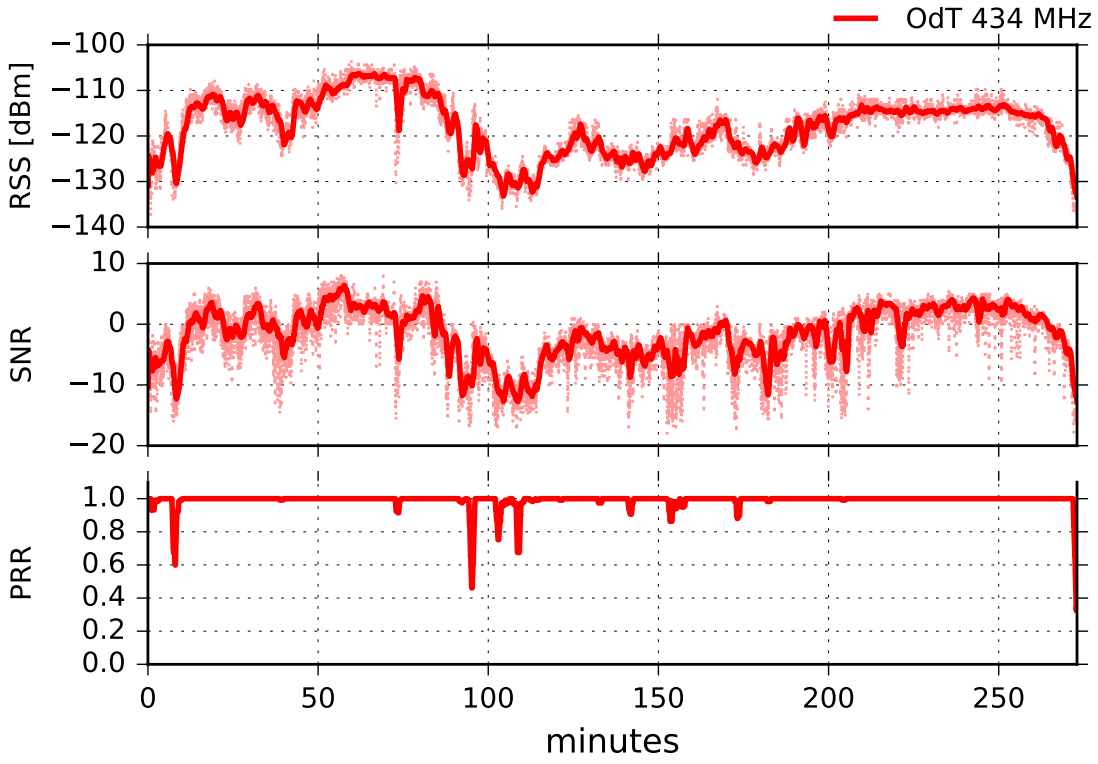

Figure 5.22: RSS, SNR, and PRR for 316 km LOS link over land for OdT at 434 MHz. LoRa test parameters: BW = 125 kHz, SF = 10, CR = 4/6.

5.5.2 LOS Over Seawater Experimental Scenario

This group of experiments aimed to investigate LoRa link feasibility over seawater in two frequency bands: 868 MHz and 434 MHz. The OdT transmitters at 868 MHz and 434 MHz were mounted at point A (ICTP), while the receivers (OdT and commercial transceivers) were mounted at point C (Pacug). Various sets of LoRa parameters were investigated - we probed SF $\in \{7, 10, 12\}$ within a fixed bandwidth of BW = 125 kHz, and coding rate CR = 4/6.

22 km LOS over seawater results at 868 MHz

Figure 5.24 shows the results obtained in LOS scenario for OdT, Libelium and Uputronics transceivers, operating at 868 MHz with following parameters: BW = 125 kHz, SF = 7, and CR = 4/6.

We observe that the RSS is almost constant during the whole experiment and that it is nearly equal for all three transceivers. This implies that multipath propaga-

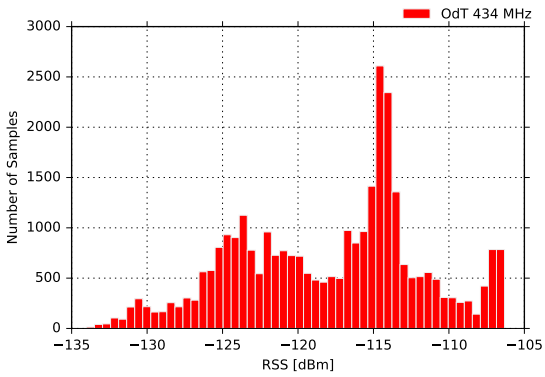

(a) RSS: 1-minute window moving average

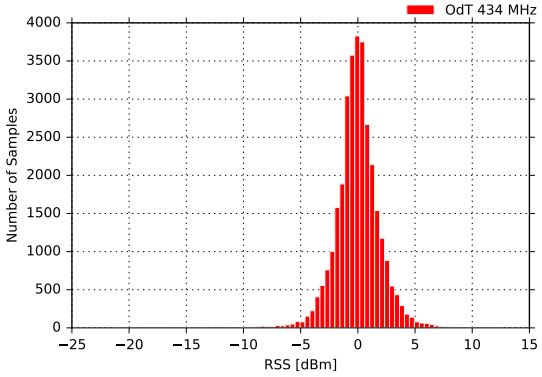

(b) RSS: 1-min window m. avg. fluctuations

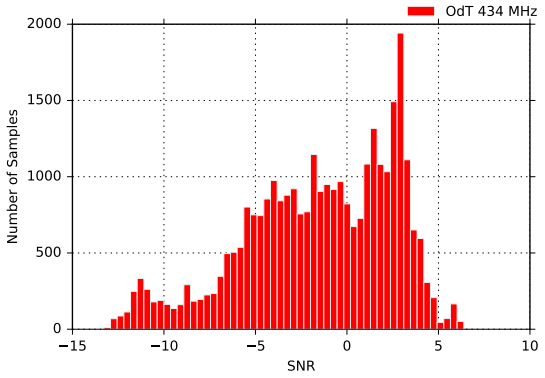

(c) SNR: 1-minute window moving average

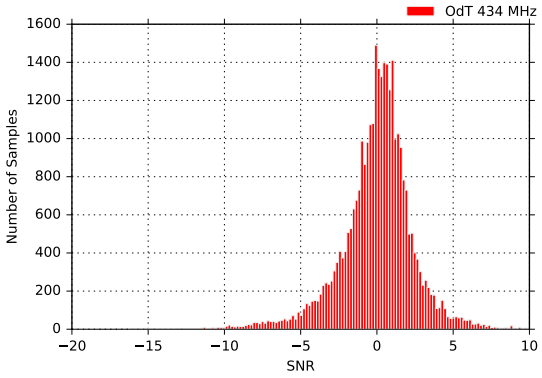

(d) SNR: 1-min window m. avg. fluctuations

Figure 5.23: RSS and SNR histograms for OdT: $f = 434\,\text{MHz}$, BW $= 125\,\text{kHz}$, SF $= 10$, CR $= 4/6$, LOS over land, 316 km.

tion effects were not dominant during the experiment and that the main component of the transmitted signal was the one which traveled in direct LOS path. In addition, two short dips can be seen in 58 and 78 minute of the test. They are caused by short radio-interference bursts, but they did not produce a drop in the packet reception rate. On the other hand, the SNR follows the fluctuation trend of RSS for all three transceivers. By inspecting the SNR values of different transceivers, and rescaling Libelium SNR values using Fig. 4.9, we observe that OdT has the highest SNR, and consequently the lowest noise floor; this implies the highest sensitivity of the OdT transceiver.

The PRR for OdT and Uputronics is constantly high, with negligible packet loss; Libelium has a constant packet loss, yielding PL $= 28.68\,\%$ which is high and unexpected since the values of RSS and SNR are deeply inside the link margin and

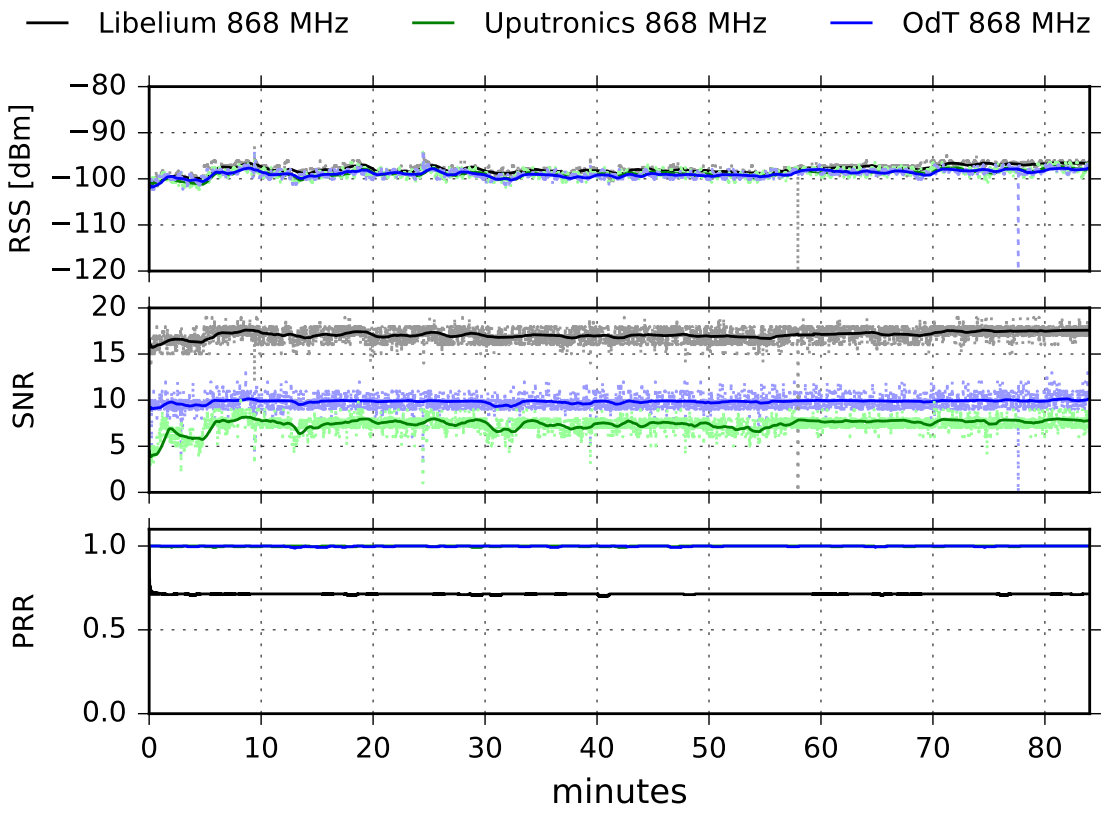

Figure 5.24: RSS, SNR, and PRR for 22 km LOS link over seawater for OdT, LiT, and UpT at 868 MHz. LoRa test parameters: BW = 125 kHz, SF = 7, CR = 4/6.

there is negligible interference. Additional tests are required in order to investigate the cause of the high packet loss.

Figure 5.25 shows RSS and SNR cumulative results on the entire measurement interval for the OdT, Uputronics and Libelium transceivers at 868 MHz, for the same LoRa parameters. It can be noticed that the distribution of RSS values does not indicate multipath propagation effects and fading since Rice distribution cannot be observed. Rice distribution of RSS amplitudes is characteristic when there is a multipath propagation effect in the channel and one component is dominant, usually, the one that travels in LOS path [89]. However, the distribution of the RSS amplitudes has to be interpreted cautiously since the RSS indicator measures the received power of the whole packet and cannot measure the RSS value of a single multipath component. The difference between the 1-minute window moving average values and current values exhibits the Gaussian distribution. This indicates that the time window for moving average calculations has been adequately selected since that

difference represent the RSS fluctuations, which can be treated as a kind of "noise".

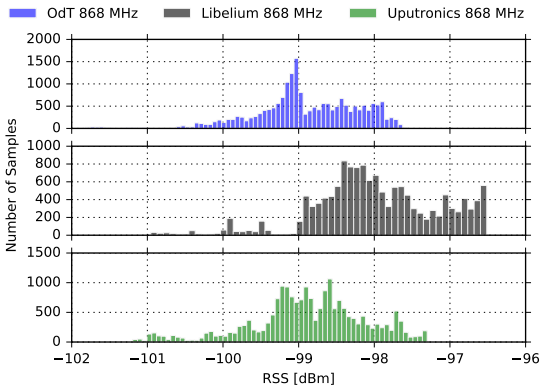

(a) RSS: 1-minute window moving average

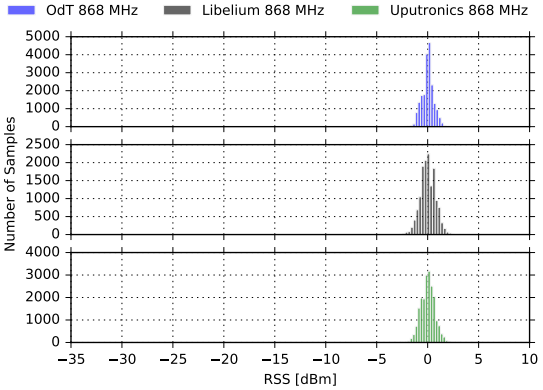

(b) RSS: 1-min window m. avg. fluctuations

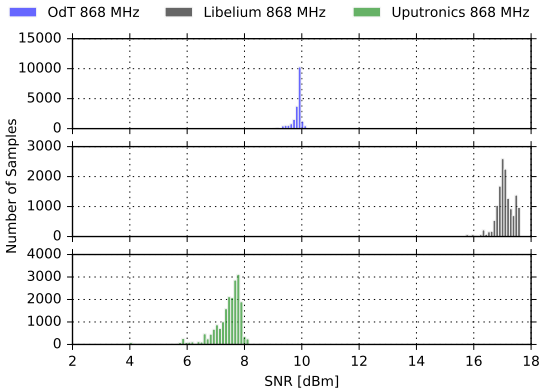

(c) SNR: 1-minute window moving average

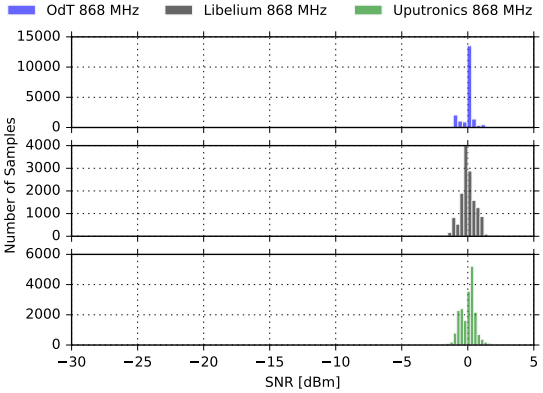

(d) SNR: 1-min window m. avg. fluctuations

Figure 5.25: RSS and SNR histograms for OdT, Uputronics, and Libelium: $f = 868\,\text{MHz}$, $\text{BW} = 125\,\text{kHz}$, $\text{SF} = 7$, $\text{CR} = 4/6$, LOS over seawater, 22 km.

Figure 5.26 shows results for the OdT, Uputronics, and Libelium transceiver at 868 MHz, in LOS scenario, with the following parameters: $\text{BW} = 125\,\text{kHz}$, $\text{SF} = 10$, $\text{CR} = 4/6$. It can be noticed that in this experiment RSS of all three transceivers fluctuated. Since these fluctuations are relatively slow, they can be attributed to multipath propagation effects. In the first 70 minutes of the experiment, multipath was not pronounced, however between 70 and 140 minute of the experiment, fluctuations of 5 dB are recorded. Since the experiment was carried out for LOS path (60 % of the First Fresnel zone was clear), multipath was a consequence of meteorological conditions which could cause refraction and consequently reflection from the sea surface due to forming air masses with different refraction indexes. How-

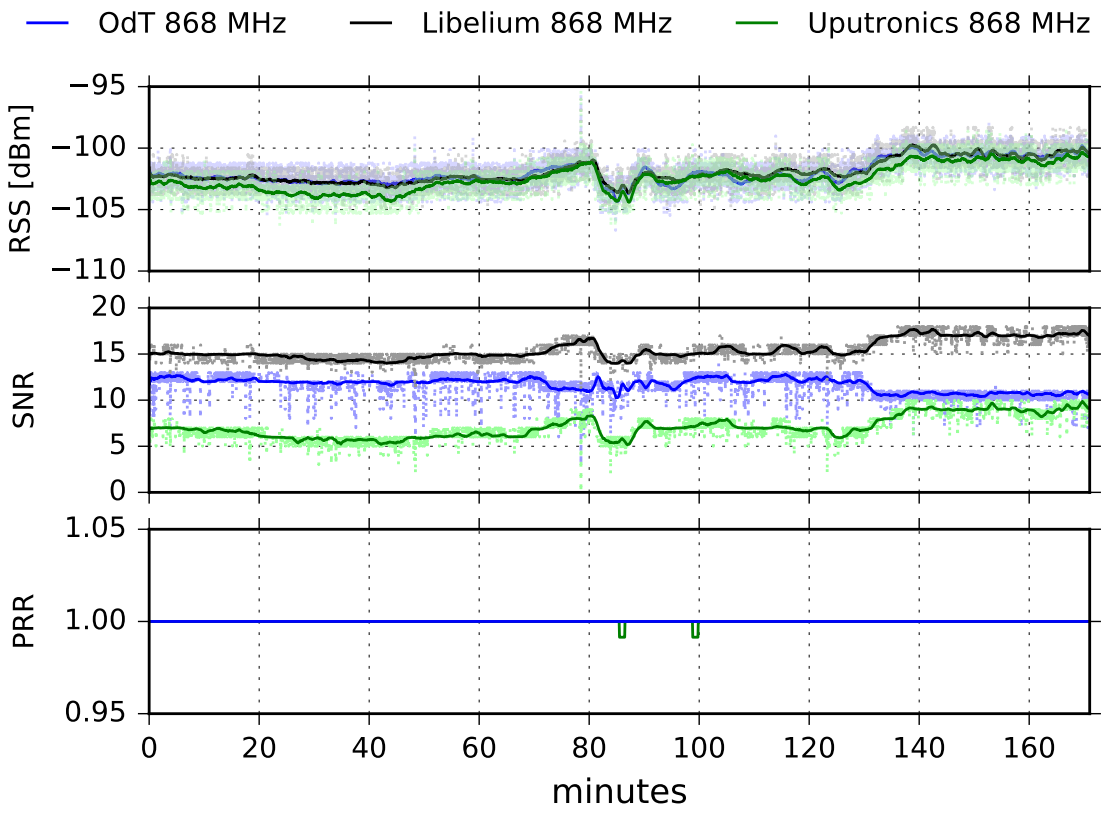

Figure 5.26: RSS, SNR, and PRR for 22 km LOS link over seawater for OdT, LiT, and UpT at 868 MHz. LoRa test parameters: BW = 125 kHz, SF = 10, CR = 4/6.

ever, the multipath did not cause any significant packet loss, Uputronics experienced negligible packet loss of PL = 0.01%.

We also observe that SNR recorded by Libelium and Uputronics follows the fluctuation trend of corresponding RSS values. On the other hand, the OdT exhibits counterintuitive behavior after 130 minute of the experiment since with the increase of the signal level at the input, SNR decreases. Examining Fig. 4.9 and taking into account the tolerances of components, this can be explained by saturated SNR measurement chain, which shows the "saw-tooth" oscillating behavior for the input signal levels higher than −100 dBm.

Figure 5.27 represents RSS and SNR histograms, based on the distribution of 1-minute window moving average values and differences between moving average values and current values for the same LoRa parameters. The distribution of the RSS amplitudes is obviously not Ricean, but it is expected since multipath propagation effect was present during only one interval of the experiment. Again, this

has to be interpreted cautiously due to already mentioned reasons. The distribution of the difference between the 1-minute window moving average values and current values can be approximated with Gaussian only in the SNR case, while for RSS bimodal distribution is observed. This can be explained with the presence of relatively pronounced multipath effects during one period of the experiment; however, further measurements are needed that would relate RSS bimodal distribution with multipath effects present in a limited interval within the experiment.

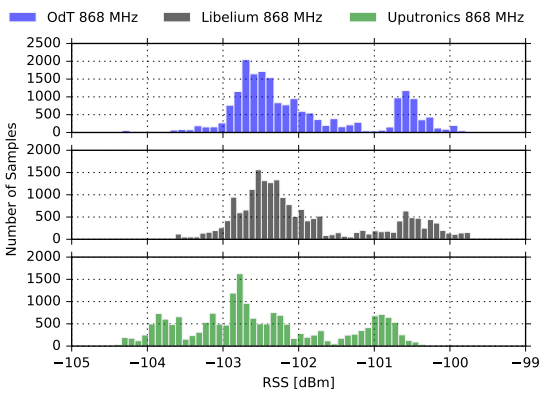

(a) RSS: 1-minute window moving average

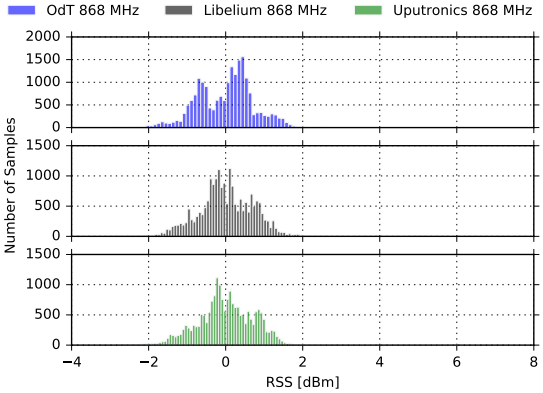

(b) RSS: 1-min window m. avg. fluctuations

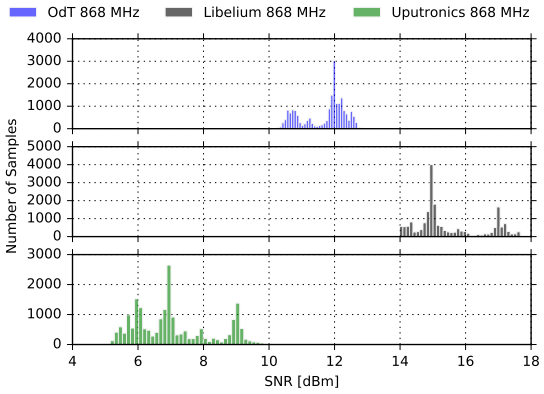

(c) SNR: 1-minute window moving average

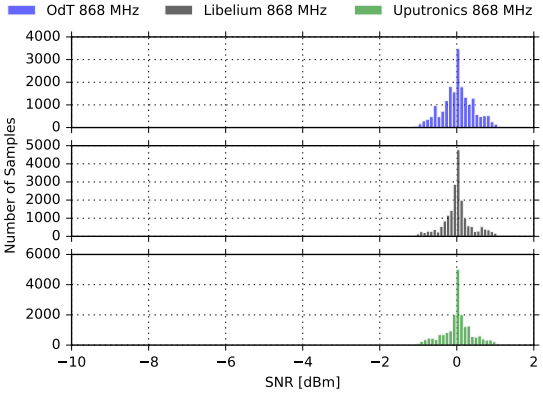

(d) SNR: 1-min window m. avg. fluctuations

Figure 5.27: RSS and SNR histograms for OdT, Uputronics, and Libelium: $f = 868\,\text{MHz}$, $\text{BW} = 125\,\text{kHz}$, $\text{SF} = 10$, $\text{CR} = 4/6$, LOS over seawater, 22 km.

In Fig. 5.28 results for $\text{BW} = 125\,\text{kHz}$, $\text{SF} = 12$, and $\text{CR} = 4/6$ are given. The small fluctuations of RSS for all three transceivers, approximately 2 dB peak-to-peak, indicate that there was an unobtrusive multipath propagation, whose effects were not detrimental for PRR. On the other hand, sporadic packet loss that Libelium

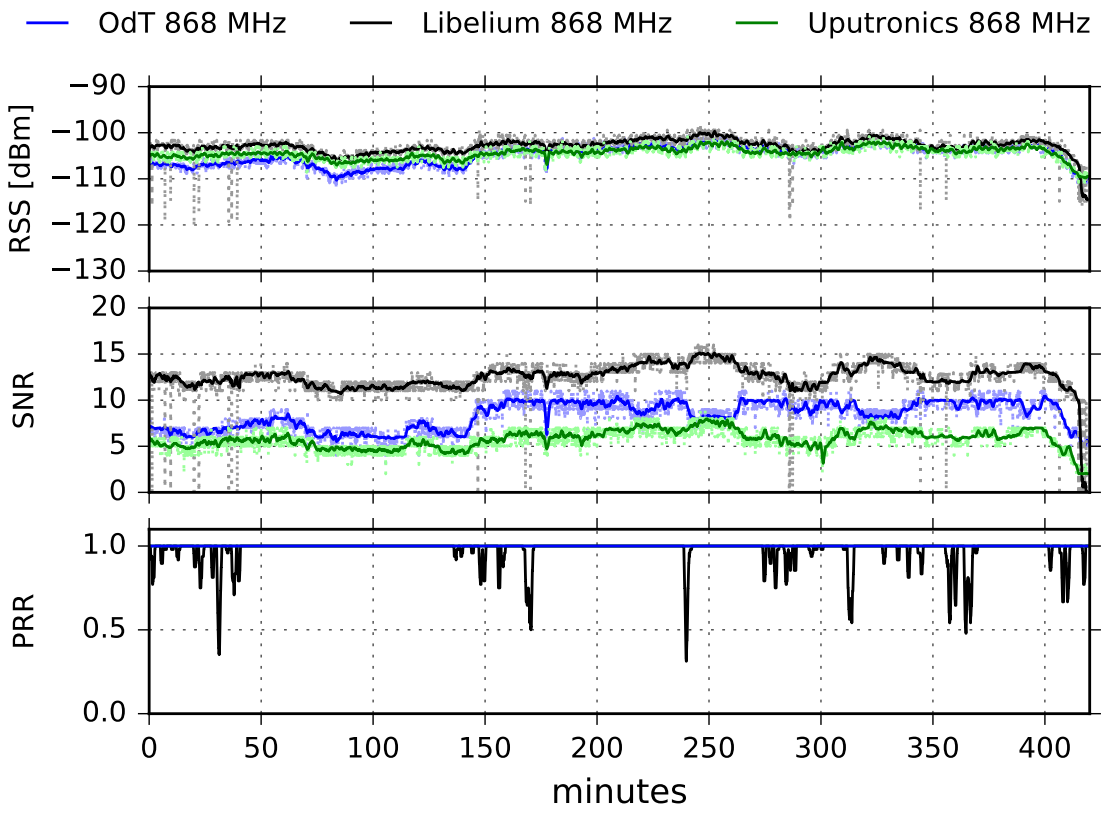

Figure 5.28: RSS, SNR, and PRR for 22 km LOS link over seawater for OdT, LiT, and UpT at 868 MHz. LoRa test parameters: BW = 125 kHz, SF = 12, CR = 4/6.

experienced is a consequence of short burst radio-interference, as can be seen on the plots. This claim is also additionally supported by the fact that moving averages of the RSS and SNR are significantly higher than the link margin during the whole measurement interval. We also observe that SNR follows RSS fluctuation trend for all three transceivers for most of the time, except for OdT: around the 250 and 325 minute of the experiment we again notice that SNR decreases when RSS increases; a closer look reveals that RSS again reached −100 dBm, replicating the same effects as in the previous experiment. Finally, by comparing the SNRs, it can be again noticed that OdT has the lowest noise floor and, consequently, the highest sensitivity.

The histograms for the same experiment scenario, presented in Fig. 5.29 confirms the reasoning applied in the previous experiments. Due to small-scale effects of multipath propagation, the distribution of the differences between RSS moving average values and current values is not bimodal; however, this has to be additionally confirmed with further experiments to be able to be generalized.

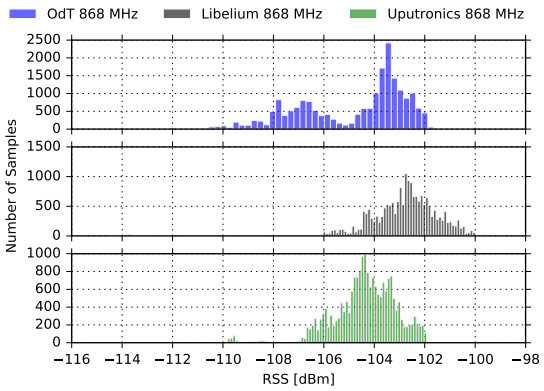

(a) RSS: 1-minute window moving average

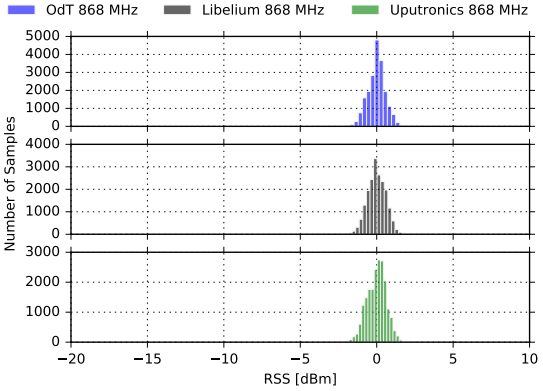

(b) RSS: 1-min window m. avg. fluctuations

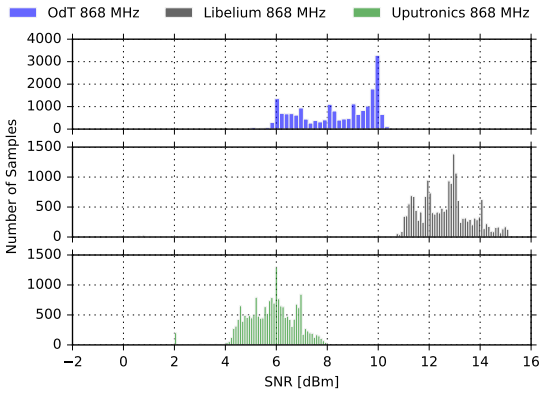

(c) SNR: 1-minute window moving average

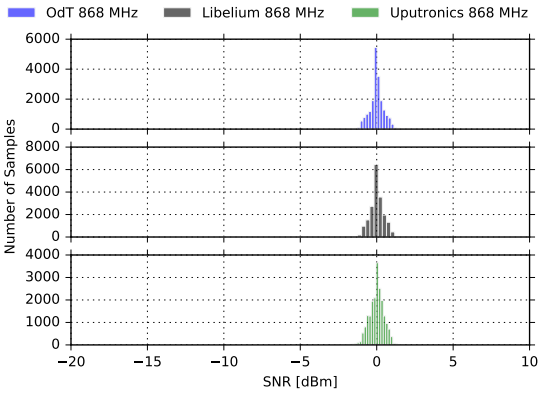

(d) SNR: 1-min window m. avg. fluctuations

Figure 5.29: RSS and SNR histograms for OdT, Uputronics, and Libelium: $f = 868\,\text{MHz}$, $\text{BW} = 125\,\text{kHz}$, $\text{SF} = 12$, $\text{CR} = 4/6$, LOS over seawater, 22 km.

22 km LOS over seawater results at 434 MHz

The experiments carried out at 434 MHz were performed using a pair of OdT transceivers, exploring the same LoRa parameters as in the case for 868 MHz band. In addition, the experimental setup was identical and deployed to operate simultaneously with the 868 MHz setup.

Figure 5.30 shows results for the following parameters: $\text{BW} = 125\,\text{kHz}$, $\text{SF} = 7$, and $\text{CR} = 4/6$. It can be seen that the RSS is remarkably high during the whole measurement, the minimum value is $-88\,\text{dBm}$. Its moving average values fluctuate 3 dB peak-to-peak indicating a small-scale multipath propagation. This also can be concluded if we compare it to the corresponding results at the 868 MHz. Namely, the difference yields approximately 12 dB. However, due to negligible terrain shielding

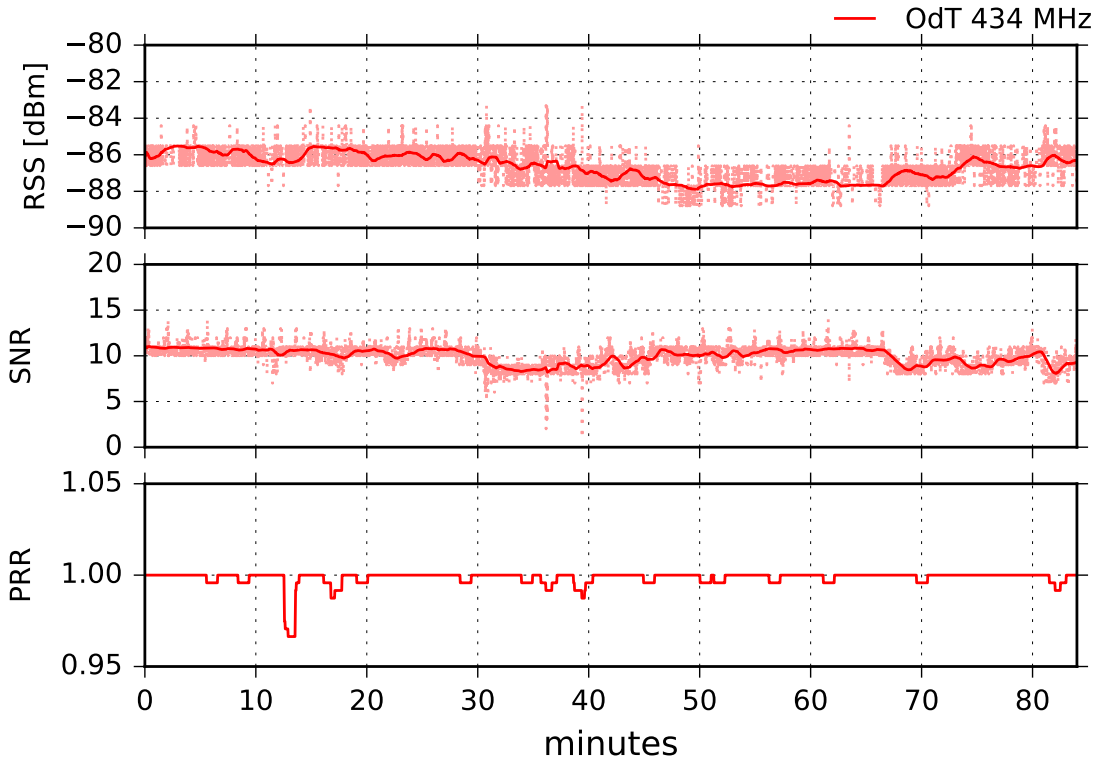

Figure 5.30: RSS, SNR, and PRR for 22 km LOS link over seawater for OdT at 434 MHz. LoRa test parameters: BW = 125 kHz, SF = 7, CR = 4/6.

in this case (see Table 5.2) and consequent free-space propagation, the difference should be 6 dB, provided there are no multipath effects on propagation path. We can also observe a very small packet loss during the whole experiment which yields PL = 0.15 %.

The SNR fluctuations do not follow RSS fluctuation trend during the whole experiment. Referring to Fig. 4.9, this can be easily explained. Namely, the SNR measurement chain is deeply in the saturation region, reflecting the oscillations that can be observed for RSS values lower than −100 dBm.

Figure 5.31 shows the distribution of the moving averages of the RSS and SNR calculated in the 1-minute window, as well as distributions of the difference between their current and moving average values. The results shown are obtained using the following LoRa parameters: BW = 125 kHz, SF = 7, and CR = 4/6. We observe that difference between current and moving average values of RSS is nearly bimodal which is expected since small-to-medium-scale multipath effects can be observed.

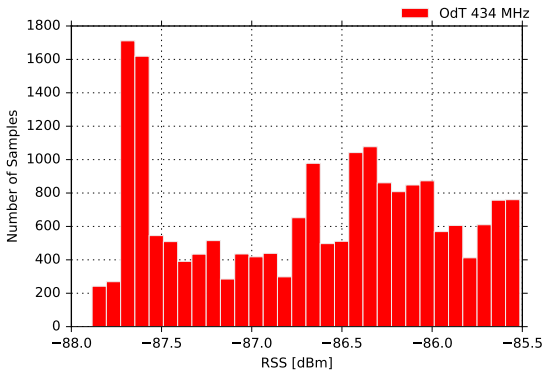

(a) RSS: 1-minute window moving average

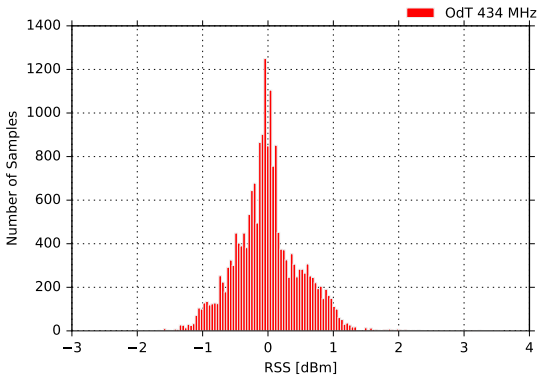

(b) RSS: 1-min window m. avg. fluctuations

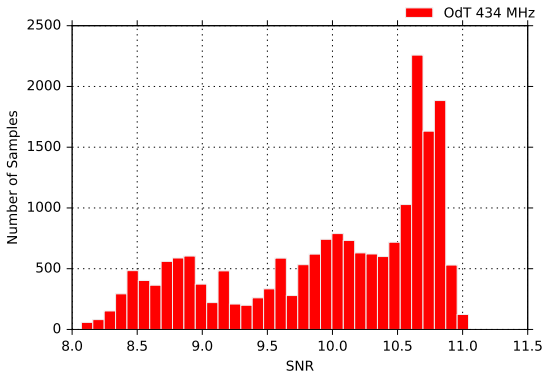

(c) SNR: 1-minute window moving average

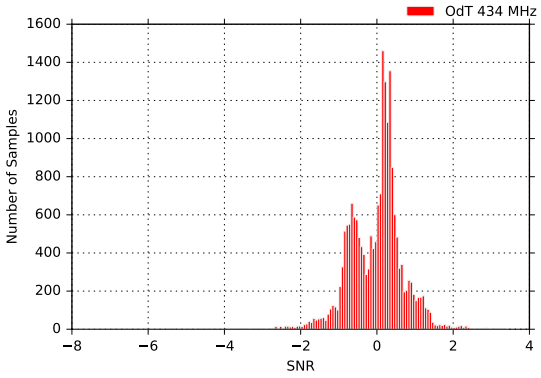

(d) SNR: 1-min window m. avg. fluctuations

Figure 5.31: RSS and SNR histograms for OdT: $f = 434\,\text{MHz}$, BW $= 125\,\text{kHz}$, SF $= 7$, CR $= 4/6$, LOS over seawater, 22 km.

On the other hand, it can be noticed that for the same difference of SNR values there is a bimodal distribution, which may be explained by the deep saturation of the SNR measurement chain; however, this claim needs further investigation in order to be confirmed.

In Fig. 5.32 results for the following LoRa parameters are given: BW $= 125\,\text{kHz}$, SF $= 10$, and CR $= 4/6$. As in the previous experimental case, RSS fluctuation of moving average values are approximately 3 dB peak-to-peak. The difference between the corresponding RSS values for the same LoRa parameters at 868 MHz is slightly lower yielding 10 dB. The same conclusion as in the case for SF $= 7$ can be applied; this is also valid for SNR.

Figure 5.33 shows RSS and SNR distribution of 1-minute moving average and the difference between current values and moving average for the same LoRa param-

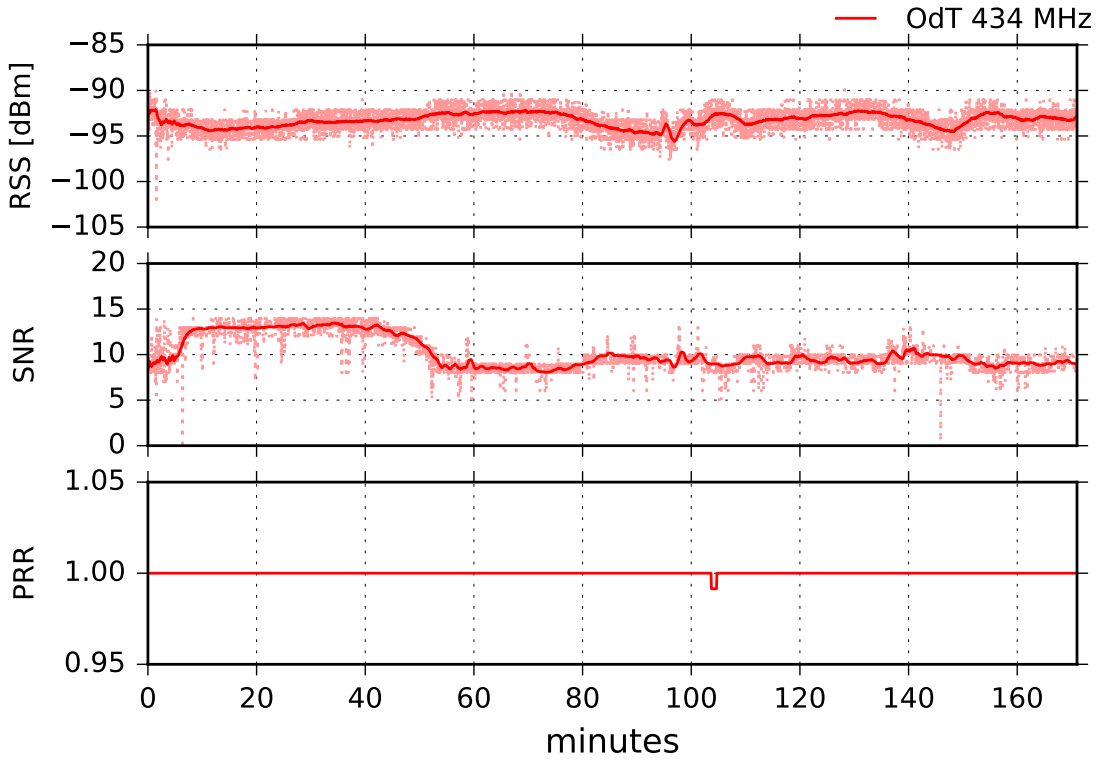

Figure 5.32: RSS, SNR, and PRR for 22 km LOS link over seawater for OdT at 434 MHz. LoRa test parameters: BW = 125 kHz, SF = 10, CR = 4/6.

eters. Again, the small-scale multipath effects can be distinguished by inspecting the difference between current values and moving average values in Fig. 5.33b. On the other hand, the moving average fluctuations in Fig. 5.33d this time show Gaussian distribution, but the SNR measurement chain is on the onset of the saturation region, where the characteristic of the measurement chain is different than in the deep saturation region.

Figure 5.34 shows experimental results for the following parameters: BW = 125 kHz, SF = 12, and CR = 4/6. The RSS fluctuations in this mode are the highest, and multipath propagation is clearly observed. However, PRR is constantly PRR = 1, which is expected due to highest sensitivity mode of operation. It should be noted that, counter-intuitively, these LoRa settings can also yield the highest packet loss due to very long packet airtime (above 1 second) and increased susceptibility to interference. The uncorrelated fluctuations of SNR to RSS are due to same reasons as in the other two experimental scenarios for 434 MHz - the saturation of SNR

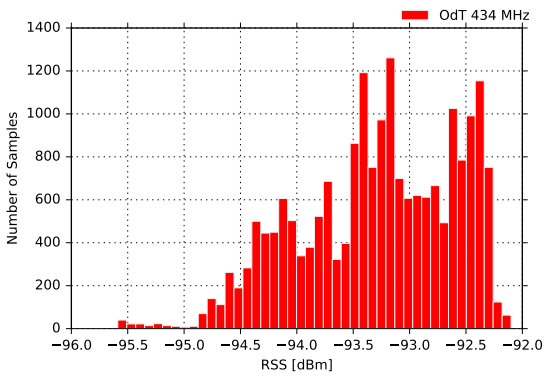

(a) RSS: 1-minute window moving average

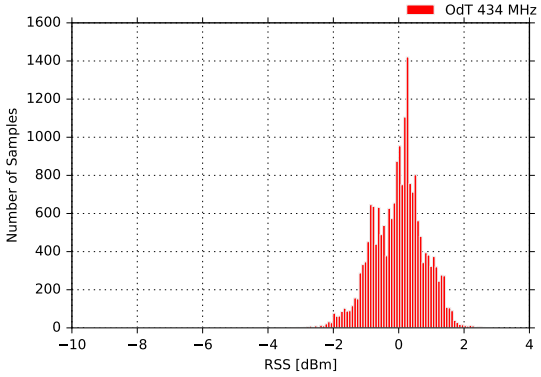

(b) RSS: 1-min window m. avg. fluctuations

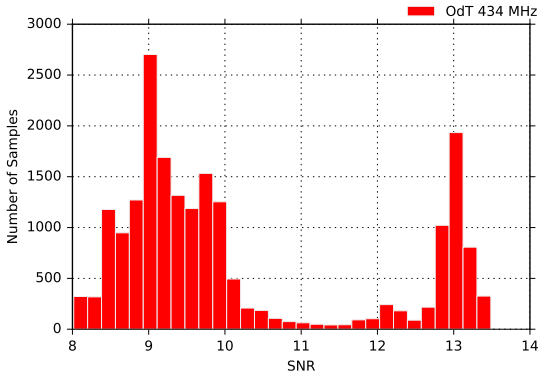

(c) SNR: 1-minute window moving average

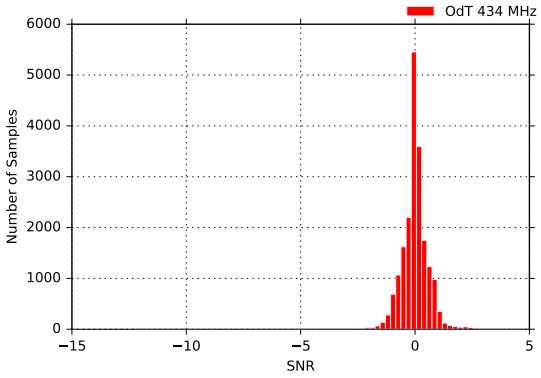

(d) SNR: 1-min window m. avg. fluctuations

Figure 5.33: RSS and SNR histograms for OdT: $f = 434\,\text{MHz}$, BW $= 125\,\text{kHz}$, SF $= 10$, CR $= 4/6$, LOS over seawater, 22 km.

measurement chain and oscillation which the chain exhibits in that region.

Eventually, Fig. 5.35 gives an insight into the distribution of the RSS and SNR moving averaged values, calculated on the 1-minute window for the same measurement. Here the same conclusions from the previous experimental case can be applied.

The experimental results unambiguously show that LoRa links over seawater are feasible up to at least 22 km for any combination of LoRa parameters in both frequency bands of interest, 868 MHz and 434 MHz if LOS condition between transmitter and receiver is guaranteed. Furthermore, the links are feasible using low-cost off-the-shelf rubber duck antennas which makes the results useful also in commercial deployments. Since there is a link margin of 15 dB in 868 MHz band, and approximately 20 dB in 434 MHz band, it can be assumed that maximum achievable distance is significantly longer.

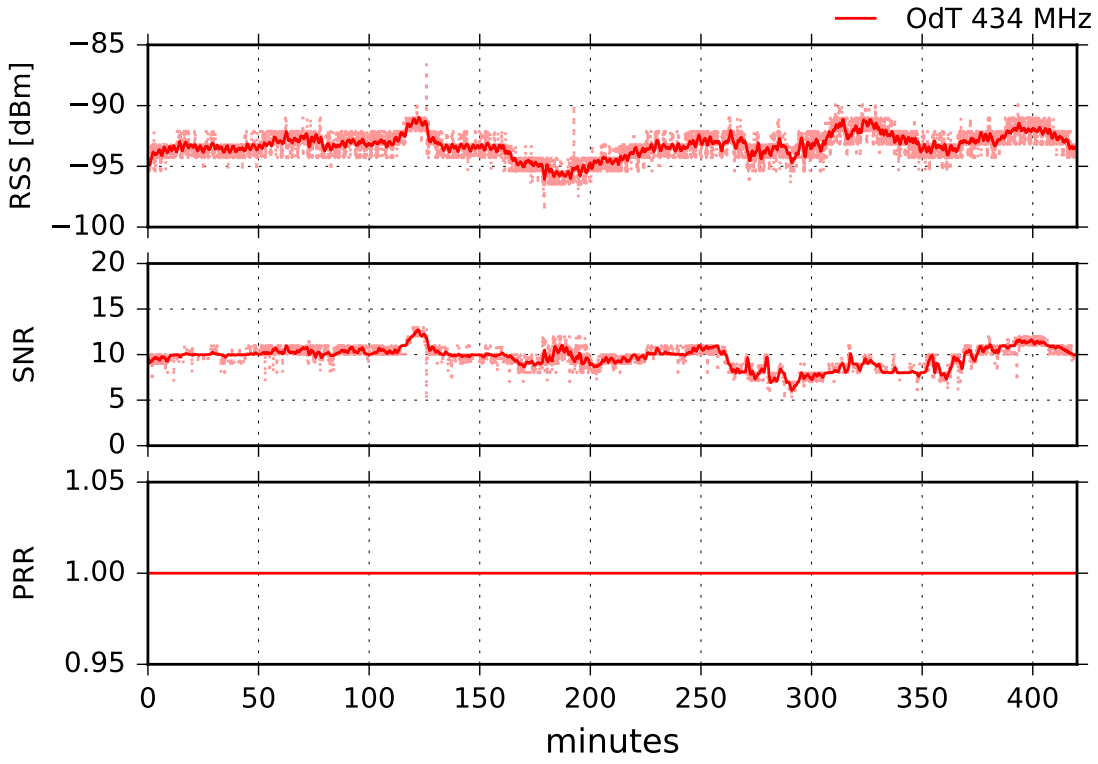

Figure 5.34: RSS, SNR, and PRR for 22 km LOS link over seawater for OdT at 434 MHz. LoRa test parameters: BW = 125 kHz, SF = 12, CR = 4/6.

Moreover, the experiments also showed that there is a significant weather tolerance margin as well. Namely, it is well known that RSS decreases when ambient temperature increases [90]. This can impair signal reception if deployments are done in areas with high average temperature fluctuations during the year. Moreover, if the transceivers are mounted inside, e.g. IP-67 rated enclosure, the temperature can be even higher than ambient if the device is exposed directly to the sun [91]. Since our transceivers were deployed in unfavorable conditions in terms of weather conditions (they were mounted inside the IP-67 rated enclosure, directly exposed to the sun, with an ambient temperature of 28 °C), it can be easily concluded that link feasibility can be extended for even higher ambient temperatures.

It is interesting to note that RSS fluctuations are smaller for a smaller spreading factor used. By increasing the spreading factor, the RSS fluctuations are increasing in amplitude in both frequency bands, resulting in a peak-to-peak value of 10 dB for SF = 12 at 868 MHz. Additional investigation is needed to determine the cause,

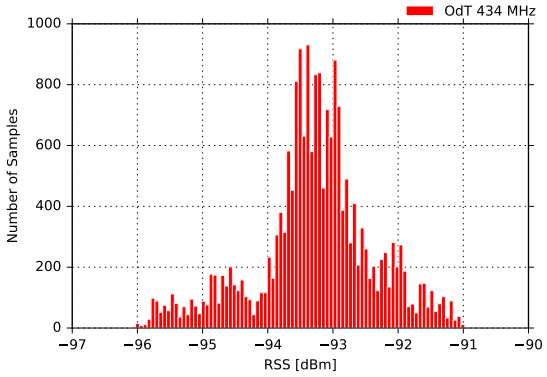

(a) RSS: 1-minute window moving average

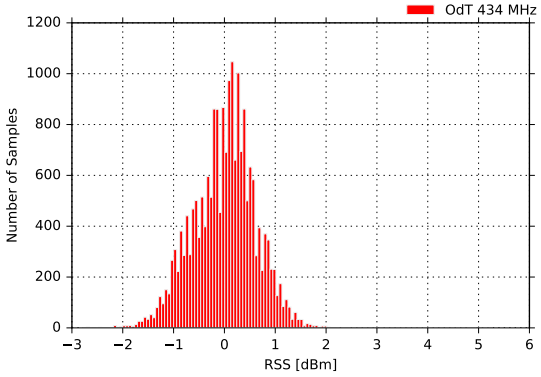

(b) RSS: 1-min window m. avg. fluctuations

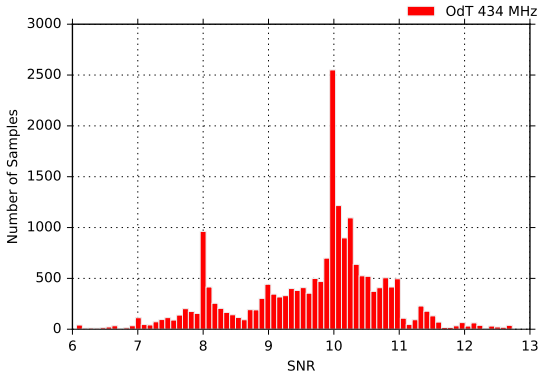

(c) SNR: 1-minute window moving average

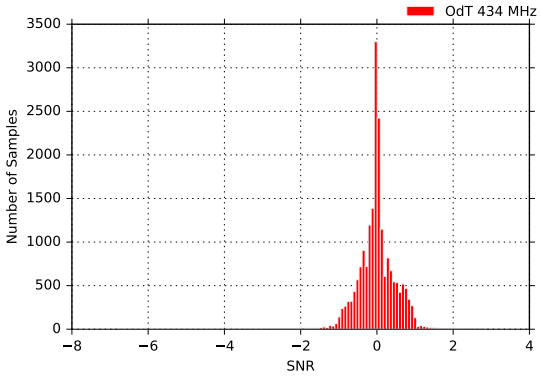

(d) SNR: 1-min window m. avg. fluctuations

Figure 5.35: RSS and SNR histograms for OdT: $f = 434\,\text{MHz}$, BW $= 125\,\text{kHz}$, SF $= 12$, CR $= 4/6$, LOS over seawater, 22 km.

however, an explanation can be related to longer packet airtimes (due to higher SFs) and longer RSS measurement window which increases the probability for a different kind of interference to impact the measurement. Nevertheless, this did not cause a problem in the packet reception rate because the absolute value of RSS was substantially greater than the reception margin for the given LoRa parameters.

When the SNR measurement chains are not in the saturation region of operation, the values of SNR can be used to assess the link quality. It can be seen that OdT transceiver constantly has the highest SNR, as well as the highest PRR. This is the consequence of the lowest noise floor which is provided with an advanced hardware design approach described in [80]. This enables the OdT to decode very weak signals and maximize range.

The PRR is constantly high with negligible packet loss for all LoRa parameters

tested, except for Libelium in the case of SF = 7. This needs further investigation since RSS and SNR are considerably above the reception margin, and the other two receivers operated flawlessly for the same LoRa parameters. Besides that, in all other experimental scenarios packet loss is negligible, which implies that LoRa parameters can be chosen only according to the application specific requirements.

It is worth noting that in these experiments compatibility between the only two manufacturers of LoRa ICs is validated since the transmitters were equipped with Semtech LoRa ICs, whereas one of the receivers was equipped with HopeRF LoRa IC. This practically means that there are no limitations in terms of hardware usage in different deployments.

Results of the experiments imply that propagation over seawater does not pose any problem for LoRa transmission systems. The optimum set of parameters can be chosen based only on the particular application requirements, since the reliable transmission can be achieved for virtually any combination of LoRa parameters for bandwidths BW $\geq$ 125 kHz. Taking into account LoRa bit rate, these systems may be very useful for connection of environmental monitoring stations deployed in island countries. Moreover, this technology could be applied in early-warning systems for disaster prevention from e.g. eruptions of volcanoes located on islands.

5.5.3 Obstructed LOS Over Seawater Scenario

This group of experiments aimed to give a deeper insight into LoRa links behavior over seawater when the LOS is completely blocked. The assumption was that propagation was possible due to diffraction effects on knife-edge obstacle. The obstacle consisted of natural rocks and was positioned near the receive side, see Fig 5.3.

28 km obstructed LOS over seawater results at 868 MHz

This group of experiments did not yield any results in terms of packet reception. We tested all three group of parameters; moreover, we replaced low cost COTS antennas by three-element collinear dipoles with a higher gain of 8.5 dBi, but we could not establish a link for any of the LoRa parameters used in the previous experiments.

28 km obstructed LOS over seawater results at 434 MHz

Using low-cost, off-the-shelf, rubber-duck antennas, we were unable to establish a LoRa link. Since we were on the boundary of the reception margin, we replaced the antenna on transmit side with wide-band three-element collinear dipole with a higher gain of 6.5 dBi. The results of the experiment were the same as previously: there was no reception for any of the LoRa parameters.

In the next step, we replaced the antenna at the receive side also with a collinear dipole. Since this case is not suitable for most IoT commercial applications, (costly and bulky antennas at both sides), we tested only one set of LoRa parameters: BW = 125 kHz, SF = 10, and CR = 4/6. In this case, we had a successful packet reception and the results are given in Fig. 5.36.

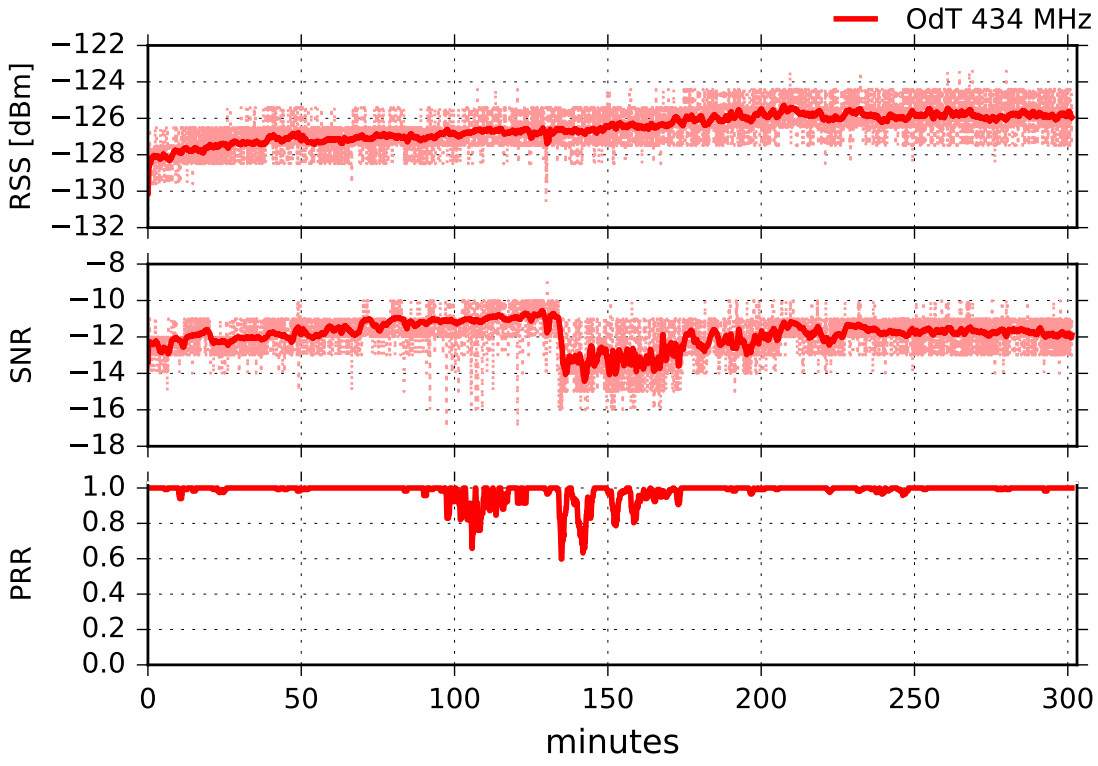

Figure 5.36: RSS, SNR, and PRR for 28 km obstructed LOS link over seawater for OdT at 434 MHz. LoRa test parameters: BW = 125 kHz, SF = 10, CR = 4/6.

Analyzing RSS, SNR, and PRR combined, it can be concluded that two different kinds of interferences affected transmission: 1) radio-interference, which caused main packet loss between 95 and 175 minute of the experiment; and 2) interference

due to multipath propagation which started after 140 minute of the experiment. Radio-interference can be recognized by short dips in SNR while moving average values remain high. In the interval $140 - 175$ minute of the experiment, both radio-interference and interference caused by the multipath propagation, affected transmission and PRR. This can be recognized due to short dips in SNR which reach link margin values, and by a drop in moving average values, respectively. Multipath propagation, in this case, could be caused by meteorological conditions and different refraction indexes of air masses between transmit and receive side, as well as by the diffraction on knife-edge obstacle, made of natural rocks, which blocks LOS propagation (see Fig. 5.3).

Figure 5.37 presents the distribution of RSS and SNR moving averages and the difference between moving average values and their current values.

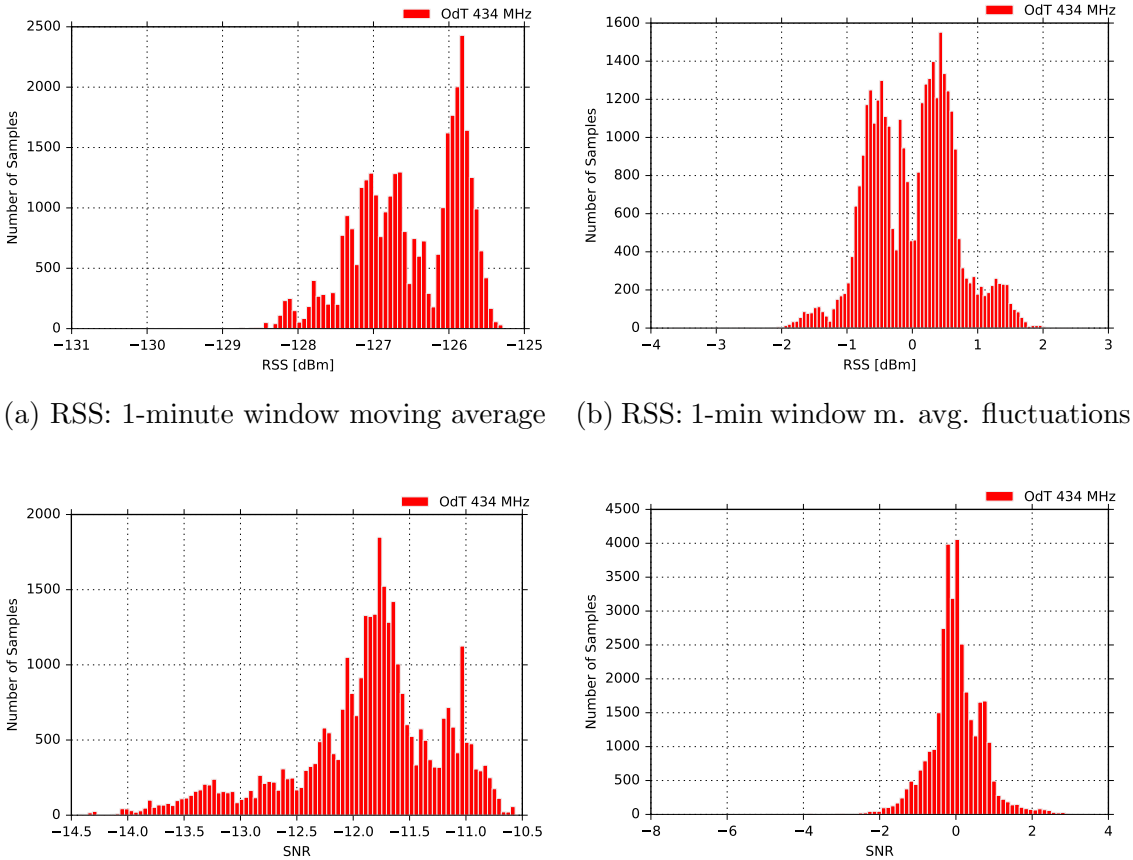

(a) RSS: 1-minute window moving average

(b) RSS: 1-min window m. avg. fluctuations

(c) SNR: 1-minute window moving average

(d) SNR: 1-min window m. avg. fluctuations

Figure 5.37: RSS and SNR histograms for OdT: $f = 434\,\text{MHz}$, $\text{BW} = 125\,\text{kHz}$, $\text{SF} = 10$, $\text{CR} = 4/6$, obstructed LOS over seawater, 28 km.

The results are similar to all other results obtained for 434 MHz band, except for the RSS fluctuations. Multimodal distribution (three modes) is observed in this case, which can indicate the presence of three intervals affected by different sources of interference combined; in order to confirm this claim, additional experiments are needed.

The experiment shows that LoRa links can be established even in the presence of an obstacle that blocks the line of sight, provided that higher gain antennas are used at both ends. In this case, the reception was attributed to diffraction in the knife edge obstacles present on the propagation path. Nevertheless, there are certain limitations when it comes to their practical implementations since costly and bulky antennas are needed on both sides and transmission reliability is not guaranteed.

5.5.4 Cumulative packet loss analysis

Cumulative packet loss analysis refers to analysis in which packet losses obtained in different experimental scenarios are analyzed together for the same sets of LoRa parameters. In this way, we were able to extrapolate LoRa system behavior in terms of packet loss for different parameters and ranges in LOS propagation scenario.

We used data sets obtained in two different experimental scenarios: LOS over seawater in 22 km long link, and LOS over land in 112 km long link. The results are obtained for two different frequencies of interest, namely 868 MHz and 434 MHz for the following LoRa parameters: SF $\in \{7, 10, 12\}$, BW = 125 kHz, and CR = 4/6.

The results are presented in the form of 3D plots; the x-axis represents the range, while the y-axis represents different spreading factors. Z-axis is cumulative packet loss obtained in different measurement scenarios. The plot colors are consistent with those used in previous subsections.

Figure 5.38 presents results obtained at 868 MHz using OdT transceiver. We observe that packet loss is increasing with range for all three spreading factors, as expected. On the other hand, counterintuitive, the highest gradient can be noticed for spreading factor SF = 10. This is unexpected since the lowest sensitivity of the RF IC is for SF = 7, and it is expected that the packet loss gradient is the highest in this case. However, the packet loss for this spreading factor reaches its

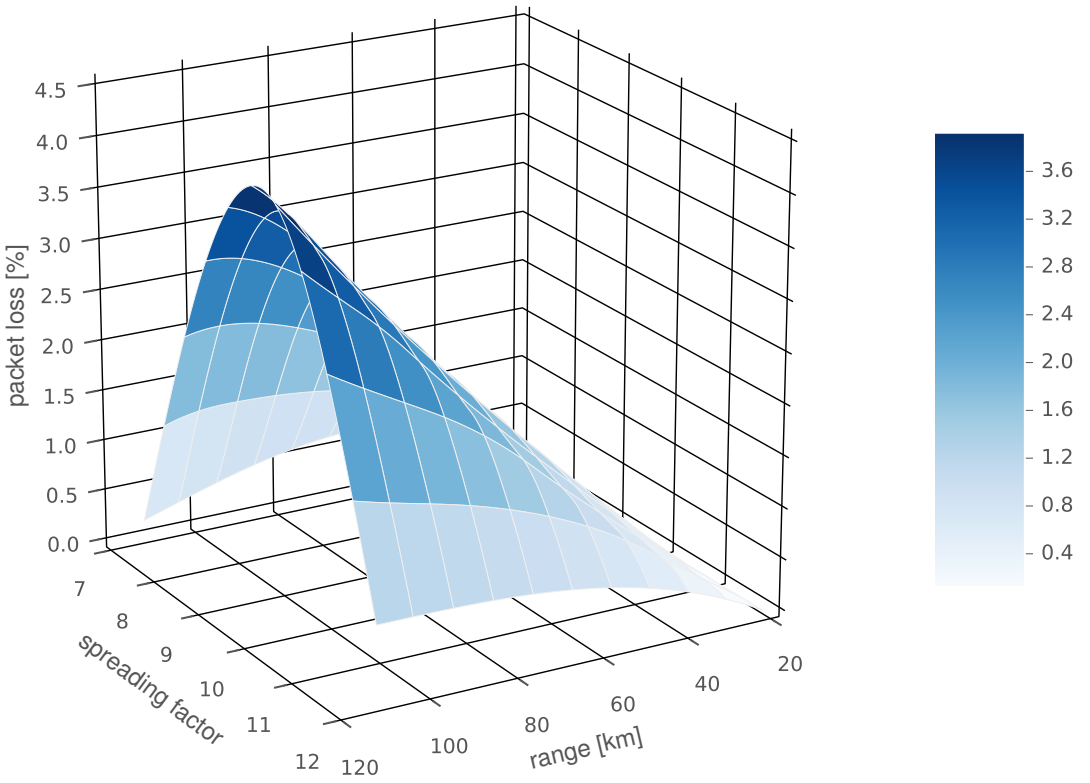

Figure 5.38: OdT cumulative packet loss at 868 MHz as a function of spreading factor and range.

maximum of PL = 0.14 %, whereas the packet loss for spreading factor SF = 10 is PL = 4.09 %. The packet loss for the spreading factor SF = 12 is smaller than for SF = 10, as expected, but still higher than for SF = 7, yielding PL = 0.73 %. This can be explained, as already stated, by longer packet airtime for higher spreading factors and increased probability for the background noise to couple to the receiver and impair packet reception. The analysis shows that the use of higher spreading factors does not necessarily imply lower packet loss. Nevertheless, the packet loss experienced in this group of experiments is small and simple to handle by using some communication protocol.

Figure 5.39 presents results acquired with LiT transceiver at 868 MHz. In this experimental scenario, packet losses are significantly higher than those recorded with OdT transceiver. Maximum packet loss is recorded for SF = 7 over 112 km long link,

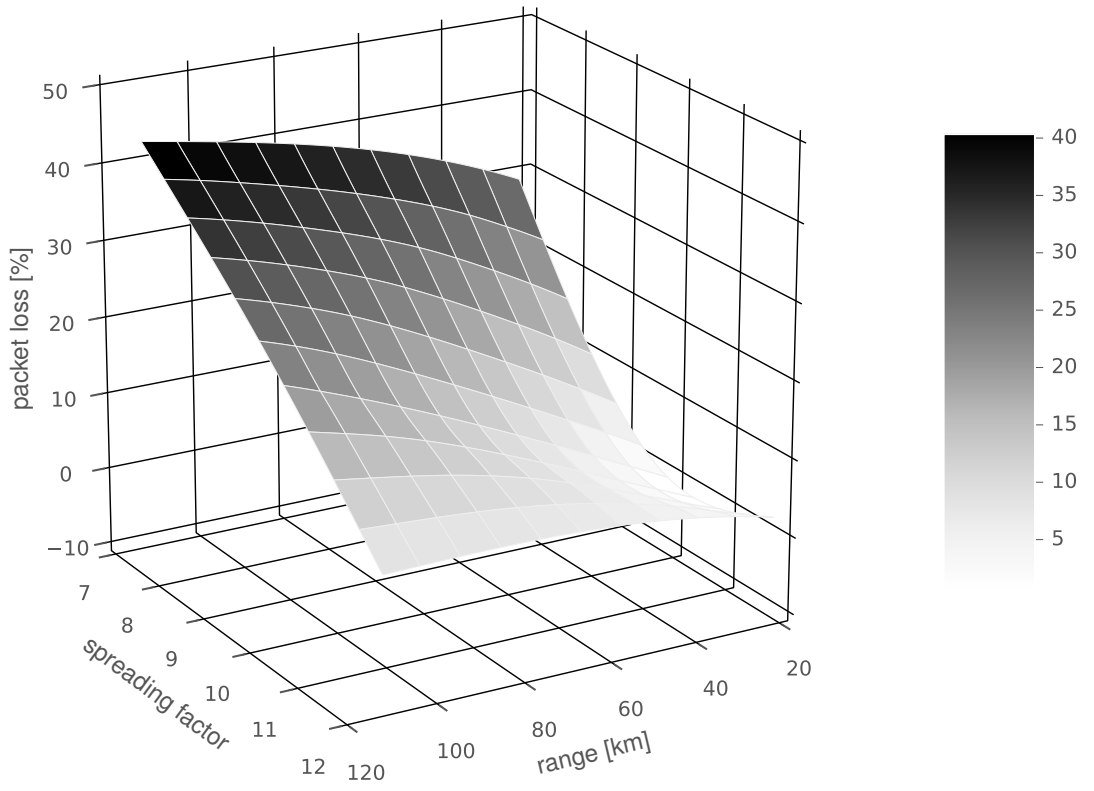

Figure 5.39: LiT cumulative packet loss at 868 MHz as a function of spreading factor and range.

which yields PL = 42.3 %. Such high packet loss proves the superior performance of OdT over LiT since OdT experienced PL = 0.14 % in the same experimental conditions.

Packet loss recorded for SF = 10 reaches its maximum at distance of 112 km. This is as expected, and it is lower than for the SF = 7, yielding PL = 22.39 %. However, this is still very high packet loss in comparison with OdT transceiver, which under the same experimental conditions recorded PL = 4.09 %. Finally, for SF = 12 the LiT transceiver experienced the smallest packet loss at link distance of 112 km, which is PL = 6.53 %.

It is interesting to note that for the 22 km long link, the smallest packet loss was recorded for SF = 10. In this experimental scenario packet airtime duration affected packet reception only in LOS over seawater experimental scenario. On the

other hand, as expected, the smallest gradient of packet loss increase was recorded for SF = 12.

Figure 5.40 shows data recorded with UpT transceiver at 868 MHz. As can be seen, the packet loss exhibits the similar trend as that recorded by OdT. Identically, maximum packet loss is experienced for SF = 10, which is PL = 19.1 %. On the other hand, the smallest change in the packet loss was recorded for SF = 12 since the minimum value is PL = 0.01 %, while maximum value is PL = 0.88 %.

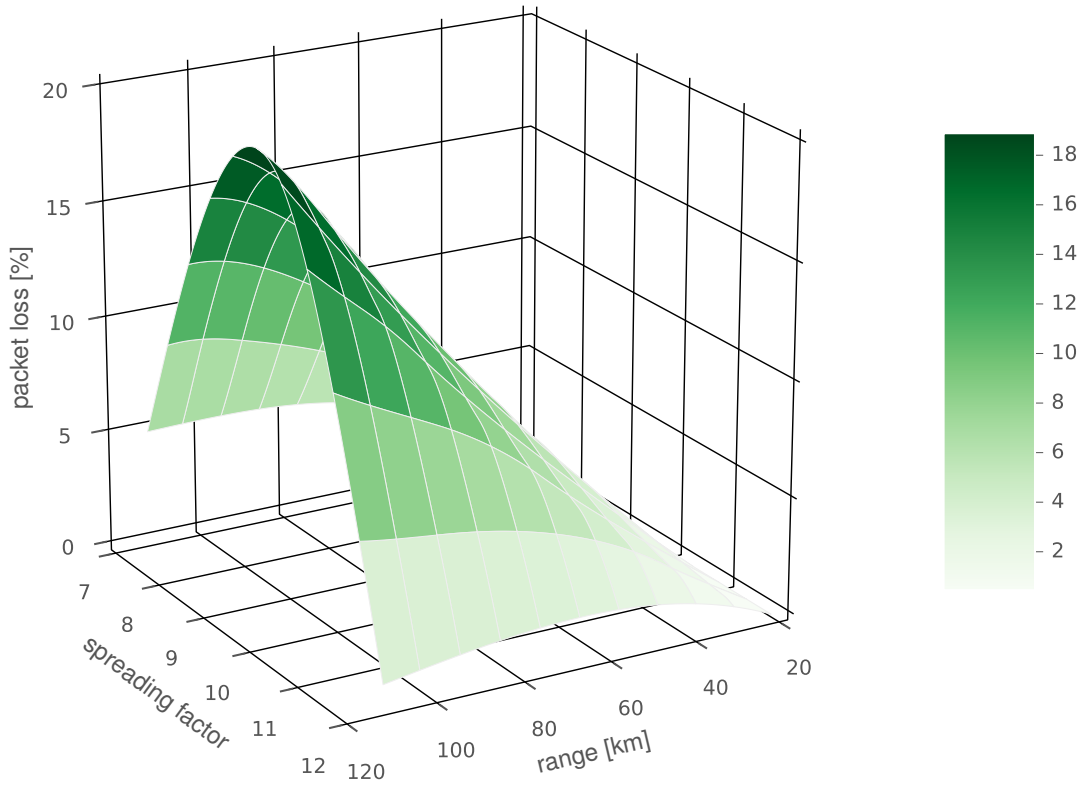

Figure 5.40: UpT cumulative packet loss at 868 MHz as a function of spreading factor and range.

Finally, in Figure 5.41 results acquired for OdT transceiver at 434 MHz are presented. We observe that packet loss exhibits the same trends as LiT transceiver, but with significantly smaller packet losses recorded. Expectedly, the highest packet loss in the experiment was recorded using SF = 7, yielding PL = 6.02 %. On the other hand, packet loss obtained deploying SF = 12 was almost constant for all link

lengths. This is expected since path loss at 434 MHz is lower than for 868 MHz, and it cannot affect packet reception rate for these LoRa parameters significantly since the link margin is still high even for the link length of 112 km.

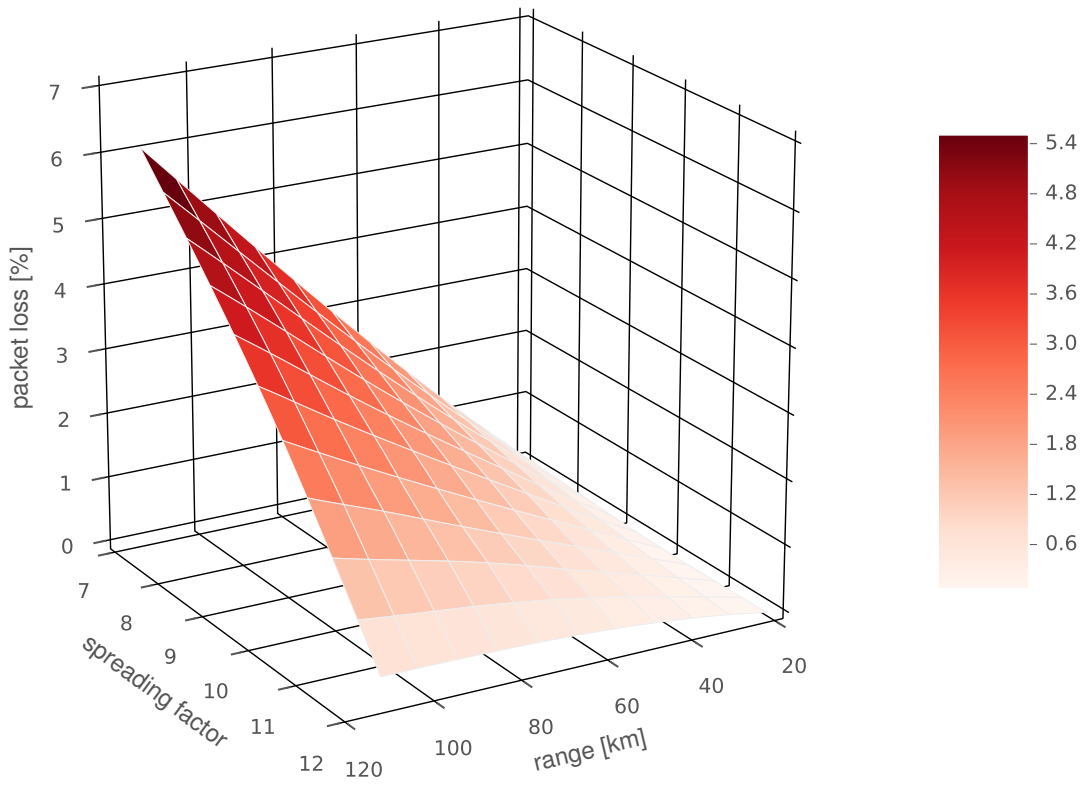

Figure 5.41: OdT cumulative packet loss at 434 MHz as a function of spreading factor and range.

Chapter 6

Conclusion

The objective of this research work was to develop the novel LoRa transceiver with improved characteristics and to gain a deeper insight into LoRa technology capabilities using the newly developed transceiver.

Since the LoRa is a new wireless technology, there are still no advanced general-purpose transceivers which might be used in scientific experiments; the current state of the art is based almost exclusively on the experiments carried out with the commercial LoRa development kits. The gained insight into technology capabilities may be limited since these transceivers struggle with different design trade-offs and cannot be classified as a scientific-graded experimental equipment.

Despite the fact that LoRa was developed to be used in long-range applications, the scientific community still does not have insights into long and ultra-long LoRa links behavior. Moreover, the conclusions drawn from the existing experiments are based on the grossly aggregate performance metrics, typically limited to long-term average values of RSS and packet loss, while temporal analysis of the link behavior was not performed. In addition, no work reports calibration of RSS indicator, which limits the accuracy and scope of the conclusions.

To bridge the identified gaps in the current state of the art, we developed a novel LoRa transceiver with improved characteristics in terms of sensitivity and immunity to external interferences. Furthermore, we optimized the transceiver in terms of power consumption and physical dimensions. The characteristics of the transceiver were verified in both laboratory and real operating conditions in the field. The results of the laboratory experiments revealed that the transceiver's sensitivity is

5 dB higher than the one specified for the LoRa modem IC used to implement the transceiver. Furthermore, the sensitivity comparison tests showed that the sensitivity of the novel LoRa transceiver is 15–25 dB higher than the sensitivity of two widely adopted commercial transceivers, namely Libelium and Uputronics. In addition, the laboratory tests revealed outstanding results in terms of power autonomy, yielding up to 10.9 years using 5 Ah lithium-polymer battery, when three 9-byte payload messages are sent per day, using SF = 10 and BW = 125 kHz.

On the other hand, the field tests showed that novel transceiver exhibits lower susceptibility to the external interferences in comparison to Libelium and Uputronics. Namely, during the strong interference bursts, where the novel LoRa transceiver was receiving packets simultaneously with two commercial transceivers, it recorded no packet loss, while Uputronics and Libelium experienced moderate and high packet loss, respectively. Furthermore, when interference bursts were strong enough to disable packet reception on commercial transceivers, the novel LoRa transceiver experienced moderate packet loss.

Field experiments also investigated long and ultra-long LoRa links in two typical propagation scenarios: LOS and obstructed LOS. The testbeds included propagation paths over both land and seawater, exploring link lengths of 22, 28, 112, and 316 km. The investigation was conducted for a variety of LoRa parameters, deploying three different spreading factors, SF $\in \{7, 10, 12\}$, within the bandwidth of BW = 125 kHz, and using the fixed coding rate of CR = 4/6. The parameters were selected to exploit different trade-offs offered by the LoRa technology in terms of data rate, power consumption, and sensitivity. Additionally, several different transceivers were deployed in each experiment to operate simultaneously in two ISM bands: 868 MHz, and 434 MHz.

To enable accurate measurements and valid conclusions, the calibration of RSS indicator of each transceiver was performed, and their linearity was investigated. We found that the RSS indicators are linear in a wide range of input signal levels, up to –50 dBm, and that they are self-coherent, but there is a constant difference between actual signal power and the one reported by the indicator. In the case of the novel LoRa transceiver, that difference yields 8.8 dB and 6.7 dB in 868 MHz and

434 MHz frequency band, respectively.

In addition, we investigated the saturation region of the SNR measurement chain and found that for the input signal levels higher than –100 dBm the measurement chain goes to the saturation. This implies that the analysis of SNR values recorded for the higher signal levels is not accurate and should not be adopted as a reliable parameter to assess the link quality.

The experimental results showed that LoRa transmission over seawater is fully feasible over distances up to 22 km if the LOS condition is provided. This conclusion is valid for both frequency bands of interest, namely 868 MHz, and 434 MHz. In addition, it can be assumed that such links are feasible for virtually any combination of LoRa parameters since the experimental parameters are selected to cover each LoRa mode, as mentioned earlier. The link margin indicates that higher distances may be achieved since it is in the range of 15–25 dB, depending on the frequency and LoRa parameters deployed. The significance of the results is amplified by the fact that low-cost omnidirectional COTS antennas were used at both sides.

Temporal analysis of the link behavior, in this case, showed that RSS did not fluctuate significantly. The fluctuations were caused by multipath propagation effects, which were not pronounced since the peak-to-peak value in the worst case was 5 dB. This, however, did not cause problems at the reception side. Since the RSS was remarkably high in almost all experiments in this group, the analysis of SNR was limited because the measurement chain was at the onset of the saturation practically all the time. Packet reception rate was constantly high, nearly without any packet loss except in the case of Libelium transceiver, which experienced significant packet loss for SF = 7, and, unexpectedly, for SF = 12. To find the cause of this packet loss, further investigation is needed since the remaining transceivers in the experiments did not experience such packet loss.

The experiments carried out on 28 km long obstructed LOS propagation path over seawater revealed that such links are not possible in either band of interest using omnidirectional antennas with standard-compliant output power. However, using bulky and higher gain antennas, the packet reception was possible on 434 MHz due to diffraction effects on the knife-edge obstacle. Nevertheless, it has to be noted

that the link quality, in this case, cannot be guaranteed.

Next, the experiments performed over 112 km long LOS path over land revealed that such links do not pose a challenge for LoRa technology in either of the frequency bands of interest. However, Libelium transceiver again experienced very high packet loss for SF = 7 which requires further investigation since the other receivers did not record any significant packet loss. This experimental scenario was particularly challenging in terms of interference since the receivers were placed at a very high altitude (1406 m above sea level) which provided favorable conditions for the different radio-interference to be coupled due to LOS propagation conditions in almost every direction. However, most of the time transceivers were able to maintain an almost flawless packet reception rate, except when very strong interference bursts were occurring. During these intervals, the increased immunity of the novel transceiver was clearly demonstrated since it succeeded to maintain significantly higher packet reception rate than commercial transceivers. The RSS was fluctuating significantly during experiments in this group, implying the strong multipath propagation effects. Despite the fact that the novel transceiver was occasionally recording the lowest RSS, it maintained the highest packet reception rate, which confirms its lowest noise floor and highest sensitivity. Finally, it should be pointed out that low-cost COTS omnidirectional antennas were deployed at both sides and in both frequency bands of interest, which makes the results even more interesting.

The feasibility of ultra-long LoRa links in LOS mode over land was investigated over 316 km long link in both frequency bands of interest. It was demonstrated that such links are possible on both frequencies of interest deploying omnidirectional antennas. However, this is valid only for novel LoRa transceiver since commercial transceivers were not able to receive packets. The packet reception rate during the experiments was degraded only during the strong interference bursts; the rest of the time, PRR remained at almost maximum value. It has to be noted that even on these link lengths, the novel LoRa transceiver provides approximately 5 dB of link margin.

A cumulative analysis of the parameters such as RSS, SNR, PRR, and packet loss, delivers several interesting observations. Namely, the experiments revealed that

the packet reception rate may not necessarily be the lowest for the lowest spreading factor within a fixed bandwidth. Counterintuitive, it can be the highest, while the use of higher spreading factors may result in lower packet reception rates. This could be explained by very long packet airtime, above 1 second, for the highest spreading factor which significantly increases the probability for intermittent interference to impair packet reception. In addition, it was observed that RSS and SNR fluctuations were increasing with increasing the spreading factor, which might also be the consequence of increased packet airtime. This implies, again counterintuitive, that the highest sensitivity LoRa operation mode may not yield the highest packet reception rate - this, however, depends on the level of the radio-interference present in the channel during packet reception.

To provide more general conclusions, this research study needs to be extended by performing long-term field experiments in which the link parameters would be recorded for months in continuity. In addition, the experimental setup should be upgraded to monitor weather conditions at both ends, and a real-time spectrum analyzer should be deployed on the receive side to record the spectrum while nodes are receiving the packets. Such an approach would provide the framework to correlate LoRa technology capabilities with environmental factors and with the level of interference in the communication channel in real operating conditions in the field.

However, the results presented in this work have several important implications. Firstly, the scientific experiments involving LoRa technology can be now performed using an optimized general-purpose LoRa transceiver with calibrated RSS indicator and determined operating range of SNR measurement chain. Consequently, the insights gained in such experiments would be accurate and would not depend on the peculiarities of the experimental setup. Secondly, the experimental results show that the LoRa technology is suitable to be used in very long range applications which are particularly important in the implementation of disaster preventions systems, such as e.g. early warning systems for volcano eruptions since the height of the volcano provides very long LOS trajectories in all directions. Finally, the low power consumption and cost of the developed transceiver allow for simpler deployment and maintenance which is of paramount importance for remote location deployments.

Bibliography

[1] Goursaud Claire and Gorce Jean-Marie. Dedicated networks for IoT : PHY / MAC state of the art and challenges. *EAI endorsed transactions on Internet of Things*, 1(1), 2015.

[2] Lavric Alexandru and Popa Valentin. Internet of Things and LoRa Low-Power Wide-Area Networks: A Survey. In *2017 International Symposium on Signals, Circuits and Systems (ISSCS)*, pages 1–5, 2017.

[3] Bor Martin, Vidler John, and Roedig Utz. LoRa for the Internet of Things. In *Proceedings of the 2016 International Conference on Embedded Wireless Systems and Networks*, pages 361–366, 2016.

[4] Vangelista Lorenzo. Frequency Shift Chirp Modulation: the LoRa™ Modulation. *IEEE Signal Processing Letters*, 24(12):1818–1821, 2017.

[5] Reynders Brecht and Pollin Sofie. Chirp Spread Spectrum as a Modulation Technique for Long Range Communication. In *2016 Symposium on Communications and Vehicular Technologies (SCVT)*, pages 1–5, 2016.

[6] Raza Usman, Kulkarni Parag, and Sooriyabandara Mahesh. Low Power Wide Area Networks: An Overview. *IEEE Communications Surveys & Tutorials*, 19(2):855–873, 2017.

[7] Georgiou Orestis and Raza Usman. Low Power Wide Area Network Analysis: Can LoRa Scale? *IEEE Wireless Communications Letters*, 6(2):162–165, 2017.

[8] Li Lingling, Ren Jiuchun, and Zhu Qian. On the Application of LoRa LPWAN Technology in Sailing Monitoring System. In *2017 13th Annual Conference*

on Wireless On-demand Network Systems and Services (WONS), pages 77–80, 2017.

[9] Spread SpectrumScene. The Advantages of Constant Envelope Modulation. http://sss-mag.com/cem.html. Accessed: 29 August 2018.

[10] Bastille Networks. Decoding LoRa. https://www.rsaconference.com/writable/presentations/file_upload/hta-f01-decoding-lora-a-wireless-network-for-the-internet-of-things_copy1.pdf. Accessed: 29 August 2018.

[11] Petäjäjärvi Juha, Mikhaylov Konstantin, Pettissalo Marko, Janhunen Janne, and Iinatti Jari. Performance of a Low-Power Wide-Area Network Based on LoRa Technology: Doppler Robustness, Scalability, and Coverage. *International Journal of Distributed Sensor Networks*, 13(3):1–16, 2017.

[12] Hazem Sallouha, Bertold Van den Bergh, Qing Wang, and Sofie Pollin. ulora: Ultra low-power, low-cost and open platform for the lora networks. In *Proceedings of the 4th ACM Workshop on Hot Topics in Wireless*, pages 43–47, 2017.

[13] Thomas Ameloot, Patrick Van Torre, and Hendrik Rogier. A compact low-power lora iot sensor node with extended dynamic range for channel measurements. *Sensors*, 18(7), 2018.

[14] Matteo Cerchecci, Francesco Luti, Alessandro Mecocci, Stefano Parrino, Giacomo Peruzzi, and Alessandro Pozzebon. A low power iot sensor node architecture for waste management within smart cities context. *Sensors*, 18(4), 2018.

[15] Marco Cattani, Carlo Alberto Boano, David Steffelbauer, Stefan Kaltenbacher, Markus Günther, Kay Römer, Daniela Fuchs-Hanusch, and Martin Horn. Adige: An efficient smart water network based on long-range wireless technology. In *Proceedings of the 3rd International Workshop on Cyber-Physical Systems for Smart Water Networks*, pages 3–6, 2017.

[16] V. Raju, A. S. N. Varma, and Y. S. Raju. An environmental pollution monitoring system using lora. In *2017 International Conference on Energy, Communication, Data Analytics and Soft Computing (ICECDS)*, pages 3521–3526, 2017.

[17] A. Javed, H. Larijani, A. Wixted, and R. Emmanuel. Random neural networks based cognitive controller for hvac in non-domestic building using lora. In *2017 IEEE 16th International Conference on Cognitive Informatics Cognitive Computing (ICCI*CC)*, pages 220–226, 2017.

[18] Gregora Lukas, Vojtech Lukas, and Neruda Marek. Indoor Signal Propagation of LoRa Technology. In *2016 17th International Conference on Mechatronics - Mechatronika (ME)*, pages 1–4, 2016.

[19] Neumann Pierre, Montavont Julien, and Noël Thomas. Indoor Deployment of Low-Power Wide Area Networks (LPWAN): a LoRaWAN Case Study. In *2016 IEEE 12th International Conference on Wireless and Mobile Computing, Networking and Communications (WiMob)*, pages 1–8, 2016.

[20] Ayele Eyuel, Hakkenberg Chiel, Pieter Meijers Jan, Zhang Kyle, Meratnia Nirvana, and Havinga Paul. Performance Analysis of LoRa Radio for an Indoor IoT Applications. In *2017 International Conference on Internet of Things for the Global Community (IoTGC)*, pages 1–8, 2017.

[21] Trinh L. H., Bui V. X., Nguyen T. Q. K., Le M. H., and Ferrero F. Signal Propagation of LoRa Technology Using for Smart Building Applications. In *2017 IEEE Conference on Antenna Measurements & Applications (CAMA)*, pages 381–384, 2017.

[22] Haxhibeqiri Jetmir, Karaagac Abdulkadir, Van den Abeele Floris, Joseph Wout, Moerman Ingrid, and Hoebeke Jeroen. LoRa Indoor Coverage and Performance in an Industrial Environment: Case Study. In *2017 22nd IEEE International Conference on Emerging Technologies and Factory Automation*, pages 1–8, 2017.

[23] Jörke Pascal, Böcker Stefan, Liedmann Florian, and Wietfeld Christian. Urban Channel Models for Smart City IoT Networks Based on Empirical Measurements of LoRa-links at 433 and 868 MHz. In *2017 IEEE 28th Annual International Symposium on Personal, Indoor, and Mobile Radio Communications (PIMRC)*, pages 1–6, 2017.

[24] Wixted Andrew, Kinnaird Peter, Larijani Hadi, Tait Alan, Ahmadinia Ali, and Strachan Nail. Evaluation of LoRa and LoRaWAN for Wireless Sensor Networks. In *2016 IEEE SENSORS*, pages 1–3, 2016.

[25] Sankar Ramachandran Gowri, Yang Fan, Lawrence Piers, Michiels Sam, Joosen Wouter, and Hughes Danny. μPnP-WAN: Experiences with LoRa and its Deployment in DR Congo. In *2017 9th International Conference on Communication Systems and Networks (COMSNETS)*, pages 63–70, 2017.

[26] Wang Shie-Yuan, Chen Yo-Ru, Chen Tzu-Yang, Chang Chia-Hung, Cheng Yu-Hsiang, Hsu Chun-Chia, and Lin Yi-Bing. Performance of LoRa-based IoT Applications on Campus. In *2017 IEEE 86th Vehicular Technology Conference (VTC-Fall)*, pages 1–6, 2017.

[27] Magrin Davide, Centenaro Marco, and Vangelista Lorenzo. Performance Evaluation of LoRa Networks in a Smart City Scenario. In *2017 IEEE International Conference on Communications (ICC)*, pages 1–7, 2017.

[28] Marco Cattani, Alberto Boano Carlo, and Kay Römer. An Experimental Evaluation of the Reliability of LoRa Long-Range Low-Power Wireless Communication. *Journal of Sensor and Actuator Networks*, 6(2):3–6, 2017.

[29] Iova Oana, Murphy Amy, Picco Gian, Pietro, Ghiro Lorenzo, Molteni Davide, Ossi Federico, and Cagnacci Francesca. LoRa from the City to the Mountains: Exploration of Hardware and Environmental Factors. In *Proceedings of the 2017 International Conference on Embedded Wireless Systems and Networks*, pages 317–322, 2017.

[30] Petäjäjärvi Juha, Mikhaylov Konstantin, Roivainen Antti, Hänninen Tuomo, and Pettissalo Marko. On the Coverage of LPWANs: Range Evaluation and Channel Attenuation Model for LoRa Technology. In *2015 14th International Conference on ITS Telecommunications (ITST)*, pages 55–59, 2015.

[31] Rahman Arrief and Suryanegara Muhammad. The Development of IoT LoRa: A Performance Evaluation on LoS and Non-LoS Environment at 915 MHz ISM Frequency. In *2017 International Conference on Signals and Systems (ICSigSys)*, pages 163–167, 2017.

[32] Ko Sungwook, Cho Yulim, Kim Sojeong, Jin Daehan, Song Hyunji, Chun Jiwon, Yim Daeun, and Smith Anthony. LoRa Network Performance Comparison Between Open Area and Tree Farm Based on PHY factors. In *2018 IEEE Sensors Applications Symposium (SAS)*, pages 1–6, 2018.

[33] Gaelens Johnny, Torre Patrick, Van, Verhaevert Jo, and Rogier Hendrik. LoRa Mobile-To-Base-Station Channel Characterization in the Antarctic. *Sensors*, 17(8), 2017.

[34] Noreen Umber, Bounceur Ahcene, and Clavie Laurent. A Study of LoRa Low Power and Wide Area Network Technology. In *2017 International Conference on Advanced Technologies for Signal and Image Processing (ATSIP)*, pages 1–6, 2017.

[35] Aloÿs Augustin, Jiazi Yi, Thomas Clausen, and William Mark Townsley. A Study of LoRa: Long Range & Low Power Networks for the Internet of Things. *Sensors*, 16(9), 2016.

[36] Centenaro Marco, Vangelista Lorenzo, Zanella Andrea, and Zorz Michele. Long-Range Communications in Unlicensed Bands: the Rising Stars in the IoT and Smart City Scenarios. *IEEE Wireless Communications*, 23(5):60–67, 2016.

[37] Bor Martin and Roedig Utz. LoRa Transmission Parameter Selection. In *2017 13th International Conference on Distributed Computing in Sensor Systems (DCOSS)*, pages 27–34, 2017.

[38] Lauridsen Mads, Vejlgaard Benny, István ZĊovács, Nguyen Huan, and Mogensen Preben. Interference Measurements in the European 868 MHz ISM Band with Focus on LoRa and SigFox. In *2017 IEEE Wireless Communications and Networking Conference (WCNC)*, pages 1–6, 2016.

[39] Angrisani L., Arpaia P., Bonavolontà F., Conti M., and Liccardo A. LoRa Protocol Performance Assessment in Critical Noise Conditions. In *2017 IEEE 3rd International Forum on Research and Technologies for Society and Industry (RTSI)*, pages 1–5, 2017.

[40] Haxhibeqiri Jetmir, Abeele Floris, Van den, Moerman Ingrid, and Hoebeke Jeroen. LoRa Scalability: A Simulation Model Based on Interference Measurements. *Sensors*, 17(6), 2017.

[41] Voigt Thiemo, Bor Martin, Roedig Utz, and Alonso Juan. Mitigating Inter-network Interference in LoRa Networks. In *Proceedings of the 2017 International Conference on Embedded Wireless Systems and Networks*, pages 323–328, 2017.

[42] Zhu Guibing, Liao Chun-Hao, Suzuki Makoto, Narusue Yoshiaki, and Morikawa Hiroyuki. Evaluation of LoRa Receiver Performance under Co-technology Interference. In *2018 15th IEEE Annual Consumer Communications & Networking Conference (CCNC)*, pages 1–7, 2018.

[43] Orfanidis Charalampos, Marie Feeney Laura, and Jacobsson Martin. Measuring PHY Layer Interactions Between LoRa and IEEE 802.15.4g Networks. In *2017 IFIP Networking Conference and Workshops*, pages 1–2, 2017.

[44] Persia Samuela, Carciofi Claudia, and Faccioli Manuel. NB-IoT and LoRA Connectivity Analysis for M2M/IoT Smart Grids Applications. In *2017 AEIT International Annual Conference*, pages 1–6, 2017.

[45] Aras Emekcan, Ramachandran Gowri, Sankar, Lawrence Piers, and Hughes Danny. Exploring The Security Vulnerabilities of LoRa. In *2017 3RD IEEE International Conference on Cybernetics (CYBCONF)*, pages 361–366, 2017.

[46] Cheng Yao, Saputra Hendra, Meng Goh Leng, and Wu Yongdong. Secure Smart Metering Based on LoRa Technology. In *2018 IEEE 4th International Conference on Identity, Security, and Behavior Analysis (ISBA)*, pages 1–8, 2018.

[47] Liu Sujuan, Xia Chuyu, and Zhao Zhenzhen. A Low-power Real-time Air Quality Monitoring System Using LPWAN based on LoRa. In *2016 13th IEEE International Conference on Solid-State and Integrated Circuit Technology (ICSICT)*, pages 379–381, 2016.

[48] Marco Cattani, Carlo Alberto Boano, David Steffelbauer, Stefan Kaltenbacher, Markus Günther, Kay Römer, Daniela Fuchs-Hanusch, and Martin Horn. An Efficient Smart Water Network Based on Long-Range Wireless Technology. In *CySWATER '17 Proceedings of the 3rd International Workshop on Cyber-Physical Systems for Smart Water Networks*, pages 3–6, 2017.

[49] Su Chia-Min, Shi Cheng-Yu, Wu Yong-Lin, and Le Huang-Chen. A LoRa Wireless Smart Badge for Enhancing Museum Visitors' Experience. In *2017 16th ACM/IEEE International Conference on Information Processing in Sensor Networks (IPSN)*, pages 261–262, 2017.

[50] Hadwen Tim, Smallbon Vanessa, Zhang Qing, and D'Souza Matthew. Energy Efficient LoRa GPS Tracker for Dementia Patients. In *2017 39th Annual International Conference of the IEEE Engineering in Medicine and Biology Society (EMBC)*, pages 771–774, 2017.

[51] Petäjäjärvi Juha, Mikhaylov Konstantin, Hämäläinen Matti, and Iinatti Jari. Evaluation of LoRa LPWAN Technology for Remote Health and Wellbeing Monitoring. In *2016 10th International Symposium on Medical Information and Communication Technology (ISMICT)*, pages 1–5, 2016.

[52] Facchini Francesca, Vitetta Giorgio, Losi Alessandro, and Ruscelli Fabio. On the Performance of 169 MHz WM-Bus and 868 MHz LoRa Technologies in Smart Metering Applications. In *2017 IEEE 3rd International Forum on Research and Technologies for Society and Industry (RTSI)*, pages 1–6, 2017.

[53] Kumar Sangeeth, Rangan Venkat, and Vinodini Ramesh Maneesha. Poster: Pilot Deployment of Early Warning System for Landslides in Eastern Himalayas. In *Proceedings of the Annual International Conference on Mobile Computing and Networking, MOBICOM, Association for Computing Machinery*, pages 97–98, 2016.

[54] Li Yuezhong, Zeng Lingyuan, Yan Xiaoqiang, and Wu Hualing. Research on Water Meter Reading System Based on LoRa Communication. In *2017 IEEE International Conference on Smart Grid and Smart Cities (ICSGSC)*, pages 248–251, 2017.

[55] Trasviña-Moreno Carlos, Blasco Rubén, Marco Álvaro, Casas Roberto, and Trasviña-Castro Armando. Unmanned Aerial Vehicle Based Wireless Sensor Network for Marine-Coastal Environment Monitoring. *Sensors*, 17(3), 2017.

[56] Hayati Nur and Suryanegara Muhammad. The IoT LoRa System Design for Tracking and Monitoring Patient with Mental Disorder. In *2017 IEEE International Conference on Communication, Networks and Satellite (Comnetsat)*, pages 135–139, 2017.

[57] Tzortzakis Konstantinos, Papafotis Konstantinos, and Sotiriadi Paul. Wireless Self Powered Environmental Monitoring System for Smart Cities based on LoRa. In *2017 Panhellenic Conference on Electronics and Telecommunications (PACET)*, pages 1–4, 2017.

[58] Saleh Ali Muthanna Mohammed, Ahmed Muthanna Mohammed Manea, Khakimov Abdukodir, and Muthanna Ammar. Development of Intelligent Street Lighting Services Model Based on LoRa Technology. In *2018 IEEE Conference of Russian Young Researchers in Electrical and Electronic Engineering (EIConRus)*, pages 90–93, 2018.

[59] Chou Yu-Shang, Mo Yu-Ching, Su Jian-Ping, Chang Wan-Jung, Chen Liang-Bi, Tang Jing-Jou, and Yu Chao-Tang. i-Car System: A LoRa-based Low Power Wide Area Networks Vehicle Diagnostic System for Driving Safety. In

2017 International Conference on Applied System Innovation (ICASI), pages 789–791, 2017.

[60] Ouya Ange, Martinez De Aragon Blanca, Bouette Cecile, Habault Guillaume, Montavont Nicolas, and Papadopoulos Georgios. An Efficient Electric Vehicle Charging Architecture based on LoRa Communication. In *2017 IEEE International Conference on Smart Grid Communications (SmartGridComm)*, pages 381–386, 2017.

[61] Verbeke Thomas, Olti Emoke, and Munteanu Adrian. Development and Demonstration of a LoRa TDOA-based Localization System. In *Proceedings of the 10th International Conference on Distributed Smart Camera*, pages 206–207, 2016.

[62] Kim Dong Hyun, Park Jung Bin, Shin Jae Ho, and Kim Jong Deok. Design and Implementation of Object Tracking System Based on LoRa. In *2017 International Conference on Information Networking (ICOIN)*, pages 463–467, 2017.

[63] Fargas Bernat, Carbonés and Petersen Martin, Nordal. GPS-free Geolocation using LoRa in Low-Power WANs . In *2017 Global Internet of Things Summit (GIoTS)*, pages 1–6, 2017.

[64] Kim Dong Hyun, Lim Jun Young, and Kim Jong Deok. Low-Power, Long-Range, High-Data Transmission Using Wi-Fi and LoRa. In *2016 6th International Conference on IT Convergence and Security (ICITCS)*, pages 1–3, 2016.

[65] Benaissa Said, Plets David, Tanghe Emmeric, Trogh Jens, Martens Luc, Vandaele Leen, Verloock Leen, André Frank, Tuyttens Maurice, Sonck Bart, and Joseph Wout. Internet of Animals: Characterization of LoRa sub-GHz Off-body Wireless Channel in Dairy Barns. *Electronic letters*, 53(18):1281–1283, 2017.

[66] Yim Daeun, Chung Jiwon, Cho Yulim, Song Hyunji, Jin Daehan, Kim Sojeong, Ko Sungwook, Smith Anthony, and Riegsecker Austin. An Experimental LoRa

Performance Evaluation in Tree Farm. In *2018 IEEE Sensors Applications Symposium (SAS)*, pages 1–6, 2018.

[67] Usmonov Maksudjon and Gregoretti Francesco. Design and Implementation of a LoRa Based Wireless Control for Drip Irrigation Systems. In *2017 2nd International Conference on Robotics and Automation Engineering (ICRAE)*, pages 248–253, 2017.

[68] Zhao Wenju, Lin Shengwei, Han Jiwen, Xu Rongtao, and Lu Hou. Design and Implementation of Smart Irrigation System Based on LoRa. In *2017 IEEE Globecom Workshops (GC Wkshps)*, pages 1–6, 2017.

[69] Hirata Tadaaki, Terada Keitaro, Toyota Masaharu, Takada Yuya, Keiko Matsumoto, and Sode Tanaka Mikiko. Proposal of a Power Saving Network for Rice Fields Using LoRa. In *2017 IEEE 6th Global Conference on Consumer Electronics (GCCE)*, pages 1–4, 2017.

[70] Liu Xingqiao and Hu Caihong. Research on Remote Measurement and Control System of Piggery Environment Based on LoRa. In *2017 Chinese Automation Congress (CAC)*, pages 7016–7019, 2017.

[71] Petrić Tara, Goessens Mathieu, Nuaymi Loutfi, Pelov Alexander, and Laurent Toutain. Measurements, Performance and Analysis of LoRa FABIAN, a real-world implementation of LPWAN. In *2016 IEEE 27th Annual International Symposium on Personal, Indoor, and Mobile Radio Communications (PIMRC)*, pages 1–7, 2016.

[72] Rizzi Mattia, Ferrari Paolo, Flammini Alessandra, Sisinni Emiliano, and Gidlund Mikael. Using LoRa for Industrial Wireless Networks. In *2017 IEEE 13th International Workshop on Factory Communication Systems (WFCS)*, pages 1–4, 2017.

[73] Yang Fan, Sankar Ramachandran Gowri, Lawrence Piers, Michiels Sam, Joosen Wouter, and Hughes Danny. μPnP-WAN: Wide Area Plug and Play Sens-

ing and Actuation with LoRa. In *2016 International SoC Design Conference (ISOCC)*, pages 225–226, 2016.

[74] Ke Kai-Hsiang, Liang Qi-Wen, Chen Guan-Heng, Zeng Guan-Jie, Cheng Kai-Lin, Su Chia-Min, Lin Jun-Han, and Le Huang-Chen. A LoRa Wireless Mesh Networking Module for Campus - Scale Monitoring. In *Proceeding IPSN '17 Proceedings of the 16th ACM/IEEE International Conference on Information Processing in Sensor Networks*, pages 259–260, 2017.

[75] So Jaeyoung, Kim Daehwan, Kim Hongseok, Lee Hyunseok, and Park Suwon. LoRaCloud: LoRa Platform on OpenStack. In *2016 IEEE NetSoft Conference and Workshops (NetSoft)*, pages 431–434, 2016.

[76] Spinsante Susanna, Ciattaglia Gianluca, Del Campo Antonio, Perla Davide, Pigini Danny, Cancellieri Giovanni, and Gambi Ennio. A LoRa Enabled Building Automation Architecture Based on MQTT. In *2017 AEIT International Annual Conference*, pages 1–5, 2017.

[77] Choi Chang-Sic, Jeong Jin-Doo, Lee Il-Woo, and Park Wan-Ki. LoRa based Renewable Energy Monitoring System with Open IoT Platform. In *2018 International Conference on Electronics, Information, and Communication (ICEIC)*, pages 1–2, 2018.

[78] Xue-fen Wan, Xing-jing Du, Jian Cui, Yi Yang, Jing-wen Zhang, and Sohail Sardar Muhammad. Smartphone Based LoRa In-soil Propagation Measurement for Wireless Underground Sensor Networks. In *2017 IEEE Conference on Antenna Measurements & Applications (CAMA)*, pages 114–117, 2017.

[79] Wan Xue-Fen, Yang Yi, Du Xingjing, and Sohail Sardar Muhammad. Design of Propagation Testnode for LoRa Based Wireless Underground Sensor Networks. In *2017 Progress in Electromagnetics Research Symposium - Fall (PIERS - FALL)*, pages 579–583, 2017.

[80] Jovalekic Nikola, Drndarevic Vujo, Darby Iain, Zennaro Marco, Pietrosemoli Ermanno, and Ricciato Fabio. Lora transceiver with improved characteristics. *IEEE Wireless Communications Letters*, 2018.

[81] EFM32GG Data Sheet. https://www.silabs.com/documents/public/data-sheets/efm32gg-datasheet.pdf. Accessed: 29 August 2018.

[82] SX1276/77/78/79 - 137 MHz to 1020 MHz Low Power Long Range Transceiver. https://www.semtech.com/uploads/documents/DS_SX1276-7-8-9_W_APP_V5.pdf. Accessed: 29 August 2018.

[83] Semtech SX127x Reference Design Overview. https://www.semtech.com/uploads/documents/AN1200.19_SX127x_RefDesign_STD.pdf. Accessed: 29 August 2018.

[84] Spartaco Caniggia and Francescaromana Maradei. *Signal Integrity and Radiated Emission of High-Speed Digital Systems*. John Wiley & Sons Ltd, 2008.

[85] Eric Bogatin. *Signal and Power Integrity Simplified*. Prentice Hall, 2013.

[86] T.V Narayanan. *Fast Methods for Full-Wave Electromagnetic Simulations of Integrated Circuit Package Modules*. PhD thesis, Georgia Institute of Technology, 2011.

[87] ETSI. EN 300 220-1 V3.1.0 (2016-05). http://www.etsi.org/deliver/etsi_en/300200_300299/30022001/03.01.00_20/en_30022001v030100a.pdf. Accessed: 29 August 2018.

[88] Marco Zennaro, Marco Rainone, and Ermanno Pietrosemoli. Radio link planning made easy with a telegram bot. In *Smart Objects and Technologies for Social Good*, pages 295–304, 2017.

[89] N. Youssef, Cheng-Xiang Wang, M. Patzold, I. Jaafar, and S. Tabbane. On the statistical properties of generalized rice multipath fading channels. In *2004 IEEE 59th Vehicular Technology Conference. VTC 2004-Spring (IEEE Cat. No.04CH37514)*, pages 162–165 Vol.1, 2004.

[90] Carlo Alberto Boano, Marco Cattani, and Kay Römer. Impact of temperature variations on the reliability of lora - an experimental evaluation. In *7th International Conference on Sensor Networks - Volume 1 (SENSORNETS)*, pages 39–50, 2018.

[91] Carlo Alberto Boano, James Brown, Zhitao He, Utz Roedig, and Thiemo Voigt. Low-power radio communication in industrial outdoor deployments: The impact of weather conditions and atex-compliance. In *Sensor Applications, Experimentation, and Logistics*, pages 159–176, 2010.

Author's Biography

Nikola Jovalekic was born on 11. 10. 1982. in Belgrade. He completed his elementary and high school education in Belgrade, and graduated at the Department of Electronics, School of Electrical Engineering, University of Belgrade in 2007. For his graduation project, he designed and implemented a system with DC motor which was remotely controlled utilizing GSM short message service (SMS). During his undergraduate studies, in the period 2003 - 2007, he worked as a demonstrator lab assistant in the Fundamentals of Electrical Engineering laboratory. In 2007 he started to work in the research and development institute for telecommunications and electronics IRITEL, as a hardware design engineer in the Optical Transmission Department. He participated in numerous projects, and is the author of a technical solution registered with the Ministry of Education, Science and Technological Development of Serbia. In 2011. he moved to Slovenia and worked as a hardware design engineer in two companies until 2017. He was awarded the "Ilija Stojanovic" award for the best scientific paper at the International Scientific Conference Telfor in 2012. In 2017., he was awarded the IAEA/ICTP Step Fellowship for his research work in Vienna, Austria. He speaks Serbian, English, Russian and Slovenian languages fluently.

Publications:

M21:

N. Jovalekic, V. Drndarevic, I. Darby, M. Zennaro, E. Pietrosemoli, and F. Ricciato. Lora Transceiver With Improved Characteristics. *IEEE Wireless Communications Letters*, 2018. DOI: 10.1109/LWC.2018.2855744; **IF=3.096**

M21:

N. Jovalekic, V. Drndarevic, E. Pietrosemoli, I. Darby, and M. Zennaro. Experimental Study of LoRa Transmission over Seawater. Sensors, 18(9), 2018. DOI: 10.3390/s18092853; **IF=2.475**

M33:

N. Jovalekic, E. Pietrosemoli, M. Rainone, and M. Zennaro. Smart and very distant objects. In Proceedings of the 3rd Workshop on Experiences with the Design and Implementation of Smart Objects, pages 29-34, 2017. DOI: 10.1145/3127502.3127514

Изјава о ауторству

Име и презиме аутора Никола Јовалекић

Број индекса 5063/2010

Изјављујем

да је докторска дисертација под насловом

Побољшање перформанси бежичних примопредајника заснованих на *LoRa* модулацији

- резултат сопственог истраживачког рада;
- да дисертација у целини ни у деловима није била предложена за стицање друге дипломе према студијским програмима других високошколских установа;
- да су резултати коректно наведени и
- да нисам кршио/ла ауторска права и користио/ла интелектуалну својину других лица.

Потпис аутора

У Београду, 20. 08. 2018.

Никола Јовалекић

Изјава о истоветности штампане и електронске верзије докторског рада

Име и презиме аутора Никола Јовалекић

Број индекса 5063/2010

Студијски програм Електроника

Наслов рада Побољшање перформанси бежичних примопредајника заснованих на *LoRa* модулацији

Ментор др Вујо Дрндаревић

Изјављујем да је штампана верзија мог докторског рада истоветна електронској верзији коју сам предао ради похрањења у **Дигиталном репозиторијуму Универзитета у Београду.**

Дозвољавам да се објаве моји лични подаци везани за добијање академског назива доктора наука, као што су име и презиме, година и место рођења и датум одбране рада.

Ови лични подаци могу се објавити на мрежним страницама дигиталне библиотеке, у електронском каталогу и у публикацијама Универзитета у Београду.

Потпис аутора

У Београду, 20. 08. 2018.

Никола Јовалекић

Изјава о коришћењу

Овлашћујем Универзитетску библиотеку „Светозар Марковић“ да у Дигитални репозиторијум Универзитета у Београду унесе моју докторску дисертацију под насловом:

Побољшање перформанси бежичних примопредајника заснованих на LoRa модулацији

која је моје ауторско дело.

Дисертацију са свим прилозима предао сам у електронском формату погодном за трајно архивирање.

Моју докторску дисертацију похрањену у Дигиталном репозиторијуму Универзитета у Београду и доступну у отвореном приступу могу да користе сви који поштују одредбе садржане у одабраном типу лиценце Креативне заједнице (Creative Commons) за коју сам се одлучио.

1. Ауторство (CC BY)

2. Ауторство – некомерцијално (CC BY-NC)

3. Ауторство – некомерцијално – без прерада (CC BY-NC-ND)

4. Ауторство – некомерцијално – делити под истим условима (CC BY-NC-SA)

5. Ауторство – без прерада (CC BY-ND)

6. Ауторство – делити под истим условима (CC BY-SA)

(Молимо да заокружите само једну од шест понуђених лиценци.
Кратак опис лиценци је саставни део ове изјаве).

Потпис аутора

У Београду, 20. 08. 2018.

Никола Јовалекић